THESIS

Laser Frequency Stabilization with a Cryogenic Optical Cavity

Takafumi Ushiba

Department of Physics, Faculty of Science,
University of Tokyo.

December 2015

Abstract

In the field of precise measurements such as gravitational-wave detectors and optical atomic clocks, the frequency instability of a laser determines the performance. Especially in the case of state-of-the-art optical atomic clocks, the frequency noise of a probe laser limits their stability. Therefore, improvements of the frequency stability of a laser are necessary to make the performance of optical atomic clocks better.

In this research, we have aimed to improve the laser frequency stability in order to make better optical lattice clocks. Since the cycle time of a measurement of the atomic transition frequency at an optical lattice clock is about 1 second, the laser frequency instability at around 1 second determines the clock instability through the Dick effect.

Currently, an optical cavity with a rigid spacer gives the best stability at around 1 second. However, the stability of several cavity-stabilized lasers has already reached the thermal-noise limit of the cavity components, which is one of the fundamental noises. Thus, reducing the cavity thermal noise is indispensable for obtaining better frequency stability. For this purpose, new developments are under way around the world through several approaches; for example, a longer cavity length, crystalline mirror coating with a high mechanical Q factor, and operation at cryogenic temperature.

A state-of-the-art cavity-stabilized laser has been reached an Allan deviation of 1×10^{-16} at 1 second, which is close to the thermal-noise limit of this cavity. For further reductions of the thermal noise to reach a stability of 1×10^{-17}, utilizing a cryogenic cavity below 20 K is inevitable. Thus, several groups are currently trying to make an optical cavity to work at a very low temperature, but there is no reported result that shows an instability less than 1×10^{-16}, because a cryogenic cavity at below 70 K needs a cryogenic refrigerator that can easily induce additional noises. A group in Germany reported an Allan deviation of 2×10^{-13} at around 1 second and 2×10^{-14} at around 1000

seconds using a silicon cavity operated at a very low temperature; they also discussed the thermal property necessary to reach 2×10^{-17} stability. However, the noises that limit the current instability have not been shown.

In this thesis, we construct a laser frequency-stabilizing system with a monocrystalline silicon cavity operated at a very low temperature. In order to realize a temperature-stable and quiet environment at less than 20 K, we used a cryogenic refrigerator with helium recondensation as well as a multiple stack structure with glass balls for thermal isolation. We used a passive and active vibration isolation system for reducing the effect of seismic motion and vibration from the refrigerator. In addition, several noise-reduction system such as Doppler noise cancellation, laser power stabilization, etc, were installed.

We evaluated the performance of our system quantitatively. The instability result has been evaluated to have an Allan deviation of $\sigma_y = 7.03^{+0.38}_{-0.34} \times 10^{-15}$. This instability is lowest around 1 second using an optical cavity operated at a very low temperature. Moreover, we evaluated any noise contributions for the frequency instability due to various effects, such as seismic motion, temperature fluctuation, etc, and found that the acceleration noise limits the stability of our laser frequency.

In this work, we showed that laser stabilization with a very low-temperature optical cavity can reach a 10^{-15} level at around 1 second. Moreover, we showed prospects to reach a stability below 10^{-16} by using a cryogenic optical cavity.

Thesis supervisor: Masaki Ando

Thesis title: Laser Frequency Stabilization with a Cryogenic Optical Cavity

要旨

重力波検出器や光格子時計などの精密測定分野では、レーザーの周波数安定度がそれらの性能を決める。特に世界最高水準の光格子時計ではプローブレーザーの周波数雑音が時計の安定度を制限しており、より高性能な時計を作るにはレーザーの周波数安定度を向上させる必要がある。

本研究ではより高性能な光格子時計開発のために、レーザー周波数の安定化を行っている。光格子時計では原子の遷移周波数測定にかかる時間が 1 秒程度であるため、1 秒付近のレーザー周波数の安定度がディック効果を介して時計の性能を制限する。

1 秒付近の周波数基準として現在最も安定なものは光共振器である。しかしながら、世界最高水準の光共振器に安定化されたレーザーの安定度は原理的な雑音の一つである光共振器の熱雑音レベルに到達している。したがって、レーザーの周波数安定度をより向上させるには光共振器の熱雑音低減が必要不可欠であり、長い光共振器や機械的 Q 値の高いコーティングを用いた共振器、低温化した共振器を利用した周波数安定化が試みられている。

世界最高の光共振器に安定化されたレーザーの安定度は 1 秒のアラン標準偏差で 1×10^{-16} を実現しており、その共振器の熱雑音限界近くまで到達している。そのため、1×10^{-17} の周波数安定度を目指した更なる熱雑音低減のためには、20 K 以下の極低温光共振器を用いることが必要不可欠である。現在いくつかの研究グループが安定な極低温光共振器の製作を試みているが、70 K 以下の温度領域に到達するためには新たな雑音源となりうる冷凍機を用いる必要があるため、未だ 10^{-16} 以下の安定度は報告されていない。ドイツのグループのみが極低温の光共振器に安定化したレーザーの周波数安定度を報告しており、そのアラン標準偏差は 1 秒付近で 2×10^{-13}、1000 秒付近で 2×10^{-14} である。この共振器の熱特性によって決まる安定度の限界は 2×10^{-17} とされているが、現在の安定度を制限する要因についてはわかっていない。

そこで、我々は極低温動作の光共振器による周波数安定化レーザーを構築した。本実験では高い温度安定性と静寂な環境を実現するため、ヘリウムガスの凝縮を利用したパルスチューブ冷凍機を用いている。また、高い温度安定性

の確保のためにガラス球を用いた多段のスタック構造を用いている。さらに、地面振動や冷凍機の振動が光共振器に伝わらないように受動防振と能動防振を組み合わせた防振装置を用いている。加えて、ドップラー雑音除去やレーザーの強度安定化などの雑音低減措置もとられている。

この周波数安定化システムを定量的に評価することによって$7.03^{+0.38}_{-0.34}\times10^{-15}$のアラン標準偏差を得た。この結果は極低温の光共振器を用いた周波数安定化レーザーとして最も安定なものである。また、地面振動や温度揺らぎなどの雑音の寄与を定量的に調べることにより、私たちの周波数安定度が共振器に加わる加速度の影響によって制限されていることを示した。

これにより、極低温の光共振器を用いても10^{-15}台の安定度のレーザーが構築できることを示した。また、極低温の光共振器を用いた周波数安定化によって10^{-17}台の安定度を達成するための具体的な方法を示した。

指導教員：安東正樹（准教授）
論文題目：極低温光共振器を用いたレーザー周波数安定化

Acknowledgements

This experiment has been supported by many people. Here, I would like to express my gratitude to them.

First, I would like to thank my supervisors. My former supervisor, Kimio Tsubono, gave me a chance to start this experiment. If I could not have become acquainted with him, I could not pursue to this work. My current supervisor, Masaki Ando, held meetings for my doctoral thesis and discuss the schedule of the experiment and writing. I could not have finished writing this thesis without him. My second supervisor, Hidetoshi Katori, in the ALPS course often gave me a useful advice for my experiment. He also gave me a chance to do this work in his laboratory at RIKEN.

I am glad to have worked with my co-researchers. Yoichi Aso is one of proposers of this experiment. He contrived the conceptual idea using thermal insulation stacks. Noriaki Ohmae is a very reliable person for me. Almost all the progress and failures of this work were reported to him at first and he always showed me the next way to go. He also help me directly to construct the experimental setup when I did that work that was difficult to do alone. Moreover, the narrow linewidth laser that is used in the beat frequency measurement was developed by him. Ayaka Shoda taught me the concept of a feedback system involving AVIS. The circuit made by her was also used in the experiment.

I am obliged to our group members. Yuta Michimura, who is a current assistant professor of our group, gave me some experimental advice. Kentaro Komori and Yuya Kuwahara, who are the 2nd-year master course students, were good for discussing the experimental and theoretical matters. Naoki Aritomi and Tomofumi Shimoda, who are 1st-year master course students, helped me to cope with incidental tasks at Hongo campus while in RIKEN.

I would also like to thank past members of our group. Wataru Kokuyama taught me how to progress the research and pursue life as a PhD student.

Nobuyuki Matsumoto often gave me fundamental questions concerning the experiment, and thus I could reconsider my experiment deeply each time.

I am grateful to the engineers of the Faculty of Science. My work could not have been completed without Shigemi Otsuka and Yoshikatsu Nanjo.

This research is mainly supported by Prof. Katori's ERATO project, Innovative Space-Time project, Japan Science and Technology Agency, and JSPS Grant-in-Aid for JSPS Fellows Number 15J11096. Also, this research is also performed in Prof. Katori's laboratory, Quantum Metrology Laboratory, RIKEN.

Finally, I greatly thankful my parents for their continuous support of my life.

Contents

Glossary

Symbols

i	imaginary unit $\mathrm{i} = \sqrt{-1}$
c	speed of light $c = 299792458$ m/s
h	Planck's constant $h = 6.626 \times 10^{-34}$ Js
$\hbar$	Dirac constant $\hbar = h/2\pi = 1.055 \times 10^{-34}$ Js
k_B	Boltzmann constant $k_\mathrm{B} = 1.381 \times 10^{-23}$ J/s
σ_B	Stefan-Boltzmann constant $\sigma_\mathrm{B} = 5.670 \times 10^{-8}$ J/s
e	elementary charge $e = 1.602 \times 10^{-19}$ C
λ	laser wavelength
ν	laser frequency [Hz] ($\nu = c/\lambda$)
Ω	laser angular frequency [rad/sec] ($\Omega = 2\pi\nu$)
f	Fourier frequency [Hz]
n	refractive index
L	length of a FPC
$\mathcal{F}$	finesse of a FPC
p_0	pressure of standard condition gas
V_0	volume of standard condition gas
T_0	temperature of standard condition gas
N_A	Avogadro's constant $N_\mathrm{A} = 6.022 \times 10^{23}$

Acronyms

ADC	analog-to-digital converter
AR	anti-reflective, anti-reflection
AOM	acousto-optic modulator
AVIS	active vibration isolation system
AVIT	active vibration isolation table
BS	beam splitter
CTE	coefficient of thermal expansion
DAMI	differential arm length Michelson interferometer
EOM	electro-optic modulators
ECDL	external cavity diode laser
FDT	fluctuation dissipation theorem
FEM	finite element method
FPC	Fabry-Perot cavity
FSR	free spectral range
FWHM	full width at half maximum
HR	high-reflection
HWP	half-wave plate
LD	laser diode
OFC	oxide-free copper
PBS	polarizing beam splitter
PD	photodetector, photodiode
PDH	Pound-Drever-Hall (method)
PSD	power spectral density
PVIS	passive vibration isolation system
PZT	lead zirconate titanate (piezoelectric transducer)
QWP	quarter-wave plate
RMS	root mean square
RAM	residual amplitude modulation (noise)
TIS	thermal isolation stack
VCXO	voltage-controlled crystal oscillator

Chapter 1
Introduction

Since the development of the laser in 1960 [1], lasers have been used in many fields of academic research, such as material science, quantum physics, and astronomy. As these researches became more complicated and precise, the importance of a frequency stabilized laser has been increasing. In resent years, very stable lasers are required in several fields, such as gravitational-wave detectors [2–4], gravity measurements [5], and optical clocks [6]. Especially in the field of frequency standard, the stability of several clocks, for example Sr and Hg optical lattice clocks, is limited by the frequency fluctuations of a probe laser, which detects the atomic transition frequency [7, 8].

The frequencies of several optical clocks are used for secondary representations of the second [9], and these are candidates for the next definition of second. Therefore, improving the stability of these clocks is very important for many fields of science. Moreover, optical clocks are also useful for fundamental physics. Stable clocks can be used for testing the local position invariance by measuring the constancy of the fine-structure constant [10]. Therefor, improvements of optical clocks are essential for state-of-the-art science.

To focus on optical lattice clocks, the instability of a probe laser at around 1 second determines their instability [7] through the Dick effect [11]. Thus, improving the laser frequency instability at around 1 second is important for making better optical lattice clocks [12]. Optical lattice clocks are achieved by stabilizing the probe laser frequency to the atomic-transition frequency [6]. Since their stability typically improves in proportion to $1/\sqrt{\tau}$ [13], where τ is the averaging time of the frequency measurement, the single measurement accuracy of atomic transition frequency determines the clock instability. Since the minimal feedback cycle time in optical lattice clocks is about 1 second

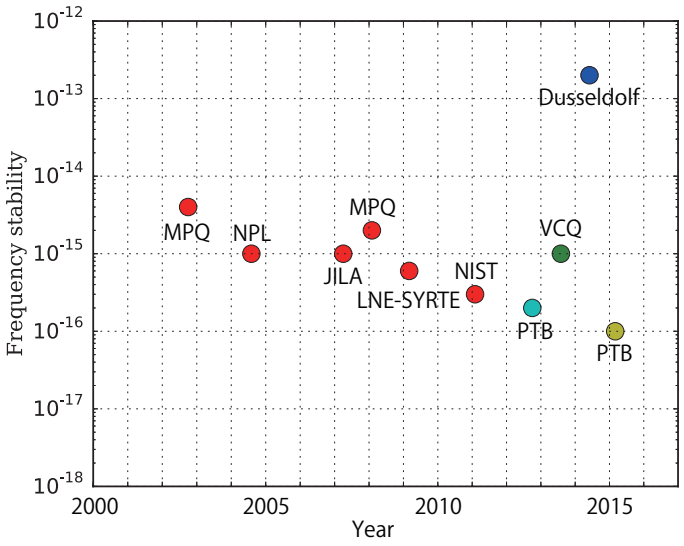

Figure 1.1: The history of the frequency stability of the major cavity-stabilized lasers. Red dots are the frequency-stabilized lasers with a cavity at room temperature [16–21]. The yellow dot is when using a long cavity of about 48 cm [24]. The green dot is when using crystalline coating mirrors that have a high mechanical Q factor [22]. The light-blue dot is when using a cryogenic optical cavity at around 124 K [12]. The blue dot is when using a cryogenic cavity below 24 K [23]. The stability is the Allan deviation or modified Allan deviation at around 1 second. Detailed characteristics are given in Table 1.1

[13–15], the stability of optical lattice clocks has been improved when the laser frequency stability at around 1 second becomes better.

Frequency stabilization at around 1 second is often performed using an optical cavity with a rigid spacer, because it provides the best current stability at around 1 second. Figure 1.1 shows the history of the major cavity-stabilized lasers [12, 16–24]; Table 1.1 gives their stability and several characteristics.

In 2004, it was suggested that the frequency instability of several narrow-linewidth lasers was limited by the Brownian thermal noise of the cavity components [25]. The thermal-noise level of lasers discussed in this paper was estimated for an Allan deviation of $\sigma_y \simeq 3 \times 10^{-16}$. Therefore, thermal-noise reduction is necessary to achieve frequency stability below 3×10^{-16}. One approach for reducing the thermal noise is to use a long cavity [24]. The

Institute	Instability	Length	Temperature	Coatings
MPQ [16]	4×10^{-15}	27 cm	about 300 K	dielectric multilayer
NPL [17]	1×10^{-15}	10 cm	about 300 K	dielectric multilayer
JILA [18]	1×10^{-15}	7 cm	about 300 K	dielectric multilayer
MPQ [19]	2×10^{-15}	7.8 cm	about 300 K	dielectric multilayer
LNE-SYRTE [20]	6×10^{-16}	10 cm	about 300 K	dielectric multilayer
NIST [21]	3×10^{-16}	29 cm	about 300 K	dielectric multilayer
PTB [12]	2×10^{-16}	21 cm	about 124 K	dielectric multilayer
VCQ [22]	1×10^{-15}	3.5 cm	about 300 K	crystalline multilayer
Dusseldolf [23]	2×10^{-13}	25 cm	below 24 K	dielectric multilayer
PTB [24]	1×10^{-16}	48 cm	about 300 K	dielectric multilayer

Table 1.1: The stability and several characteristics of each frequency stabilized laser shown in Fig. 1.1. The instability of PTB [12] is the modified Allan deviation at around 1 second. The instability of the other results is the Allan deviation at around 1 second. The instability is read from the graph of the Allan deviation or the modified Allan deviation of lasers in Ref. [12, 16–24].

estimated thermal-noise level of the cavity, which is about 48 cm long, is $\sigma_y \simeq 5.4 \times 10^{-17}$. The instability of the laser is $\sigma_y \simeq 9 \times 10^{-17}$ at around 100 seconds and $\sigma_y \simeq 1 \times 10^{-16}$ at around 1 second. This result is the highest frequency stability at around 1 second, which is close to the thermal-noise limit. Another approach is to construct a reference cavity with high mechanical Q-factor coating mirrors [22]. The estimated thermal noise level of the cavity is $\sigma \simeq 1 \times 10^{-15}$ and the instability of the laser is $\sigma_y \simeq 1 \times 10^{-15}$ at around 1 second. The thermal-noise level of this cavity is not so good because the cavity length is short, 3.5 cm long. However, its stability reaches a stability which cannot be achieved with conventional dielectric multilayer coatings. Thus, this result is very important in terms of making high mechanical Q-factor coatings. Another approach is to cool an optical cavity at low temperature [12, 23]. One way is to cool the optical cavity at around 124 K, which is the zero-cross temperature of the coefficient of thermal expansion (CTE) of monocrystalline silicon [12]. The thermal-noise level of the cavity is estimated at the modified Allan deviation of mod $\sigma_y \simeq 5 \times 10^{-17}$, and the frequency stability of the laser is mod $\sigma_y \simeq 2 \times 10^{-16}$ at around 1 second. Another way is to cool the optical cavity below 24 K [23]. The estimated thermal noise level of the cavity

is $\sigma_y \simeq 6 \times 10^{-18}$. The frequency instability of the laser is $\sigma_y \simeq 2 \times 10^{-14}$ at around 1000 second and $\sigma_y \simeq 2 \times 10^{-13}$ at around 1 second.

In view of the above results, the laser instability with these approaches, except for utilizing a very low temperature cavity, is close to another thermal noise limit, and thus using an optical cavity operated at a very low temperature is inevitable for any further improvements of the laser stability. However, the laser frequency instability with a very low-temperature cavity is currently far from the state-of-the-art frequency stability: about 1×10^{-16}. Moreover, the noise sources that limit the current instability are not determined, though the noise level of the thermal effects has been well discussed [23]. Other than the noises due to the thermal effects, there are many fundamental and technical noises that disturb frequency stabilization, such as the shot noise, acceleration noise, and residual amplitude modulation (RAM) noise. Therefore, we should research all of the noise sources, at least all of the noise sources that are well known as noise sources that disturb frequency stabilization, in order to show that the very low-temperature optical cavity is a strong tool for further improvements of the laser stability.

In this thesis, we constructed a frequency-stabilized laser with a cryogenic optical cavity, and estimated many noise sources that may limit the laser frequency stability, both systematically and quantitatively. By doing this systematic and quantitative evaluation, we showed the prospects to improve the laser stability with a cryogenic optical cavity operated at very low temperature. Using a very low-temperature optical cavity is one of strong methods for reducing the thermal noise. Thus, our work can be an important step for making an ultrastable laser.

The organization of this thesis is as follows: Chapter 2 introduces the method of frequency stabilization with a reference cavity. This chapter also shows the noise sources that disturb the stabilization of the laser frequency and their formulation. Chapter 3 describes the design and features of our experimental setup. The noise budget and the design stability of our experiment are also described in this chapter. Chapter 4 considers the performance of our experimental setup. Chapter 5 describes a noise estimation using the results of Chapter 4 and that of a direct stability measurement of our laser. Chapter 6 summarizes the results of this work. This chapter also explains future

prospects of the experiment.

Chapter 2
Frequency Stabilization

Laser frequency stabilization has been performed since the invention of a laser. Especially since 2000, the stability of the laser frequency has gradually improved. In this chapter, we give an overview of frequency stabilization.

We introduce the characteristic of a Fabry-Perot cavity (FPC) in Section 2.1. In the next Section, we discuss the fundamental limit of the frequency stability of a laser, called the Shawlow-Townes limit. We describe the Pound-Drever-Hall method for frequency stabilization in Section 2.3. We explain the relation between the frequency stability and the cavity length fluctuation in Section 2.4. Lastly, we discuss the noise sources of laser frequency stabilization in Section 2.5.

2.1 Fabry-Perot cavity

2.1.1 Transmittance and Reflectance

A Fabry-Perot cavity (FPC) consists of two mirrors facing each other, like in Fig. 2.1. A part of the input light to a FPC is transmitted through a front mirror, and plies between two mirrors. After that, the light is partly transmitted through a FPC, and the rest is reflected.

The amplitude of the reflected light can be calculated as

$$E_{\mathrm{r}} = Er_{\mathrm{F}} + Et_{\mathrm{F}}^2(-r_{\mathrm{E}})\mathrm{e}^{-2\mathrm{i}\delta}\sum_{n=0}^{\infty}\left(r_{\mathrm{F}}r_{\mathrm{E}}\mathrm{e}^{-2\mathrm{i}\delta}\right)^n = E\left(r_{\mathrm{F}} - \frac{r_{\mathrm{E}}t_{\mathrm{F}}^2\mathrm{e}^{-2\mathrm{i}\delta}}{1 - r_{\mathrm{F}}r_{\mathrm{E}}\mathrm{e}^{-2\mathrm{i}\delta}}\right), \quad (2.1)$$

where r_{F} and r_{E} are the amplitude reflectivity of the front and end mirrors; t_{F}

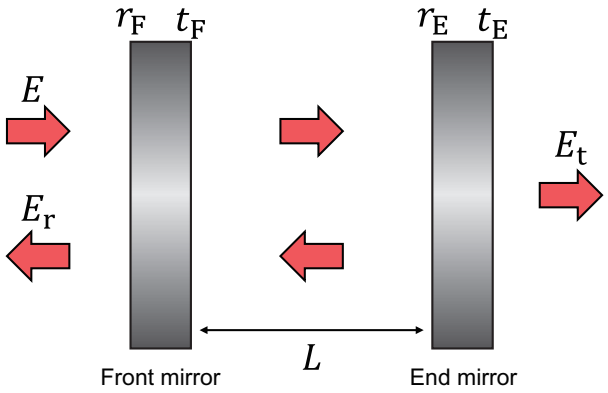

Figure 2.1: FP cavity

is the amplitude transmittance of the front mirror and $\delta = 2\pi L/\lambda$ is a phase change of the light traveling along the cavity length.

The amplitude of the transmitted light can be described as

$$E_t = Et_F t_E e^{-i\delta} \sum_{n=0}^{\infty} \left(r_F r_E e^{-2i\delta}\right)^n = E\frac{t_F t_E e^{-i\delta}}{1 - r_F r_E e^{-2i\delta}}, \tag{2.2}$$

where t_E is the amplitude transmittance of the end mirror.

We then obtain the amplitude reflectance and transmittance of a FPC, respectively, as follows:

$$r_{FPC} = r_F - \frac{r_E t_F^2 e^{-2i\delta}}{1 - r_F r_E e^{-2i\delta}}, \tag{2.3}$$

$$t_{FPC} = \frac{t_F t_E e^{-i\delta}}{1 - r_F r_E e^{-2i\delta}}. \tag{2.4}$$

The power of the reflected and transmitted light can be calculated as

$$P_r = |E_r|^2 = \frac{\{(r_F^2 + t_F^2)r_E - r_F\}^2 + 4r_F r_E(r_F^2 + t_F^2)\sin^2\delta}{(1 - r_F r_E)^2(1 + F\sin^2\delta)}|A|^2, \tag{2.5}$$

$$P_t = |E_t|^2 = \frac{t_F^2 t_E^2}{(1 - r_F r_E)^2(1 + F\sin^2\delta)}|A|^2, \tag{2.6}$$

where $F = 4r_F r_E/(1 - r_F r_E)^2$. The power of the transmitted light becomes

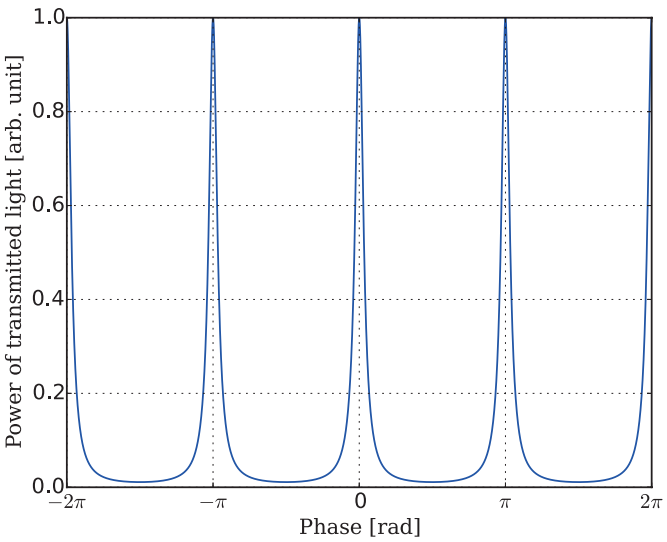

Figure 2.2: Example of the transmitted laser power. The Y-axis is normalized to make the maximum value 1.

maximum at $\delta = n\pi$. When the power of the transmitted light is maximum, the cavity state is called 'on resonance'.

2.1.2 Free spectral range and finesse

The power of the transmitted light has a sharp peak when the amplitude reflectance of the front and end mirrors satisfies $r_{\mathrm{F}},\ r_{\mathrm{E}} \sim 1$. Figure 2.2 shows an example of the transmitted laser power.

The laser frequency resonant with a FPC can be calculated as

$$\delta = \frac{2\pi L}{\lambda} = \frac{2\pi L\nu}{c} = n\pi \Leftrightarrow \nu = \frac{nc}{2L}. \tag{2.7}$$

The difference between the resonant frequencies next to each other is called the free spectral range (FSR); which can be described as

$$\nu_{\mathrm{FSR}} = \frac{c}{2L}. \tag{2.8}$$

Next, we calculate the full width at half maximum (FWHM) frequency,

ν_{FWHM}. Assuming that $r_{\mathrm{F}}, r_{\mathrm{E}} \sim 1$ and using Eq. (2.6), ν_{FWHM} satisfies the following equation:

$$\frac{1}{1 + F \sin^2 (2\pi\nu_{\mathrm{FWHM}}/\nu_{\mathrm{FSR}})} = \frac{1}{2}. \tag{2.9}$$

Then, if we assume $\nu_{\mathrm{FWHM}} \ll \nu_{\mathrm{FSR}}$, ν_{FWHM} can be written as

$$\nu_{\mathrm{FWHM}} = \frac{c}{\pi L \sqrt{F}}. \tag{2.10}$$

The ratio of ν_{FSR} and ν_{FWHM} is called the 'finesse', which can be expressed as

$$\mathcal{F} = \frac{\nu_{\mathrm{FSR}}}{\nu_{\mathrm{FWHM}}} = \frac{\pi\sqrt{r_{\mathrm{F}} r_{\mathrm{E}}}}{1 - r_{\mathrm{F}} r_{\mathrm{E}}}. \tag{2.11}$$

This is an index of the sharpness of the cavity resonance, and only depends on the amplitude reflectance of the front and end mirrors.

2.1.3 Reflectance and its differential function

Frequency stabilization is achieved using the reflected light of a FPC. We therefore describe the behavior of reflectance of the cavity in this subsection.

Using Eq. (2.3), the reflectance of a FPC and its differential as a function of δ can be written as

$$r_{\mathrm{FPC}} = r_{\mathrm{F}} - \frac{r_{\mathrm{E}} t_{\mathrm{F}}^2 \mathrm{e}^{-2\mathrm{i}\delta}}{1 - r_{\mathrm{F}} r_{\mathrm{E}} \mathrm{e}^{-2\mathrm{i}\delta}}, \tag{2.12}$$

$$r'_{\mathrm{FPC}} = \frac{-2\mathrm{i} t_{\mathrm{F}}^2 r_{\mathrm{E}} \mathrm{e}^{-2\mathrm{i}\delta}}{(1 - r_{\mathrm{F}} r_{\mathrm{E}} \mathrm{e}^{-2\mathrm{i}\delta})^2}. \tag{2.13}$$

Figure 2.3 shows the behavior of the reflectance as a function of δ.

When a FPC is on resonance, Eq. (2.12) and Eq. (2.13) can be changed to

$$r_{\mathrm{FPC}} = r_{\mathrm{F}} - \frac{t_{\mathrm{F}}^2 r_{\mathrm{E}}}{1 - r_{\mathrm{F}} r_{\mathrm{E}}}, \tag{2.14}$$

$$r'_{\mathrm{FPC}} = \frac{2\mathrm{i} t_{\mathrm{F}}^2 r_{\mathrm{E}}}{(1 - r_{\mathrm{F}} r_{\mathrm{E}})^2}. \tag{2.15}$$

Then, $|r_{\mathrm{FPC}}|$ becomes minimum and $|r'_{\mathrm{FPC}}|$ has the maximum value on reso-

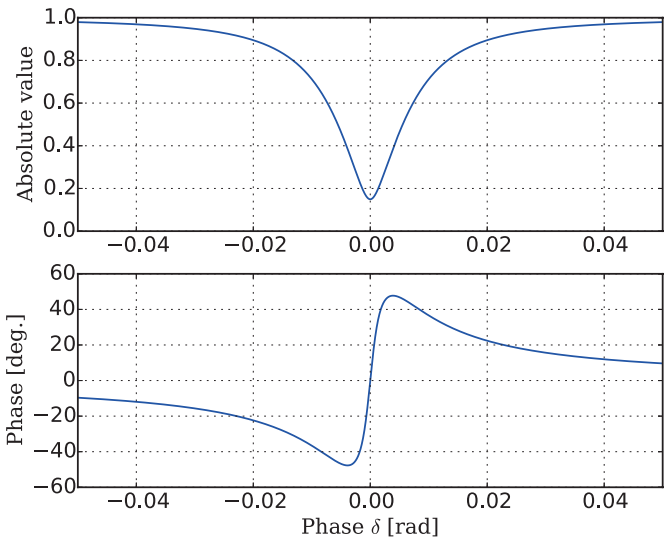

Figure 2.3: Absolute value and phase of the reflectance of a FPC. The parameters are $r_{\mathrm{F}} = r_{\mathrm{E}} = 0.99$, $t_{\mathrm{F}} = 0.13$.

nance.

2.1.4 Time constant of a cavity

When a FPC is in the steady state, the laser light stays in a FPC for a while. Now, considering the situation that the input laser is suddenly stopped, the laser beam staying in a FPC gradually reduces. In this part, we formulate the time scale of this decay.

The round-trip loss of the amplitude of the light inside a FPC can be written as

$$\Delta E_{\mathrm{intra}} = -(1 - r_{\mathrm{F}} r_{\mathrm{E}}) E_{\mathrm{intra}}. \tag{2.16}$$

Then, the attenuation rate satisfies the following equation:

$$\frac{\mathrm{d}E_{\mathrm{intra}}}{\mathrm{d}t} = -\frac{c}{2L}(1 - r_{\mathrm{F}} r_{\mathrm{E}}) E_{\mathrm{intra}}. \tag{2.17}$$

The solution to Eq. (2.17) can be described as

$$E_{\text{intra}} = E_0 \mathrm{e}^{-\frac{c}{2L}(1-r_{\text{F}}r_{\text{E}})t}, \tag{2.18}$$

where E_0 is the amplitude of the intra-cavity light when the laser is stopped. Therefore, the intra-cavity laser power can be calculated as

$$P_{\text{intra}} = |E_{\text{intra}}|^2 = |E_0|^2 \mathrm{e}^{-\frac{c}{L}(1-r_{\text{F}}r_{\text{E}})t}. \tag{2.19}$$

Now, we define the time constant of a FPC as the time that it takes to obtain the intra-cavity power, 1/e. Thus, the time constant, τ_{FPC}, can be written as

$$\tau_{\text{FPC}} = \frac{L}{c(1-r_{\text{F}}r_{\text{E}})}. \tag{2.20}$$

Using Eq. (2.11) and assuming $r_{\text{F}}, r_{\text{E}} \sim 1$, Eq. (2.20) can be rewritten as

$$\tau_{\text{FPC}} = \frac{1}{2\pi\nu_{\text{FWHM}}}. \tag{2.21}$$

Thus, we can know the necessary ν_{FWHM} to measure the time constant of a FPC.

2.1.5 Response for frequency fluctuation

When the input laser has some frequency fluctuation, we can describe the amplitude of the input laser as

$$E_{\text{in}} = E\mathrm{e}^{\mathrm{i}(\Omega t + \delta\phi(t))}, \tag{2.22}$$

where $\delta\phi(t)$ is the phase fluctuation, which satisfies

$$\frac{\partial\delta\phi(t)}{\partial t} = \delta\Omega(t) = 2\pi\delta\nu(t), \tag{2.23}$$

where $\delta\nu(t)$ is the laser frequency fluctuation. Assuming $\delta\phi(t) \ll 1$, Eq. (2.22) can be approximated as

$$E_{\text{in}} \simeq E\mathrm{e}^{\mathrm{i}\Omega t}(1 + \mathrm{i}\delta\phi(t)). \tag{2.24}$$

Then, using the inverse Fourier transformation (IFT),

$$\delta\phi(t) = \int_{-\infty}^{\infty} \tilde{\delta\phi}(\omega)\mathrm{e}^{\mathrm{i}\omega t}d\omega, \tag{2.25}$$

Eq. (2.24) can be rewritten as

$$E_{\mathrm{in}} = E\mathrm{e}^{\mathrm{i}\Omega t} + \mathrm{i}E\int_{-\infty}^{\infty} \tilde{\delta\phi}(\omega)\mathrm{e}^{\mathrm{i}(\Omega+\omega)t}\, d\omega. \tag{2.26}$$

Therefore, since the amplitude reflectance of the FPC in Eq. (2.12) is a function of the laser frequency, the amplitude of the reflected light can be expressed as

$$\begin{aligned} E_{\mathrm{r}} &= r(\Omega)E\mathrm{e}^{\mathrm{i}\Omega t} + \mathrm{i}E\int_{-\infty}^{\infty} r(\Omega+\omega)\tilde{\delta\phi}(\omega)\mathrm{e}^{\mathrm{i}(\Omega+\omega)t}\, d\omega \\ &= r(\Omega)E\mathrm{e}^{\mathrm{i}\Omega t}\left(1 + \mathrm{i}\delta\phi(t) + \mathrm{i}\int_{-\infty}^{\infty} \frac{r(\Omega+\omega)-r(\Omega)}{r(\Omega)}\tilde{\delta\phi}(\omega)\mathrm{e}^{\mathrm{i}(\Omega+\omega)t}\, d\omega\right). \end{aligned} \tag{2.27}$$

Here, $r(x)$ stands for $r_{\mathrm{FPC}}(x)$. Now, considering that the laser angular frequency, Ω, satisfies the resonant condition, Eq. (2.27) can be approximated as

$$\begin{aligned} E_{\mathrm{r}} &\simeq \left(r_{\mathrm{F}} - \frac{t_{\mathrm{F}}^2 r_{\mathrm{E}}}{1 - r_{\mathrm{F}}r_{\mathrm{E}}}\right)E\mathrm{e}^{\mathrm{i}(\Omega t + \delta\phi(t))} \\ &\times \left(1 - 2\int_{-\infty}^{\infty} \frac{t_{\mathrm{F}}^2 r_{\mathrm{E}}}{r_{\mathrm{F}} - r_{\mathrm{E}}(r_{\mathrm{F}}^2 + t_{\mathrm{F}}^2)}\frac{\sin\gamma}{1 - r_{\mathrm{F}}r_{\mathrm{E}}\mathrm{e}^{-2\mathrm{i}\gamma}}\mathrm{e}^{-\mathrm{i}\gamma}\tilde{\delta\phi}(\omega)\mathrm{e}^{\mathrm{i}\omega t}\, d\omega\right), \end{aligned} \tag{2.28}$$

where $\gamma = L\omega/c$. Since we can describe $\tilde{\delta\phi}(\omega)$ as

$$\tilde{\delta\phi}(\omega) = \frac{2\pi\tilde{\delta\nu}(\omega)}{\mathrm{i}\omega}, \tag{2.29}$$

Eq. (2.28) can be rewritten as

$$\frac{E_{\mathrm{r}}}{E_{\mathrm{in}}} = \frac{r_{\mathrm{F}} - r_{\mathrm{E}}(r_{\mathrm{F}}^2 + t_{\mathrm{F}}^2)}{1 - r_{\mathrm{F}}r_{\mathrm{E}}}\left(1 - \mathrm{i}\int_{-\infty}^{\infty} H_{\mathrm{FPC}}(\omega)\tilde{\delta\nu}(\omega)\mathrm{e}^{\mathrm{i}\omega t}\, d\omega\right), \tag{2.30}$$

where $H_{\mathrm{FPC}}(\omega)$ is the response function of a FPC for frequency fluctuation, and it can be expressed as

$$H_{\mathrm{FPC}}(\omega) = \frac{4\pi}{\omega} \frac{t_{\mathrm{F}}^2 r_{\mathrm{E}}}{r_{\mathrm{F}} - r_{\mathrm{E}}(r_{\mathrm{F}}^2 + t_{\mathrm{F}}^2)} \frac{\sin\gamma}{1 - r_{\mathrm{F}} r_{\mathrm{E}} \mathrm{e}^{-2\mathrm{i}\gamma}} \mathrm{e}^{-\mathrm{i}\gamma}. \tag{2.31}$$

Here, after calculating the absolute value of $H_{\mathrm{FPC}}(\omega)$, it can be written as

$$|H_{\mathrm{FPC}}(\omega)| = \frac{4\pi}{\omega(1 - r_{\mathrm{F}} r_{\mathrm{E}})} \frac{t_{\mathrm{F}}^2 r_{\mathrm{E}}}{r_{\mathrm{F}} - r_{\mathrm{E}}(r_{\mathrm{F}}^2 + t_{\mathrm{F}}^2)} \frac{|\sin\gamma|}{\sqrt{1 + F\sin^2\gamma}}. \tag{2.32}$$

Assuming $\gamma \ll 1$, Eq. (2.32) can be rewritten as

$$|H_{\mathrm{FPC}}(\omega)| = \frac{4\pi L}{c(1 - r_{\mathrm{F}} r_{\mathrm{E}})} \frac{t_{\mathrm{F}}^2 r_{\mathrm{E}}}{r_{\mathrm{F}} - r_{\mathrm{E}}(r_{\mathrm{F}}^2 + t_{\mathrm{F}}^2)} \frac{1}{\sqrt{1 + \left(\frac{\sqrt{F}L}{c}\omega\right)^2}}. \tag{2.33}$$

Then, the behavior of the frequency response of a FPC for frequency fluctuation is the same as that of a 1st-order low pass filter, and its cut-off frequency can be described as

$$f_{\mathrm{c}} = \frac{c}{2\pi L\sqrt{F}} = \frac{\nu_{\mathrm{FWHM}}}{2}. \tag{2.34}$$

Figure 2.4 shows the absolute value and phase of H_{FPC} as a function of the Fourier frequency.

2.2 Schawlow-Townes limit

The laser is a tool for making coherent light by using the stimulated emission radiation from atoms. Figure 2.5 shows a schematic diagram of the structure of a laser.

The fundamental frequency fluctuation the noise source of a laser is the spontaneous emission of atoms, which causes a random phase fluctuation of the stimulated emission [28]. The limit to the frequency stability of this effect is called the 'Schawlow-Townes limit'. The frequency fluctuation spectrum of

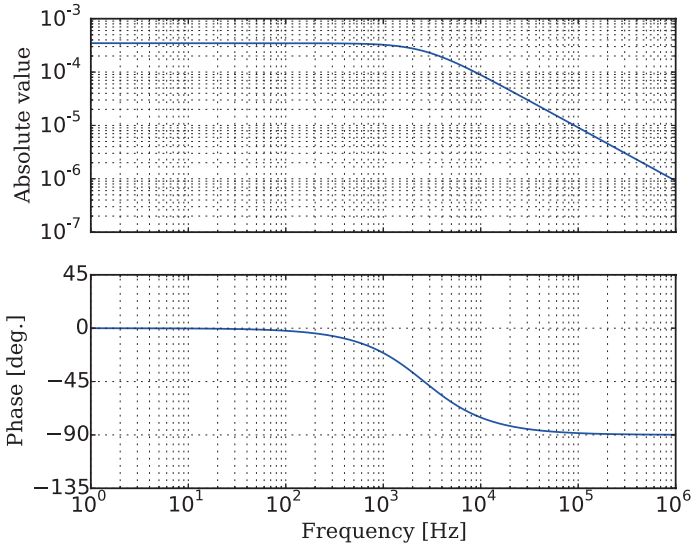

Figure 2.4: Absolute value and phase of the response function, $H_{\mathrm{FPC}}(\omega)$. The parameters used for this calculation are those in our optical cavity: $r_{\mathrm{F}} = r_{\mathrm{E}} = 0.999989$, $t_{\mathrm{F}} = 3.24 \times 10^{-3}$, and $L = 0.2$.

this effect can be described as [29]

$$\frac{\delta\nu}{\nu} = \nu_{\mathrm{FWHM}}\sqrt{\frac{2h}{P\nu}}\ [/\sqrt{\mathrm{Hz}}], \tag{2.35}$$

where ν_{FWHM}, h, P, and ν are the FWHM of an optical cavity, the Planck constant, the output laser power, and the frequency of a laser. Because of this limit, it is very difficult to construct a laser whose stability is below the 10^{-16} level.

However, it is well-known that we can reduce the frequency fluctuation below the Schawlow-Townes limit by using an active feedback system for frequency stabilization [29]. Thus, the stability of a laser can reach the 10^{-17} level of stability by using an external reference optical cavity.

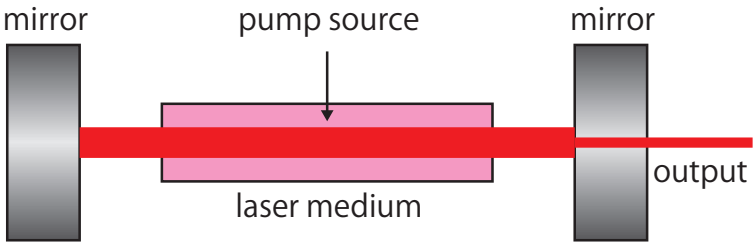

Figure 2.5: Schematic diagram of the structure of a laser. A laser consists of three parts: a laser medium, a pump source, and an optical cavity. The laser medium is the source of stimulated emission of radiation. The pump source is an energy source for making the inverted population of the laser medium. The optical cavity plays the role to store the light of the spontaneous emission and the stimulated emission.

2.3 Pound-Drever-Hall method

The Pound-Drever-Hall (PDH) method is a strong method for frequency stabilization using phase modulated light [30].

2.3.1 Error signal

Considering light with phase modulation, the amplitude of this light can be described to be

$$E_{\mathrm{in}}(t) = E\mathrm{e}^{\mathrm{i}(\Omega t + m\sin\omega_m t)} = E\sum_{-\infty}^{\infty} J_n(m)\mathrm{e}^{\mathrm{i}(\Omega+n\omega_m)t}, \tag{2.36}$$

where m is the modulation depth and ω_m is the angular frequency of the phase modulation. $J_n(m)$ is a Bessel function of the n-th order. Here, assuming that m is small, the amplitude of the light can be approximated as

$$E_{\mathrm{in}}(t) \simeq E\left(J_0(m)\mathrm{e}^{\mathrm{i}\Omega t} + J_1(m)\mathrm{e}^{\mathrm{i}(\Omega+\omega_m)t} - J_1(m)\mathrm{e}^{\mathrm{i}(\Omega-\omega_m)t}\right). \tag{2.37}$$

Equation (2.37) shows that there are three different components, called the carrier and sidebands, which have angular frequencies of Ω and $\Omega \pm \omega_m$.

This light enters the optical cavity. Noting that the amplitude reflectance of a FPC in Eq. (2.12) is a function of the angular frequency of light, the reflected power can be written as

$$P_{\mathrm{r}}(t) = \left| r(\delta\omega)J_0(m) + J_1(m)\left(r_+(\delta\omega)\mathrm{e}^{\mathrm{i}\omega_m t} - r_-(\delta\omega)\mathrm{e}^{-\mathrm{i}\omega_m t}\right)\right|^2 P_{\mathrm{in}}, \tag{2.38}$$

where $r(\delta\omega)$ stands for $r_{\mathrm{FPC}}(\delta\omega)$ and $r_\pm(\delta\omega) \equiv r(\delta\omega \pm \omega_m)$. $\delta\omega$ is the difference between the angular frequency of the input light and the nearest resonant angular frequency of a FPC. P_{in} is the input laser power. By expanding Eq. (2.38), we obtain

$$\begin{aligned}\frac{P_{\mathrm{r}}(t)}{P_{\mathrm{in}}} &= |r(\delta\omega)|^2 J_0(m)^2 + |r_+(\delta\omega)|^2 J_1(m)^2 + |r_-(\delta\omega)|^2 J_1(m)^2 \\ &+ 2J_0(m)J_1(m)\mathrm{Re}\left[\left\{r^*(\delta\omega)r_+(\delta\omega) - r(\delta\omega)r_-^*(\delta\omega)\right\}\mathrm{e}^{\mathrm{i}\omega_m t}\right] \\ &- 2J_1(m)^2\mathrm{Re}\left[r_+(\delta\omega)r_-^*(\delta\omega)\mathrm{e}^{2\mathrm{i}\omega_m t}\right].\end{aligned} \tag{2.39}$$

Here, considering demodulation of the reflected power by $\sin\omega_m t$, we obtain an error signal, ϵ, given by

$$\frac{\epsilon}{P_{\mathrm{in}}} = -2J_0(m)J_1(m)\mathrm{Im}\left[r^*(\delta\omega)r_+(\delta\omega) - r(\delta\omega)r_-^*(\delta\omega)\right]. \tag{2.40}$$

Figure 2.6 shows an example of the error signal as a function of the laser frequency. If the demodulation frequency, ω_m, is far from FWHM and $\delta\omega \ll \nu_{\mathrm{FWHM}}$, we can use the following approximations:

$$r_\pm(\delta\omega) \sim 1, \tag{2.41}$$

$$r(\delta\omega) \simeq r(0) + r'(0)\delta\omega. \tag{2.42}$$

Then, Eq. (2.40) can be rewritten as

$$\frac{\epsilon}{P_{\mathrm{in}}} = 4J_0(m)J_1(m)\mathrm{Im}[r'_{\mathrm{FPC}}(0)]\delta\omega. \tag{2.43}$$

Here, using Eq. (2.15), Eq. (2.43) can be rewritten as

$$\frac{\epsilon}{P_{\mathrm{in}}} = \frac{8t_{\mathrm{F}}^2 r_{\mathrm{E}} L}{(1 - r_{\mathrm{F}} r_{\mathrm{E}})^2 c} J_0(m)J_1(m)\delta\omega. \tag{2.44}$$

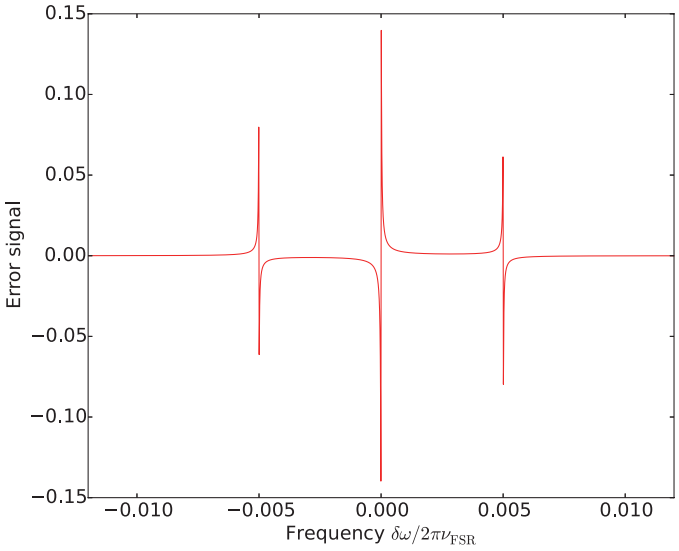

Figure 2.6: Example of an error signal according to the PDH method.

Thus, by assuming $r_{\mathrm{F}}, r_{\mathrm{E}} \sim 1$ and $t_{\mathrm{F}}^2 \simeq 1 - r_{\mathrm{F}}^2$, which means that the loss at the front mirror is sufficiently small, Eq. (2.44) can be further approximated as

$$\frac{\epsilon}{P_{\mathrm{in}}} = \frac{4J_0(m)J_1(m)\mathcal{F}}{\pi\nu_{\mathrm{FSR}}}\delta\omega. \tag{2.45}$$

Equation (2.45) shows that we can obtain a signal proportional to the difference between the laser frequency and the resonant frequency of the FPC. Thus, by feeding back the error signal to the laser frequency, we can make the laser frequency resonant with the frequency of the FPC.

2.3.2 Response for frequency fluctuation

The input laser with both some frequency fluctuation and phase modulation can be described as

$$E_{\mathrm{in}} = E\mathrm{e}^{\mathrm{i}(\Omega t + \delta\phi(t) + m\sin\omega_m t)}. \tag{2.46}$$

Using Eq. (2.37), Eq. (2.46) can be approximated as

$$E_{\rm in} \simeq E\left(J_0(m)\mathrm{e}^{\mathrm{i}(\Omega t+\delta\phi(t))} + J_1(m)\mathrm{e}^{\mathrm{i}((\Omega+\omega_m)t+\delta\phi(t))} - J_1(m)\mathrm{e}^{\mathrm{i}((\Omega-\omega_m)t)+\delta\phi(t)}\right). \tag{2.47}$$

Then, by considering the situation that the angular frequency, Ω, satisfies the resonant condition of a FPC, the amplitude of the reflected light can be expressed as

$$\begin{aligned} E_{\rm r} &\simeq r(0)J_0(m)\left(1-\mathrm{i}\int_{-\infty}^{\infty} H_{\rm FPC}(\omega)\tilde{\delta\nu}(\omega)\mathrm{e}^{\mathrm{i}\omega t}\right)E\mathrm{e}^{\mathrm{i}(\Omega \mathrm{t}+\delta\phi(\mathrm{t}))} \\ &+ J_1(m)\left(r_+(\delta\Omega)\mathrm{e}^{\mathrm{i}\omega_m t} - r_-(\delta\Omega)\mathrm{e}^{-\mathrm{i}\omega_m t}\right)E\mathrm{e}^{\mathrm{i}(\Omega \mathrm{t}+\delta\phi(\mathrm{t}))}, \end{aligned} \tag{2.48}$$

where $\delta\Omega$ is the angular frequency fluctuation, defined in Eq. (2.23). Now, assuming that the frequency fluctuation is much smaller than the modulation frequency, we can use the approximation $r_\pm(\delta\Omega)\sim 1$. Therefore, the reflected power can be calculated as

$$\frac{P_r}{P} = \left| r(0)J_0(m)\left(1-\mathrm{i}\int_{-\infty}^{\infty} H_{\rm FPC}(\omega)\tilde{\delta\nu}(\omega)\mathrm{e}^{\mathrm{i}\omega t}\,d\omega\right) + 2\mathrm{i}J_1(m)\sin\omega_m t\right|^2. \tag{2.49}$$

Demodulating the reflected power by $\sin\omega_m t$, we can obtain the error signal as

$$\frac{\epsilon}{P} = 4r(0)J_0(m)J_1(m)\mathrm{Re}\left[\int_{-\infty}^{\infty} H_{\rm FPC}(\omega')\tilde{\delta\nu}(\omega')\mathrm{e}^{\mathrm{i}\omega' t}\,d\omega'\right]. \tag{2.50}$$

This equation means that an error signal for the ω component of the frequency fluctuation reduces to the transfer function of a FPC. So, the error signal gets small when the frequency, $f,\ > \nu_{\rm FWHM}/2$.

2.4 Resonant frequency and cavity length

In the previous section, we explained that we can make laser frequency resonant with an optical cavity. Thus, the performance of the laser frequency stabilization is limited by the stability of the resonant frequency of the FPC.

The laser frequency that is resonant with an optical cavity can be written

as

$$\nu = \frac{nc}{2L}, \tag{2.51}$$

where n is the number of anti-nodes of the standing wave in an optical cavity. Here, considering a small fluctuation of the cavity length, δL, the variation of a resonant frequency of a FPC can be expressed as

$$\delta\nu = \frac{nc}{2}\frac{-\delta L}{L^2} = -\frac{\nu}{L}\delta L. \tag{2.52}$$

Equation (2.52) means that the resonant frequency of a FPC changes when the cavity length fluctuates. Therefore, the stability of the laser frequency that is tuned to the resonant frequency of a FPC is determined by the cavity-length fluctuation.

2.5 Noise source

In this section, we describe several noise sources of frequency stabilization.

2.5.1 Thermal noise

The spacer and mirrors of an optical cavity thermally fluctuate because these components have a finite temperature. The thermal fluctuation causes a cavity-length fluctuation, called 'thermal noise'. Thermal noise is one of the fundamental noises of laser frequency stabilization.

Thermal noise has been theoretically well studied and a theory, called fluctuation-dissipation theorem (FDT), tells that the thermal fluctuation is related to the loss of a system. According to the FDT, the power spectral density (PSD) of the thermal noise of a harmonic oscillator can be described as

$$G_x(\omega) = -\frac{4k_{\mathrm{B}}T}{M\omega}\mathrm{Im}\left[\frac{1}{\omega^2 - \omega_0^2\left\{1 + \mathrm{i}\phi(\omega)\right\}}\right] \ [\mathrm{m}^2/\mathrm{Hz}], \tag{2.53}$$

where $M, T, \omega_0, \phi(\omega)$ are the mass, temperature, resonant angular frequency, and loss angle of the harmonic oscillator. If we assume a structure damping

model, a loss angle can be written as

$$\phi(\omega) = \frac{1}{Q}, \tag{2.54}$$

where Q is the quality factor. We can therefore rewrite Eq. (2.53) as

$$G_x(\omega) = \frac{4k_\mathrm{B}T}{M\omega Q} \frac{\omega_0^2}{\omega^4 - 2\omega^2\omega_0^2 + \omega_0^4(1 + 1/Q^2)} \ [\mathrm{m}^2/\mathrm{Hz}]. \tag{2.55}$$

Figure 2.7 is an example of the thermal noise power spectral density. Then, by considering that the Fourier frequency is far from the resonant frequency and $Q \gg 1$, Eq. (2.55) can be approximated as

$$G_x(\omega) = \frac{4k_\mathrm{B}}{M\omega_0^2\omega} \frac{T}{Q} \ (\omega \ll \omega_0) \ [\mathrm{m}^2/\mathrm{Hz}], \tag{2.56}$$

$$G_x(\omega) = \frac{4k_\mathrm{B}\omega_0^2}{M\omega^5} \frac{T}{Q} \ (\omega \gg \omega_0) \ [\mathrm{m}^2/\mathrm{Hz}]. \tag{2.57}$$

In the case of a real cavity spacer and mirrors, they have many elastic modes. Thus, the thermal noise of these components is the summation of the thermal noises of all elastic modes. At frequencies below the resonant frequencies of the elastic modes, the thermal noise of a cylindrical cavity spacer, mirror substrate, and mirror coatings can be described as [25]

$$G_\mathrm{spacer}(f) = \frac{4k_\mathrm{B}T}{\omega Q_\mathrm{spacer}} \frac{L}{3\pi R^2 Y_\mathrm{spacer}} \ [\mathrm{m}^2/\mathrm{Hz}], \tag{2.58}$$

$$G_\mathrm{substrate}(f) = \frac{4k_\mathrm{B}T}{\omega Q_\mathrm{substrate}} \frac{1 - \sigma^2}{\sqrt{\pi} Y_\mathrm{substrate} w_0} \ [\mathrm{m}^2/\mathrm{Hz}], \tag{2.59}$$

$$G_\mathrm{coating}(f) = \frac{4k_\mathrm{B}T}{\omega Q_\mathrm{coating}} \frac{2(1+\sigma)(1-2\sigma)d}{\pi Y_\mathrm{substrate} w_0^2} \ [\mathrm{m}^2/\mathrm{Hz}], \tag{2.60}$$

where $Q_\mathrm{X}, Y_\mathrm{X}, R, \sigma$, and w_0 are the quality factor of X, Young's modulus of X, the radius of the cavity spacer, Poisson's ratio of a mirror substrate, and the beam spot size on the mirror. Then, the spectrum of the normalized frequency

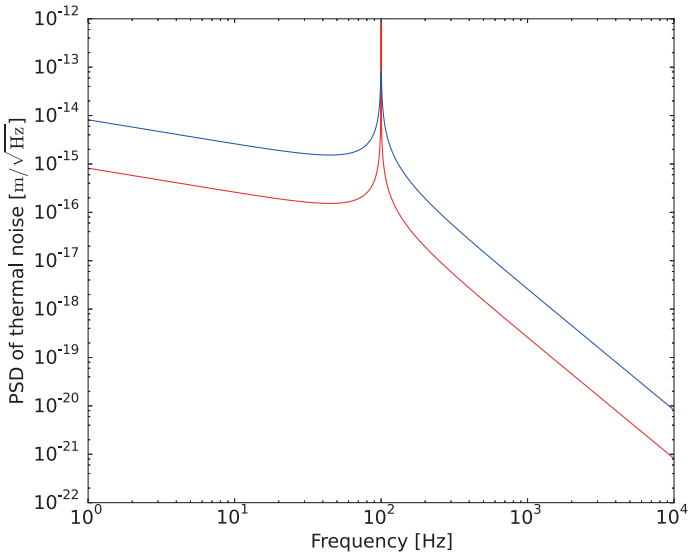

Figure 2.7: An example of a PSD of the thermal noise. The mass, M, is 1 kg, the temperature, T, is 300 K, and the resonant angular frequency, ω_0, is $2\pi \times 100$ rad/s. The blue and red lines have difference quality factors: $Q = 10^4$ for the red and $Q = 10^2$ for blue.

fluctuation of the thermal noise can be expressed as

$$\frac{\delta\nu}{\nu} = \frac{\sqrt{G_{\mathrm{spacer}}(f)}}{L} = \sqrt{\frac{4k_{\mathrm{B}}T}{\omega Q_{\mathrm{spacer}}} \frac{1}{3L\pi R^2 Y_{\mathrm{spacer}}}}\ [/\sqrt{\mathrm{Hz}}], \tag{2.61}$$

$$\frac{\delta\nu}{\nu} = \frac{\sqrt{G_{\mathrm{substrate}}(f)}}{L} = \sqrt{\frac{4k_{\mathrm{B}}T}{\omega Q_{\mathrm{substrate}}} \frac{1-\sigma^2}{\sqrt{\pi}L^2 Y_{\mathrm{substrate}} w_0}}\ [/\sqrt{\mathrm{Hz}}], \tag{2.62}$$

$$\frac{\delta\nu}{\nu} = \frac{\sqrt{G_{\mathrm{coating}}(f)}}{L} = \sqrt{\frac{4k_{\mathrm{B}}T}{\omega Q_{\mathrm{coating}}} \frac{2(1+\sigma)(1-2\sigma)d}{\pi L^2 Y_{\mathrm{substrate}} w_0^2}}\ [/\sqrt{\mathrm{Hz}}]. \tag{2.63}$$

2.5.2 Shot noise

The number of photons on a photodetector has some fluctuation since photons are quanta and this fluctuation is called the shot noise. This noise is also a fundamental noise for laser frequency stabilization.

The PSD of the shot noise can be expressed as

$$G_I(f) = 2eI_{\mathrm{DC}}\ [\mathrm{A}^2/\mathrm{Hz}], \tag{2.64}$$

where e is an elementary charge. I_{DC} is the DC current of a photodetector (PD). Using the DC laser power to a photodiode, P_{DC}, I_{DC} can be written as

$$I_{\mathrm{DC}} = \frac{eP_{\mathrm{DC}}\eta}{h\nu}, \tag{2.65}$$

where h is the Planck constant and η is the quantum efficiency (QE) of a PD. Thus, we can rewrite the PSD of the shot noise as

$$G_P(f) = \left(\frac{h\nu}{e\eta}\right)^2 G_I(f) = \frac{2h\nu}{\eta}P_{\mathrm{DC}}\ [\mathrm{W}^2/\mathrm{Hz}]. \tag{2.66}$$

In the PDH method, an error signal can be written as in Eq. (2.43). Then, the spectrum of the frequency fluctuation of the shot noise can be described as

$$\sqrt{G_\nu(f)} = \frac{1}{2\pi}\frac{\sqrt{G_P(f)}}{\epsilon/\delta\omega} = \frac{\sqrt{2h\nu P_{\mathrm{DC}}/\eta}}{8\pi P_{\mathrm{in}}J_0(m)J_1(m)\mathrm{Im}[r'(0)]}\ [\mathrm{Hz}/\sqrt{\mathrm{Hz}}]. \tag{2.67}$$

The laser power of the reflected light of the PDH method can be written as in Eq. (2.39). Then, the average power of the reflected light in the situation under a laser resonating with a FPC can be written as

$$P_{\mathrm{r}} = P_{\mathrm{DC}} = \left[r^2(0)J_0^2(m) + 2J_1^2(m)\right]P_{\mathrm{in}}. \tag{2.68}$$

Here, we use the approximation $r_\pm(0) \sim 1$. Therefore, Eq. (2.67) can be rewritten as

$$\sqrt{G_\nu(f)} = \frac{\sqrt{2h\nu\left[r^2(0)J_0^2(m) + 2J_1^2(m)\right]/(\eta P_{\mathrm{in}})}}{8\pi J_0(m)J_1(m)\mathrm{Im}[r'(0)]}\ [\mathrm{Hz}/\sqrt{\mathrm{Hz}}]. \tag{2.69}$$

Then, the spectrum of the normalized frequency fluctuation of the shot noise can be obtained as

$$\frac{\delta\nu}{\nu} = \frac{\sqrt{G_\nu(f)}}{\nu} = \frac{\sqrt{2h\left[r^2(0)J_0^2(m) + 2J_1^2(m)\right]/(\eta P_{\mathrm{in}}\nu)}}{8\pi J_0(m)J_1(m)\mathrm{Im}[r'(0)]}\ [/\sqrt{\mathrm{Hz}}]. \tag{2.70}$$

Here, if we assume $r_{\mathrm{F}}, r_{\mathrm{E}} \sim 1$ and the amplitude loss of an input mirror is small enough, Eq. (2.45) is satisfied. Thus, Eq. (2.70) can be approximated as

$$\frac{\delta\nu}{\nu} = \frac{1}{8J_0(m)L\mathcal{F}}\sqrt{\frac{hc\lambda}{\eta P_{\mathrm{in}}}}\ [/\sqrt{\mathrm{Hz}}]. \tag{2.71}$$

2.5.3 Acceleration noise

The acceleration of a FPC causes an elastic deformation, and changes the cavity length. The main source of the cavity acceleration is a seismic vibration.

A spectrum of the cavity length fluctuation caused by the acceleration of a FPC can be written as

$$\sqrt{G_x(f)} = AL\sqrt{G_a(f)}\ [\mathrm{m}/\sqrt{\mathrm{Hz}}], \tag{2.72}$$

where $\sqrt{G_a(f)}$ is the spectrum of the cavity acceleration and A is the coupling constant, called the vibration sensitivity, from acceleration to the laser frequency fluctuation. The vibration sensitivity depends on the shape of the cavity spacer, the way of cavity support, the material of a FPC and the cavity support, etc.

We can thus describe the spectrum of the normalized frequency fluctuation of the acceleration noise as

$$\frac{\delta\nu}{\nu} = \frac{\sqrt{G_x(f)}}{L} = A\sqrt{G_a(f)}\ [/\sqrt{\mathrm{Hz}}]. \tag{2.73}$$

2.5.4 Temperature-fluctuation noise

The temperature fluctuation of an optical cavity leads to thermal expansion, which changes the cavity length.

The spectrum of the temperature-fluctuation noise can be expressed as

$$\sqrt{G_x(f)} = \alpha L\sqrt{G_T(f)}\ [\mathrm{m}/\sqrt{\mathrm{Hz}}], \tag{2.74}$$

where α and $\sqrt{G_T(f)}$ are the coefficient of thermal expansion (CTE) and the temperature-fluctuation spectrum of the FPC. Then, the spectrum of the normalized frequency fluctuation of the temperature-fluctuation noise can be

written as

$$\frac{\delta\nu}{\nu} = \frac{\sqrt{G_x(f)}}{L} = \alpha\sqrt{G_{\mathrm{T}}(f)}\ [/\sqrt{\mathrm{Hz}}]. \tag{2.75}$$

2.5.5 Residual amplitude modulation noise

In practice, phase modulated light by using an EOM has a superfluous amplitude modulation at the same frequency of the phase modulation. There are many sources of this noise, such as scattered light, the temperature fluctuation of the EOM, etc. So, in this part, we show its effect.

Considering light with a phase and amplitude modulation, we can express its amplitude as [33]

$$\begin{aligned} E_{\mathrm{in}} &= E\left(1 + m_{\mathrm{a}}\sin(\omega_m t + \phi)\right)\mathrm{e}^{\mathrm{i}(\Omega t + m\sin\omega_m t)} \\ &\simeq E\left(1 + m_{\mathrm{a}}\sin(\omega_m t + \phi)\right)\left(J_0 + J_1\mathrm{e}^{\mathrm{i}\omega_m t} - J_1\mathrm{e}^{-\mathrm{i}\omega_m t}\right)\mathrm{e}^{\mathrm{i}\Omega t} \end{aligned} \tag{2.76}$$

where m_{a} is an amplitude-modulation index, and ϕ is a phase difference between a phase modulation and an amplitude modulation. J_0 and J_1 represent $J_0(m)$ and $J_1(m)$, respectively. Then, considering a laser frequency resonant with the FPC, the amplitude of the reflected light can be written as

$$\begin{aligned} E_{\mathrm{r}} &= E\left(r(0)J_0 + 2\mathrm{i}J_1\sin\omega_m t\right)\mathrm{e}^{\mathrm{i}\Omega t} \\ &- \mathrm{i}m_{\mathrm{a}}E\left(\mathrm{i}J_0\sin(\omega_m t + \phi) - r(0)J_1\cos\phi + J_1\cos(2\omega_m t + \phi)\right)\mathrm{e}^{\mathrm{i}\Omega t}. \end{aligned} \tag{2.77}$$

Here, we assume that $r_+(0),\ r_-(0),\ r_+(\omega_m),\ r_-(-\omega_m) \sim 1$. Therefore, a reflected power can be approximated as

$$\begin{aligned} \frac{P_{\mathrm{r}}}{P_{\mathrm{in}}} &\simeq (r^2(0)J_0^2 + 2J_1^2 - 2J_1^2\cos 2\omega_m t) \\ &+ 2\left(r(0)J_0^2 + 2r(0)J_1^2 + J_1^2\right)m_{\mathrm{a}}\cos\phi\sin\omega_m t \\ &+ 2\left(r(0)J_0^2 + J_1^2\right)m_{\mathrm{a}}\sin\phi\cos\omega_m t - 2J_1^2 m_{\mathrm{a}}\sin(3\omega_m t + \phi). \end{aligned} \tag{2.78}$$

Here, we use an approximation: $m_{\mathrm{a}}^2 \simeq 0$.

Then, by demodulating the reflected power by $\sin\omega_m t$, we can obtain the

error signal as

$$\epsilon_{\mathrm{RAM}} = 2\left[r(0)J_0^2 + 2r(0)J_1^2 + J_1^2\right] m_{\mathrm{a}} P_{\mathrm{in}} \cos\phi, \tag{2.79}$$

Therefore, the spectrum of an error signal of the RAM noise can be described as

$$\sqrt{G_{\epsilon_{\mathrm{RAM}}}(f)} = 2\left[r(0)J_0^2 + 2r(0)J_1^2 + J_1^2\right] P_{\mathrm{in}} \cos\phi \sqrt{G_{m_{\mathrm{a}}}(f)}, \tag{2.80}$$

where $\sqrt{G_{m_{\mathrm{a}}}(f)}$ is a spectrum of the amplitude-modulation index.

Therefore, the frequency fluctuation spectrum of the RAM noise can be expressed as

$$\sqrt{G_\nu(f)} = \frac{r(0)J_0^2 + 2r(0)J_1^2 + J_1^2}{4\pi J_0 J_1 \mathrm{Im}[r'(0)]} \cos\phi \sqrt{G_{m_{\mathrm{a}}}(f)}\ [\mathrm{Hz}/\sqrt{\mathrm{Hz}}]. \tag{2.81}$$

Thus, the spectrum of a normalized frequency fluctuation of the RAM noise can be written as

$$\frac{\delta\nu}{\nu} = \frac{\sqrt{G_\nu(f)}}{\nu} = \frac{r(0)J_0^2 + 2r(0)J_1^2 + J_1^2}{4\pi\nu J_0 J_1 \mathrm{Im}[r'(0)]} \cos\phi \sqrt{G_{m_{\mathrm{a}}}(f)}\ [/\sqrt{\mathrm{Hz}}]. \tag{2.82}$$

Now, assuming that $r_{\mathrm{F}},\ r_{\mathrm{E}} \sim 1$, and that the amplitude loss of the input mirror is sufficiently small, we can use the approximation $r(0) \sim 0$ and Eq. (2.45). Thus, Eq. (2.82) can be rewritten as

$$\frac{\delta\nu}{\nu} = \frac{J_1(m)\nu_{\mathrm{FSR}}}{4\nu J_0(m)\mathcal{F}} \cos\phi \sqrt{G_{m_{\mathrm{a}}}(f)}\ [/\sqrt{\mathrm{Hz}}]. \tag{2.83}$$

2.5.6 Residual gas noise

The inside of an optical cavity is held at a high vacuum for reducing any fluctuation of the refractive index in a FPC. However, due to residual gas, there is some fluctuation of the refractive index, which changes the resonant frequency of a reference cavity.

A PSD of an effective cavity length fluctuation of the residual gas noise

can be described as [34]

$$G_x(f) = \frac{2(n_0-1)^2}{(N_\mathrm{A}/V_0)\pi w^2}\left(\frac{p}{p_0}\right)\left(\frac{T_0}{T}\right)\frac{\tau_R}{2}\ [\mathrm{m}^2/\sqrt{\mathrm{Hz}}], \tag{2.84}$$

where n_0, A_0, V_0, p_0, T_0 are the refractive index of the gas, the Avogadro constant, and the volume, pressure, and temperature of the gas under the standard condition; τ_R is defined as

$$\tau_R \equiv \frac{w}{u_0}\sqrt{\frac{T_0}{T}}, \tag{2.85}$$

where u_0 is the mean speed of the gas molecules under the standard condition. Then, the spectrum of the normalized frequency fluctuation of the residual gas noise is

$$\frac{\delta\nu}{\nu} = \frac{\sqrt{G_x(f)}}{L} = \frac{n_0-1}{Lw}\sqrt{\frac{V_0}{\pi N_\mathrm{A}}\left(\frac{p}{p_0}\right)\left(\frac{T_0}{T}\right)\tau_R}\ [/\sqrt{\mathrm{Hz}}]. \tag{2.86}$$

2.5.7 Doppler noise

In general, we transfer the frequency-stabilized light from a FPC to an application system. However, while a frequency stabilized laser is transferred from a FPC to an application system, the beam undergoes some phase modulation because of the optical path-length fluctuation. This phase noise is called the Doppler noise.

Now, considering that the beam, $E\mathrm{e}^{\mathrm{i}\Omega t}$, travels some distance, the amplitude of the light after traveling is described as

$$E_\mathrm{AT} = E\mathrm{e}^{\mathrm{i}(\Omega t + \frac{nl}{\lambda})}, \tag{2.87}$$

where n and l are the refractive index and the path length along which the light travels. Then, the angular frequency of the light after traveling can be written as

$$\Omega' = \Omega + \left(\frac{\mathrm{d}n}{\mathrm{d}t}l + \frac{\mathrm{d}l}{\mathrm{d}t}n\right)\frac{1}{\lambda}. \tag{2.88}$$

The path-length fluctuation is mainly caused by seismic vibration and tem-

perature fluctuation of the optical path, and the fluctuation of the refractive index is basically caused by winds and sounds. From Eq. (2.88), the angular frequency fluctuation of the Doppler noise can be described in the frequency domain as

$$\tilde{\Omega}'(\omega) = \left(l\tilde{n}(\omega) + n\tilde{l}(\omega)\right)\frac{\mathrm{i}\omega}{\lambda}. \tag{2.89}$$

Then, the frequency-fluctuation spectrum of the Doppler noise can be expressed as

$$\sqrt{G_\nu(f)} = \frac{\mathrm{i}f}{\lambda}\sqrt{l^2 G_n(f) + n^2 G_l(f)}\ [\mathrm{Hz}/\sqrt{\mathrm{Hz}}], \tag{2.90}$$

where $G_n(f)$ and $G_l(f)$ are the spectrum of the reflective index and that of the path length, respectively. Therefore, the spectrum of the normalized frequency fluctuation of the Doppler noise is written as

$$\frac{\delta\nu}{\nu} = \sqrt{G_\nu(f)}/\nu = \frac{\mathrm{i}f}{c}\sqrt{l^2 G_n(f) + n^2 G_l(f)}\ [/\sqrt{\mathrm{Hz}}]. \tag{2.91}$$

2.5.8 Other noises

In this subsection, we consider those noise sources that are hard to be formulated.

Laser-power fluctuation noise

If the mirrors of a FPC have some absorption loss, a part of the input laser power changes to heat at the mirror surface. This effect makes the coatings locally heat up, which causes thermal expansion. In this way, the input laser-power fluctuation is changed to a cavity-length fluctuation.

However, formulating this effect has some difficulty, since any local heating of the coatings highly depends on the configuration of an optical cavity. We should thus check this noise effect in a real configuration of our experiment, and stabilize the intra-cavity laser power.

On the other hand, due to the very large thermal conductivity of monocrystalline silicon, the laser-power fluctuation noise should be small in our experiment. Moreover, since the laser-power fluctuation noise can be reduced by changing the operation parameters, like laser power, we can reduce the effect

of this noise after constructing our experimental setup. The laser-power fluctuation noise can therefore be well reduced for reaching a 10^{-17} level stability.

Circuit noise

For frequency stabilization, the electrical feedback system, consisting of a PD, amplifiers, and analog circuit filters, is necessary. However, such a system has some electrical noises, which causes frequency fluctuation of the laser.

There are many electrical noise sources such as the dark current of the PDs, noises of the op-amps, thermal noise of the resistance, etc. Then, the formulation of the circuit noise is very difficult. So, measuring the circuit noise in the frequency stabilization and estimating the noise level of an electrical circuit are necessary.

However, the circuit noise can be reduced by changing the operation parameters like the laser power and the modulation depth. We can therefore reduce this noise to below the 10^{-17} level.

2.6 Summary of this chapter

- We explained the properties of a FPC for characterizing the absolute frequency value and frequency fluctuation.
- The PDH method is a strong method for obtaining the signal of the difference between laser frequency and resonant frequency of an optical cavity using phase-modulated light.
- The stability of the laser frequency resonating with a FPC is determined by the cavity length stability of a reference cavity.
- We considered various noise sources of the cavity length fluctuation and the form of the spectrum of the normalized frequency fluctuation using the parameters of a FPC, laser power, etc.

Chapter 3
Experimental Design

In this chapter, we show the experimental setup for achieving 10^{-17} level frequency stabilization. We explain the design concept of our experiment in Section 3.1. We describe the noise budget of our experimental setup in Section 3.2. Several designs mentioned in this chapter were developed by my collaborators: Dr. Yoichi Aso and Dr. Noriaki Ohmae. Their contributions are shown in each subsection.

3.1 Design concept

3.1.1 Overview of the experimental design

A schematic of our experimental setup for the frequency stabilization is shown in Fig. 3.1. Outside the cryostat, there is an input laser system on an optical table. In this part, we produce phase-modulated light and transport it to the cryostat. Moreover, there are also Doppler noise-cancellation systems [35] located on this optical table.

In a vacuum chamber, there are several components for reducing any cavity length fluctuation. At the bottom of a cryostat, there are rubber legs for high-frequency vibration isolation. On top of them, there is an active vibration isolation table (AVIT) for low frequency vibration reduction. There are some optics on the AVIT for matching the laser mode to the cavity eigen mode. There are also thermal-isolation stacks on the AVIT for making a temperature gradient from 300 K to 18 K, which is close to the zero-cross point temperature of the CTE of monocrystalline silicon. The optical cavity is put on thermal-

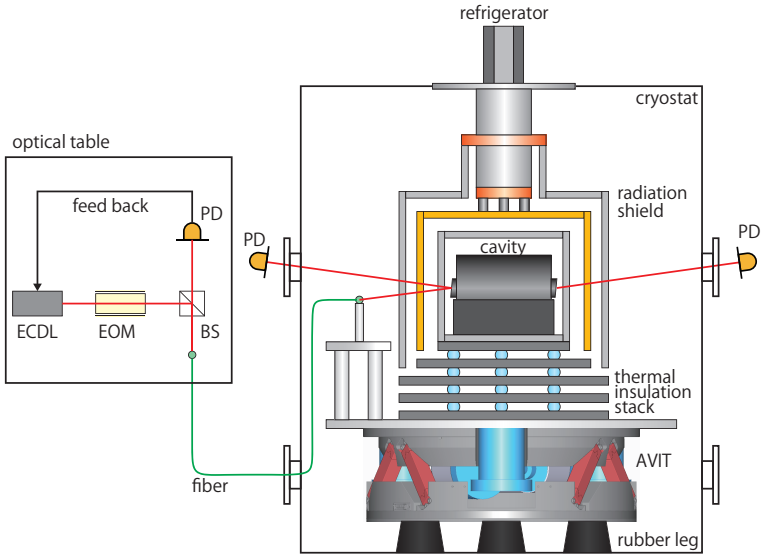

Figure 3.1: Schematic of our experimental setup. See the text for details.

isolation stacks, and there are three radiation shields around it. At the top of the cryostat, there is the refrigerator for cooling the reference cavity.

3.1.2 Silicon optical cavity

The optical-cavity design is very important for reducing several noises, such as the thermal noise, the acceleration noise, and the temperature fluctuation noise. The cavity of our experiment was mainly designed by Dr. Aso. He decided on the material of the cavity, the shape of the cavity spacer, the direction of the crystal axis, etc.

One of the fundamental noises for the frequency stabilization is the thermal noise of the cavity components. Thus, reducing the thermal noise is necessary for making an ultrastable laser. Considering Eq. (2.61), Eq. (2.62), and Eq. (2.63), the main approaches for reducing the thermal noise are as follows:

1. using a high mechanical quality factor material (large Q),
2. cooling the optical cavity (small T),
3. using a long optical cavity (large L).

Therefore, we use monocrystalline silicon, which has a very high mechanical quality factor [36] for the material of the cavity spacer and mirrors. Moreover, we cool the optical cavity to around 18 K. Since the mechanical quality factor of monocrystalline silicon at a very low temperature is larger than that at a room temperature [36], we can reduce the thermal noise effectively. Furthermore, since monocrystalline silicon has a zero-cross point temperature of the CTE at around 18 K, reducing the temperature-fluctuation noise is also expected [23, 37]. The cavity length is 20 cm, which is long enough for our goal.

Considering Eq. (2.62) and Eq. (2.63), it is also useful to make the beam-spot size large for reducing the thermal noise of the mirrors and coatings. Therefore, we use a curved mirror, whose radius of curvature is 1 m for the input mirror and a flat mirror for the end mirror of the reference cavity (see Appendix A). Moreover, the larger Poisson's ratio is also effective for reducing the thermal noise from the mirror substrates and coatings. Since the Poisson ratio of monocrystalline silicon along the [100] axis is larger than that along the [111] axis [39], the spacer and mirrors are made of monocrystalline silicon with a [100] orientation along the optical axis of the cavity.

Taking into account Eq. (2.71) and Eq. (2.83), a larger finesse is better for reducing the shot noise and RAM noise. Therefore, the coatings of the mirrors are dielectric multilayers of SiO_2 and Ta_2O_5, which have been currently used for a very high-finesse cavity.

The optical cavity of our experiment is shown in Fig. 3.2. The mirrors are optically contacted to the cavity spacer. The radius of the cavity spacer is 20 cm long.

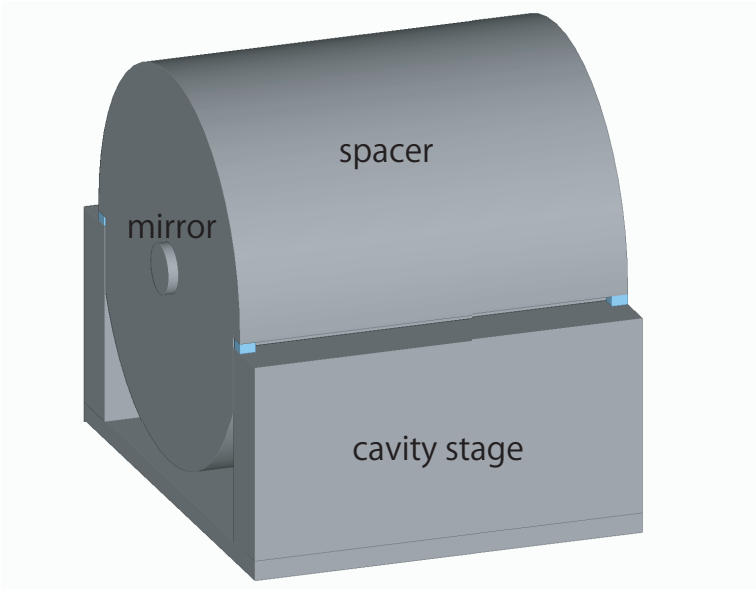

Figure 3.2: Image of a silicon optical cavity. The cavity spacer and mirrors are all made of silicon. They are supported by four rubber legs (blue part of this figure). These are on a silicon stage for reducing any cooling stress due to the difference in the CTE between the optical cavity and the cavity stage.

3.1.3 Vibration isolation system

The acceleration noise is one of the most problematic technical noise sources for the frequency stabilization. There are therefore two vibration isolation systems in our setup.

One is the passive vibration isolation system (PVIS) using rubber legs. At the bottom of the cryostat, there are three rubber legs for high-frequency vibration isolation. At the frequency which is higher than the resonant frequency of the rubber legs, seismic vibration is hardly transferable to the top of them.

The other is the active vibration isolation system (AVIS) using a hexapod-type active vibration isolation table (AVIT). Figure 3.3 is an image of the AVIT. It has six legs and there are PZTs in each leg. Thus, we can control six degrees of freedom to change the voltage applied to the PZTs. In addition, there are six vibration sensors on the top plate of the AVIT for measuring the vibration. Therefore, by feeding back these vibration sensors' signals to the voltage applied to PZTs, we can reduce any vibration at the top of the AVIT.

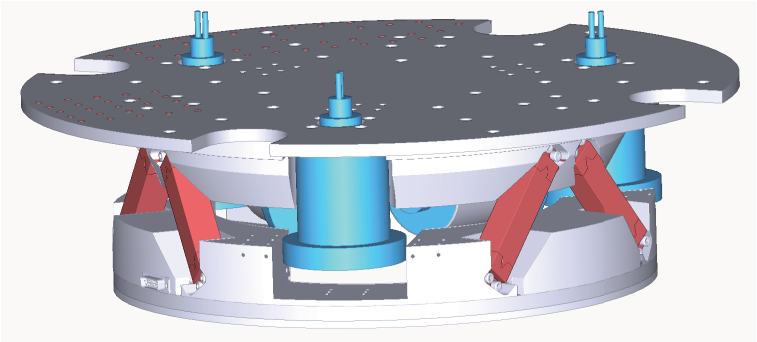

Figure 3.3: Design of the AVIT. Red parts are PZT legs and blue structures are aluminum pots for maintaining the pressure around the vibration sensors at atmospheric pressure.

Such an AVIS enables us to reduce any vibration at low frequencies easily, while low-frequency vibration reduction using a PVIS is difficult.

Moreover, the AVIS can easily reduce vibration from a refrigerator, while it's difficult for the PVIS to decrease, because such vibration is directly transmitted to a cooling target. Thus, we can reduce vibration not only from seismic motion, but also from a refrigerator.

3.1.4 Cryogenic refrigerator

The refrigerator can be a problematic vibration and temperature-fluctuation source. We thus use a helium recondensation-type pulse tube refrigerator. It is expected to be a low vibration and temperature fluctuation refrigerator. This cryogenic refrigerator was selected by Dr. Aso to reduce these noises.

Figure 3.4 is a schematic diagram of our refrigerator. The vibration level of a cold head of the pulse tube-type refrigerator is smaller than that of other refrigerators like a Stirling refrigerator, because the pulse tube-type cryocooler has no fundamental vibration section at the cryogenic part. Moreover, since there is no mechanical connection between the cold heads and the cooling targets in our refrigerator, the vibration of cold heads does not easily transfer to an optical cavity [38].

A helium recondensation-type pulse tube refrigerator also has a benefit concerning the temperature-fluctuation noise. A pulse tube refrigerator makes

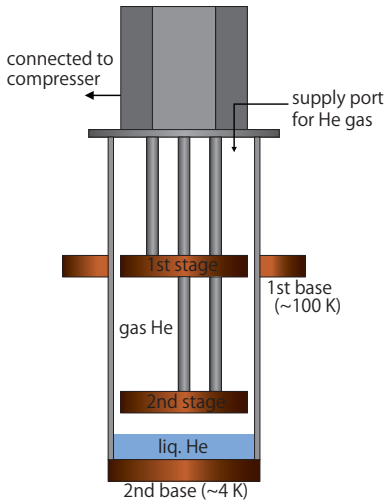

Figure 3.4: Schematic diagram of the refrigerator used in our experiment. Cold heads of the refrigerator are inside of the chamber. This chamber is filled with He gas. The 1st stage and the 1st base perform heat exchange via He gas. If the temperature of the 2nd stage is low enough, a part of He gas is changed to liq. He, cooling the 2nd base. The temperature of the 1st base is about 100 K and that of the 2nd base is about 4 K.

the temperature fluctuation synchronize with its compression. However, by using liquid helium to transfer heat, temperature fluctuation of the 2nd stage hardly transmits to the 2nd base because the liquid helium works as a heat bath.

3.1.5 Thermal isolation system

The temperature-fluctuation noise is one of the most problematic noises for frequency stabilization.

In our experiment, we use an AVIT for active vibration reduction. However, since the vibration sensor on AVIT cannot be used at the cryogenic temperature, only the part around an optical cavity can be cooled. We thus use thermal-isolation stacks, which are original structures in our experiment for making a high-temperature gradient between a reference cavity and the AVIT.

Figure 3.5 is a schematic diagram of the thermal-isolation stacks. The

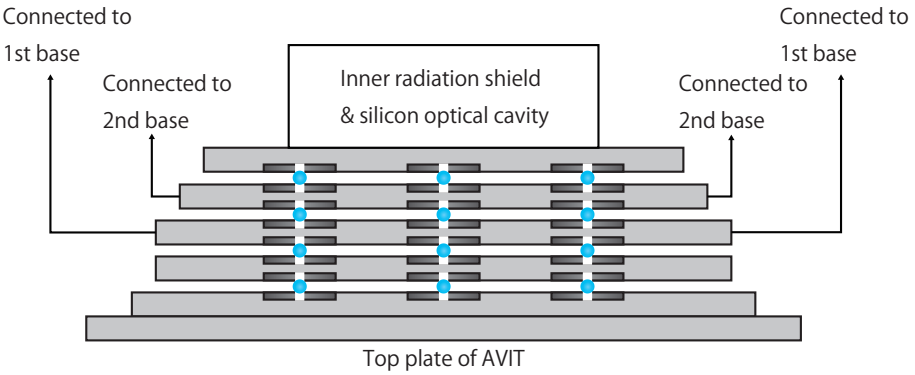

Figure 3.5: Structure of thermal-isolation stacks. The gray parts are aluminum plates coated by nickel. The dark black parts are SUS inserts that have a 3 mm diameter hall. The blue parts are 5 mm BK7 spheres. There are five stacks; the third floor is connected to the 1st base of the refrigerator and the forth floor is linked to the 2nd base of the refrigerator. The temperatures of the 4th and 5th floors are about 18 K and that of the 3rd floor is about 100 K. The temperature of the top plate of an AVIT is almost the same as the room temperature.

thermal-isolation stacks are made of three parts: aluminum plates, SUS inserts, and glass balls. Aluminum plates are coated by nickel for making the emissivity low. A SUS insert has a small hall, and a glass ball is put on this hall. In this structure, since the supporting surface between the hall and the sphere is a circle, the lower plate and upper plate has an ideal one-dimensional connection. Then, the thermal conduction between two plates can be very small, and it is possible to make a high-temperature gradient between them. The conceptual idea of this thermal-isolation stacks was invented by Dr. Aso.

Another enemy for cooling is heat transfer from radiation. The heat flux from radiation can be described as

$$Q = \varepsilon \sigma_{\mathrm{B}} A T^4, \tag{3.1}$$

where ε, σ_{B}, A, and T are the emissivity, Stefan-Boltzmann constant, surface area, and temperature. Thus, even if only a small area sees 300 K parts, the heat flux becomes very large and disturbs the cooling. Then, there are three radiation shields in our experiment to reduce the heat flux from radiation.

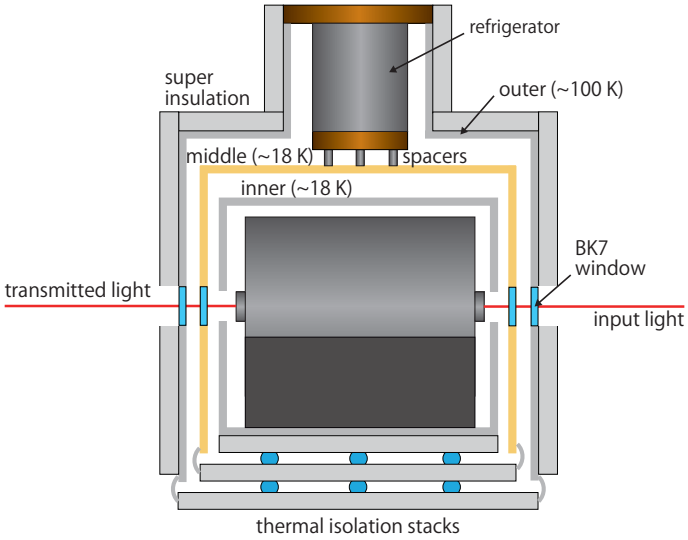

Figure 3.6: Schematic diagram of the radiation shields. The middle and outer radiation shields are connected to stacks with thin OFC wires and aluminum foils for being able to move an AVIT independently from the radiation shields. The temperature of the outer shield is 100 K, and those of inner and middle shields are 18 K.

Figure 3.6 shows a schematic diagram of the radiation shields. An inner radiation shield neighbors an optical cavity, and its temperature is almost the same as that of a reference cavity. It is made of aluminum for reducing the mass of the inner radiation shield because we should decrease the mass to below the allowable level for the AVIT. A middle radiation shield is connected to the 2nd base of the refrigerator through the SUS spacer which plays a role for making a temperature gradient between the 2nd base and the middle radiation shield. It is made of oxide-free copper (OFC), which has very high thermal conductivity. Moreover, the surface of the middle radiation shield is coated by gold because OFC is easily oxidized. Furthermore, since the emissivity of gold is very small, it can reduce the heat flux from the radiation. An outer radiation shield is connected directly to the 1st base of the refrigerator. It is made of aluminum, and there are super insulation sheets around it for reducing the heat flux from the radiation.

Radiation shields have halls for the input and transmitted light. However, even though the halls are very small, the heat flux from the room-temperature

part is very severe. We therefore use BK7 glass windows on the outer and middle radiation shields. BK7 has a high transmittance of around 1.4 μm and a low transmittance of over 2 μm. Therefore, only a laser beam can be transmitted through BK7 windows, and we can reduce the heat flux from radiation.

3.1.6 Input and output optics

The input and output optics is optics outside of the cryostat. This part has many roles, for example sending laser light to the cavity, obtaining PDH signals for frequency stabilization, and reducing several noises. One of the most important roles in this part is to measure any instability of our laser. Since the laser instability is evaluated by measuring the beat frequency between two lasers, we should prepare another laser that is no less stable than our laser. Such a stable laser was invented Dr. Ohmae. We can therefore measure the frequency stability of our laser directly.

Our laser source is an external cavity diode laser (ECDL); its wavelength is about 1397 nm for applying to a Sr optical lattice clock. Figure 3.7 is a schematic diagram of our ECDL. Mainly, there are three components: the laser diode (LD), the diffraction grating, and the PZT actuator. When the light of the LD enters the diffraction grating, the 1st-order diffracted light returns to the LD. The returned light resonates with the cavity configured by the diffraction grating, and the LD and provides the optical feedback to the LD. When we change the angle of the diffraction grating using the PZT actuator, the wavelength of the resonated beam is changed. Moreover, we can change the frequency of the ECDL to change the current applied to the LD. Therefore, the wavelength of the ECDL is tunable over a wide range, for example several tens of nanometers. In our ECDL, we use a grating with the high diffraction efficiency: about 50%. The output power is about 70 mW at 1397 nm when the supply current to the LD is about 500 mA.

Figure 3.8 is the design of the optical system used in our experiment. We make phase modulated light with the EOM, and obtain the PDH signal using the PD1. The PDH signal is fed back to the PZT actuator and the LD current, and our laser frequency is stabilized to the resonant frequency of the optical

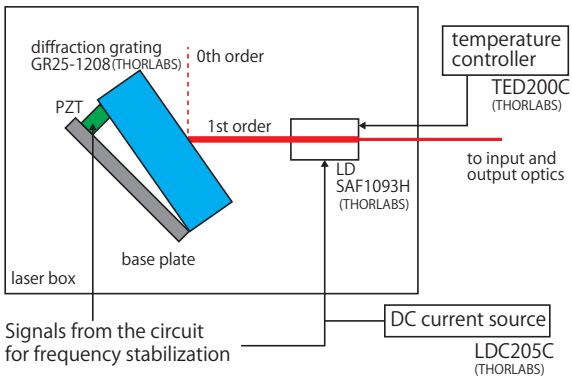

Figure 3.7: Schematic diagram of our ECDL. A pink part is a laser diode, and a blue part is a diffraction grating. A green part is the PZT actuator. These components are put in the laser box for blocking winds and sounds. The LD and the PZT are connected with the feedback circuit for the frequency stabilization (details in Appendix C). The temperature of the LD is stabilized using the temperature controller. Several model numbers of the components are shown in this figure.

cavity. The frequency fluctuations at low frequencies and high frequencies are fed back to the PZT and the LD, respectively. Doppler-noise cancellation using the differential arm length Michelson interferometer (DAMI) [35] is achieved using the signals of the PD2 and the PD3. These signals are fed back to the RF frequencies applied to the AOM1 and AOM2. Details of the Doppler noise cancellation are given in Section 3.2.7. Laser-frequency stabilization is achieved by feeding back the signal of the PD5 to the amplitude of the RF signal applied to the AOM1. Direct frequency instability evaluation is achieved by measuring the beat frequency between our laser and the stable laser using the PD6. The instability of the stable laser is at the 10^{-16} level on a time scale from 0.1 second to 10 second when the linear drift of the laser is subtracted. The beat frequency is measured using the frequency counter, and the Allan deviation of the beat signal is calculated according to its definition (see Appendix B). Our cavity mirrors have some wedge for separating the reflected light at the HR surface from that at the AR surface. The reflected light at the AR surface is detected by the PD4, and used for the RAM noise estimation.

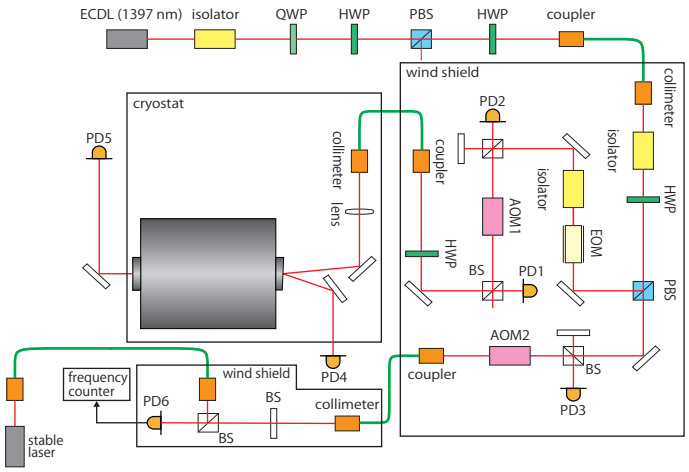

Figure 3.8: Design of the input and output laser system. A stable laser has a 10^{-16} level of frequency stability. All optical fibers in this experiment are polarization-maintaining fibers. The PD6 is a detector for measuring the beat signals between our laser and the stable laser. The beat frequency is measured by a frequency counter.

3.2 Noise budget

In this section, we show the noise budget of our experimental design.

3.2.1 Thermal noise

The thermal noise of a FPC depends on the materials composing the optical cavity and its configuration, such as the cavity length, and curvatures of mirrors. Table 3.1 gives our experimental design parameters that determine the thermal noise levels. Using these parameters and Eq. (2.61) to Eq. (2.63), the thermal noise levels can be calculated as

$$\frac{\delta\nu}{\nu} \simeq \frac{7.2\times10^{-20}}{\sqrt{f}} \ /\sqrt{\text{Hz}} \ \text{(spacer)}, \tag{3.2}$$

$$\frac{\delta\nu}{\nu} \simeq \frac{2.3\times10^{-18}}{\sqrt{f}} \ /\sqrt{\text{Hz}} \ \text{(substrate)}, \tag{3.3}$$

$$\frac{\delta\nu}{\nu} \simeq \frac{2.0\times10^{-17}}{\sqrt{f}} \ /\sqrt{\text{Hz}} \ \text{(coatings)}. \tag{3.4}$$

cavity length	$L = 0.2$ m
cavity radius	$R = 0.1$ m
Q factor	$Q_{\text{spacer}} = Q_{\text{substrate}} = 1.0 \times 10^7$ [36]
	$Q_{\text{coating}} = 2.5 \times 10^3$ [25]
Young's modulus	$Y_{\text{spacer}} = Y_{\text{substrate}} = 1.69 \times 10^{11}$ Pa [39]
Poisson's ratio	$\sigma = 0.28$ [39]
beam spot size on a front mirror	$w_{\text{F}} = 4.2 \times 10^{-4}$ m
beam spot size on an end mirror	$w_{\text{E}} = 4.7 \times 10^{-4}$ m
thickness of coatings	$d = 1.2 \times 10^{-5}$ m

Table 3.1: Parameters for calculating the thermal noise.

3.2.2 Shot noise

The shot-noise level depends on the cavity length, input laser power, wavelength, modulation depth, and the QE of a PD. Table 3.2 gives our experimental parameters that determine the shot-noise level. Then, using Eq. (2.71), we can calculate the shot-noise level as

$$\frac{\delta\nu}{\nu} \simeq 3.6 \times 10^{-19} \, /\sqrt{\text{Hz}}. \tag{3.5}$$

wave length	$\lambda = 1.4 \times 10^{-6}$m
cavity length	$L = 0.2$ m
cavity Finesse	$\mathcal{F} = 1.0 \times 10^5$
modulation depth	$m = 0.27$ rad
input laser power	$P = 1.0 \times 10^{-4}$ W
QE of a PD	$\eta = 0.88$

Table 3.2: Parameters for calculating the shot noise.

3.2.3 Acceleration noise

The noise level of the acceleration noise is determined by the vibration sensitivity and the acceleration of a reference cavity.

There are too many factors to determine the vibration sensitivity theoretically, for example, the configuration of a cavity spacer, support points, and support materials of an optical cavity. However, a vibration sensitivity below 1×10^{-11} /(m/s^2) in all translational axes was achieved in 2012 [12]. We therefore assume the vibration sensitivity of our cavity design to be 1×10^{-11} /(m/s^2) in all translational axes.

The seismic vibration level depends on the place, time, weather, and so on. However, the typical RMS seismic motion spectrum density can be described as [40]

$$\sqrt{G_x(f)} \simeq \frac{1.0 \times 10^{-7}}{f^2} \ \mathrm{m}/\sqrt{\mathrm{Hz}}. \tag{3.6}$$

Then, the acceleration from the seismic motion can be expressed as

$$\sqrt{G_\mathrm{a}(f)} = (2\pi f)^2 \sqrt{G_x(f)} = 3.9 \times 10^{-6} \ (\mathrm{m/s^2})/\sqrt{\mathrm{Hz}}. \tag{3.7}$$

Since the vibration at the place of a FPC is isolated passively and actively, the acceleration of a reference cavity is smaller than Eq. (3.7).

The passive vibration isolation can reduce the vibration at high frequency. The equation of motion of the mass on the rubber legs can be written as

$$\ddot{x} + 2\xi\omega_0\dot{x} + \omega_0^2(x - X) = 0, \tag{3.8}$$

where x and X are the displacements of the upper and lower parts of the rubber legs, respectively. ω_0 is the resonant angular frequency and ξ is a damping ratio. In the frequency domain, Eq. (3.8) can be written as

$$\left(-\omega^2 + 2\mathrm{i}\xi\omega_0\omega + \omega_0^2\right)\tilde{x} = \omega_0^2\tilde{X}. \tag{3.9}$$

Then, the transfer function of the vibration can be described as

$$H_\mathrm{P}(\omega) = \frac{\tilde{x}}{\tilde{X}} = \frac{\omega_0^2}{-\omega^2 + \mathrm{i}\omega\omega_0/Q + \omega_0^2}, \tag{3.10}$$

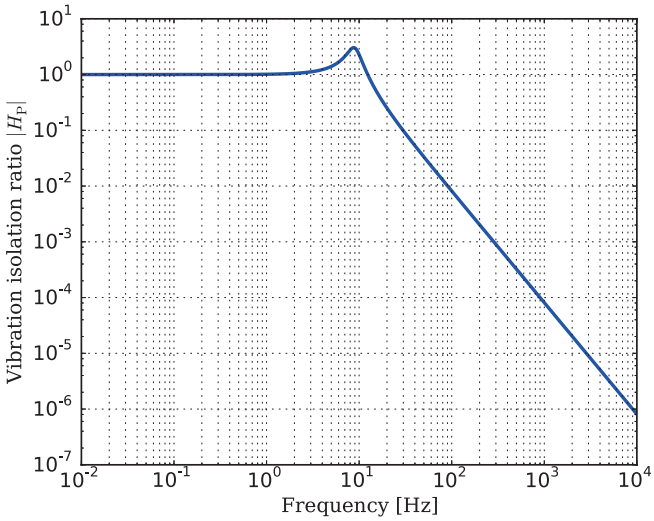

Figure 3.9: Example of the transfer function of passive vibration isolation. $\omega_0 = 2\pi \times 9$ rad/s and $Q = 3.0$. These are the same values as the design parameters.

where $Q = 1/2\xi$ is the Q factor. Figure 3.9 is an example of the vibration isolation ratio of the passive vibration isolation using the rubber legs. Thus, the vibration level on the rubber legs is smaller than that on ground at high frequency.

On the other hand, active vibration isolation reduces the seismic vibration at low frequency. The designed open-loop transfer function of an AVIS is as follows:

$$H_A(f) = G_0 \frac{if\,(1 + if/f_0)\,(1 + if/f_1)}{(1 + if/f_2)^4}. \tag{3.11}$$

Figure 3.10 shows the absolute value of the designed $H_A(f)$.

Then, the acceleration noise level of our experimental design can be written as

$$\frac{\delta\nu}{\nu} = 3.9 \times 10^{-17} \left| \frac{H_P}{1 + H_A} \right|. \tag{3.12}$$

Table 3.3 shows the parameters for calculating the acceleration noise.

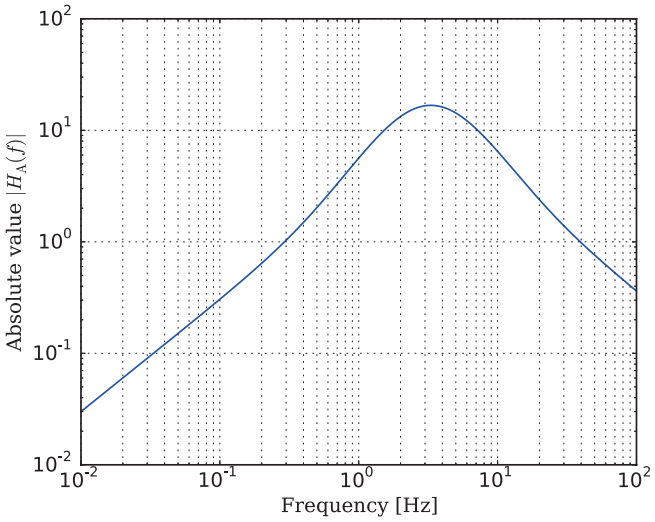

Figure 3.10: Absolute value of the designed open-loop transfer function of an AVIS. $f_0 = 0.5$ Hz, $f_1 = 20$ Hz, $f_2 = 3.3$ Hz, and $G_0 = 3$

vibration sensitivity	$A = 10^{-11}$ /(m/s^2)
seismic acceleration spectrum	$\sqrt{G_a(f)} = 3.9 \times 10^{-6}$ (m/s^2)/$\sqrt{\text{Hz}}$
Passive vibration isolation	$\omega_0 = 2\pi \times 9$ rad/s
	$Q = 3.0$
Active vibration isolation	$G_0 = 3$
	$f_0 = 0.5$ Hz
	$f_1 = 20$ Hz
	$f_2 = 3.3$ Hz

Table 3.3: Parameters for calculating the acceleration noise.

3.2.4 Temperature-fluctuation noise

The temperature-fluctuation noise depends on the CTE and the temperature fluctuation of an optical cavity.

Figure 3.11 shows the thermal structure of our experiment. The sources of temperature fluctuation of a reference cavity are the temperature of the laboratory, the 1st stage, and the 2nd stage of the refrigerator. However, the temperature fluctuations of the 1st stage and the laboratory are transferred through an outer shield. We thus don't have to consider the temperature fluctuations of the 1st stage and must do so for the laboratory, but the 2nd stage and the outer shield. The temperature fluctuation of the 2nd stage is transferred to the cavity through a middle shield. The temperature fluctuation of an outer shield is also transferred to the cavity via a middle shield.

Considering the heat transfer through solid materials, any temperature fluctuation at high frequency diminishes during the heat transfer according to the thermal resistance and the heat capacity. The transfer function of the temperature fluctuation in such a situation can be described as

$$H^{\mathrm{HT}}_{\mathrm{X}\to\mathrm{Y}}(f) = \frac{1}{1 + \mathrm{i}f R_{\mathrm{X,Y}} C_{\mathrm{Y}}}, \tag{3.13}$$

where the subscript $X \to Y$ means the situation where temperature fluctuation of X travels to Y. $R_{\mathrm{X,Y}}$ and C_{Y} are the thermal resistance between X and Y, and the heat capacity of Y, respectively.

On the other hand, considering the heat transfer from radiation, the heat flux between two materials, X and Y, can be described as

$$Q_{\mathrm{X}\to\mathrm{Y}} = \varepsilon^{\mathrm{eff}}_{\mathrm{X,Y}} \sigma_{\mathrm{B}} \left(A_{\mathrm{X}} T^4_{\mathrm{X}} - A_{\mathrm{Y}} T^4_{\mathrm{Y}} \right), \tag{3.14}$$

where

$$\varepsilon^{\mathrm{eff}}_{\mathrm{X,Y}} = \frac{\varepsilon_{\mathrm{X}} \varepsilon_{\mathrm{Y}}}{\varepsilon_{\mathrm{X}} + \varepsilon_{\mathrm{Y}} - \varepsilon_{\mathrm{X}} \varepsilon_{\mathrm{Y}}} \tag{3.15}$$

is the effective emissivity between X and Y. A_X and T_X are the surface area and the temperature of X. Then, the fluctuation of the heat flux can be written as

$$\delta Q_{\mathrm{X}\to\mathrm{Y}} = 4\varepsilon^{\mathrm{eff}}_{\mathrm{X,Y}} \sigma_{\mathrm{B}} \left(A_{\mathrm{X}} T^3_X \delta T_{\mathrm{X}} - A_{\mathrm{Y}} T^3_{\mathrm{Y}} \delta T_{\mathrm{Y}} \right). \tag{3.16}$$

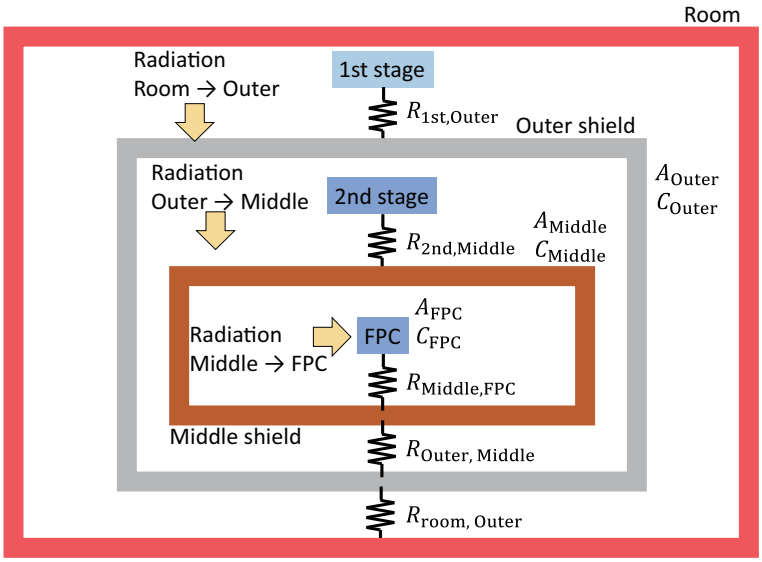

Figure 3.11: The designed thermal structure of our experiment.

We can therefore describe the temperature fluctuation of Y as

$$\delta T_{\mathrm{Y}} = \int \frac{\delta Q_{\mathrm{X}\to\mathrm{Y}}}{C_{\mathrm{Y}}}\, dt = \frac{4\varepsilon^{\mathrm{eff}}_{\mathrm{X,Y}}\sigma_{\mathrm{B}}}{C_{\mathrm{Y}}}\left(A_{\mathrm{X}}T_X^3\int \delta T_{\mathrm{X}}\, dt - A_{\mathrm{Y}}T_{\mathrm{Y}}^3\int \delta T_{\mathrm{Y}}\, dt\right). \tag{3.17}$$

Now, considering Eq. (3.17) in the frequency domain, it can be rewritten as

$$\delta\tilde{T}_{\mathrm{Y}} = \frac{4\varepsilon^{\mathrm{eff}}_{\mathrm{X,Y}}\sigma_{\mathrm{B}}}{\mathrm{i}\omega C_{\mathrm{Y}}}\left(A_{\mathrm{X}}T_X^3\delta\tilde{T}_{\mathrm{X}} - A_{\mathrm{Y}}T_{\mathrm{Y}}^3\delta\tilde{T}_{\mathrm{Y}}\right). \tag{3.18}$$

The transfer function of the temperature fluctuation from radiation is thus expressed as

$$H^{\mathrm{RT}}_{\mathrm{X}\to\mathrm{Y}}(f) = \frac{\delta\tilde{T}_{\mathrm{Y}}}{\delta\tilde{T}_{\mathrm{X}}} = \frac{A_{\mathrm{X}}T_{\mathrm{X}}^3}{A_{\mathrm{Y}}T_{\mathrm{Y}}^3}\frac{1}{1+\mathrm{i}fC_{\mathrm{Y}}\frac{\pi}{2\varepsilon^{\mathrm{eff}}_{\mathrm{X,Y}}\sigma_{\mathrm{B}}A_{\mathrm{Y}}T_{\mathrm{Y}}^3}}. \tag{3.19}$$

Now, assuming that the temperature fluctuation spectra of the 2nd stage of the refrigerator and the outer radiation shield to be

$$\sqrt{G_T(f)} = \frac{1.0\times10^{-4}}{f}\ \mathrm{K}/\sqrt{\mathrm{Hz}}, \tag{3.20}$$

the noise level of the temperature-fluctuation noise can be written as

$$\frac{\delta\nu}{\nu} = \alpha\sqrt{G_T(f)}\left(H^{\mathrm{HT}}_{\mathrm{Middle}\to\mathrm{FPC}} + H^{\mathrm{RT}}_{\mathrm{Middle}\to\mathrm{FPC}}\right)\times \sqrt{\left(H^{\mathrm{HT}}_{\mathrm{2nd}\to\mathrm{Middle}}\right)^2 + \left(H^{\mathrm{HT}}_{\mathrm{Outer}\to\mathrm{Middle}} + H^{\mathrm{RT}}_{\mathrm{Outer}\to\mathrm{Middle}}\right)^2}\ [/\sqrt{\mathrm{Hz}}]. \tag{3.21}$$

Table 3.4 gives the parameters of our experiment for calculating the temperature-fluctuation noise.

temperature	$T_{\mathrm{Outer}} = 100$ K
	$T_{\mathrm{Middle}} = T_{\mathrm{FPC}} = 18$ K
temperature fluctuation	$\sqrt{G_{\mathrm{T}}(f)} = 1.0\times10^{-4}/f$ K/$\sqrt{\mathrm{Hz}}$
thermal resistance	$R_{\mathrm{2nd,Middle}} = 70$ K/W
	$R_{\mathrm{Middle,FPC}} = R_{\mathrm{Outer,Middle}} = 10^3$ K/W
heat capacity	$C_{\mathrm{Middle}} = 130$ J/K
	$C_{\mathrm{FPC}} = 120$ J/K
surface area	$A_{\mathrm{Outer}} = 0.75$ m^2
	$A_{\mathrm{Middle}} = 0.63$ m^2
	$A_{\mathrm{FPC}} = 0.51$ m^2
emissivity	$\varepsilon_{\mathrm{Outer}} = \varepsilon_{\mathrm{FPC}} = 0.1$ [41]
	$\varepsilon_{\mathrm{Middle}} = 0.04$ [41]
cavity CTE	$\alpha = 1.0\times10^{-9}$ /K

Table 3.4: Parameters for calculating the temperature-fluctuation noise

3.2.5 Residual amplitude modulation noise

The noise level of the RAM noise can be described as Eq. (2.83). Therefore, by using the parameters given in Table 3.5, it can be calculated as

$$\frac{\delta\nu}{\nu} = 1.3 \times 10^{-17} \ /\sqrt{\text{Hz}}. \tag{3.22}$$

modulation depth	$m = 0.27$ rad
amplitude-modulation index fluctuation	$\sqrt{G_{m_\text{a}}(f)} = 1.1 \ \times 10^{-5} \ /\sqrt{\text{Hz}}$
phase difference	$\phi = 0$ rad
cavity finesse	$\mathcal{F} = 1.0 \times 10^5$
cavity FSR	$\nu_\text{FSR} = 7.5 \times 10^8$ Hz
laser frequency	$\nu = 2.14 \times 10^{14}$ Hz

Table 3.5: Parameters for calculating the RAM noise.

3.2.6 Residual gas noise

The effect of the residual gas depends on the temperature, pressure, beam size, kind of residual gas, etc. Using Eq. (2.86) and the parameters in Table 3.6, the noise spectrum of the residual gas noise can be calculated as

$$\frac{\delta\nu}{\nu} = 1.0 \times 10^{-19} \ /\sqrt{\text{Hz}}. \tag{3.23}$$

pressure	$p = 1 \times 10^{-4}$ Pa
temperature	$T = 18$ K
beam size	$w = 4.5 \times 10^{-4}$ m
cavity length	$L = 0.2$ m
refractive index	$n_0 = 1 + 2.52 \times 10^{-4}$

Table 3.6: Parameters for calculating the residual gas noise. We assume the kind of residual gas to be water.

3.2.7 Doppler noise

The laser light acquires frequency noise, like Eq. (2.91), while traveling. However, when Doppler noise cancellation is applied, the effect from the fluctuation of the traveling path will be negligible, and the effect from the length fluctuation of a short arm of a DAMI will be significant [35].

Figure 3.12 is a conceptual image of the Doppler noise cancellation. The amplitude of a laser beam after M1 can be written as

$$E_{\mathrm{AM1}} = t_{\mathrm{BS}} t_{\mathrm{M1}} E \mathrm{e}^{\mathrm{i}\left((\Omega+\Omega_{\mathrm{A}})t - \frac{\Omega(L_1+L_2)+\Omega_{\mathrm{A}}L_2}{c}\right)}, \tag{3.24}$$

where t_{BS}, t_{M1} are the transmittances of a BS and an M1 mirror, respectively. Ω_{A} is the shift frequency of an AOM.

The amplitude of the light reflected at an M1 mirror and coming back to the BS can be written as

$$E_{\mathrm{RM1}} = t_{\mathrm{BS}} r_{\mathrm{M1}} E \mathrm{e}^{\mathrm{i}\left((\Omega+2\Omega_{\mathrm{A}})t - \frac{2(\Omega+\Omega_{\mathrm{A}})(L_1+L_2)}{c}\right)}, \tag{3.25}$$

where r_{M1} is the amplitude reflectance of the M1 mirror. In the same way, we can describe the amplitude of the light reflected at the M2 mirror as being

$$E_{\mathrm{RM2}} = r_{\mathrm{BS}} r_{\mathrm{M2}} E \mathrm{e}^{\mathrm{i}\left(\Omega t - \frac{2\Omega L_3}{c}\right)}, \tag{3.26}$$

where r_{M2} is the amplitude reflectance of the M2 mirror. Then, the laser power at a PD can be described as

$$\begin{aligned} \frac{P_{\mathrm{r}}}{t_{\mathrm{BS}}^2 r_{\mathrm{BS}}^2 P_{\mathrm{in}}} &= \left| r_{\mathrm{M1}} \mathrm{e}^{\mathrm{i}\left((\Omega+2\Omega_{\mathrm{A}})t - \frac{2(\Omega+\Omega_{\mathrm{A}})(L_1+L_2)}{c}\right)} - r_{\mathrm{M2}} \mathrm{e}^{\mathrm{i}\left(\Omega t - \frac{2\Omega L_3}{c}\right)} \right|^2 \\ &= r_{\mathrm{M1}}^2 + r_{\mathrm{M2}}^2 + 2\cos\left\{ 2\Omega_{\mathrm{A}} t - \frac{\Omega(L_1+L_2-L_3)+\Omega_{\mathrm{A}}(L_1+L_2)}{c} \right\}. \end{aligned} \tag{3.27}$$

Now, by demodulating this signal by $\cos(2\omega_{\mathrm{A}} t)$, where ω_{A} is an invariable

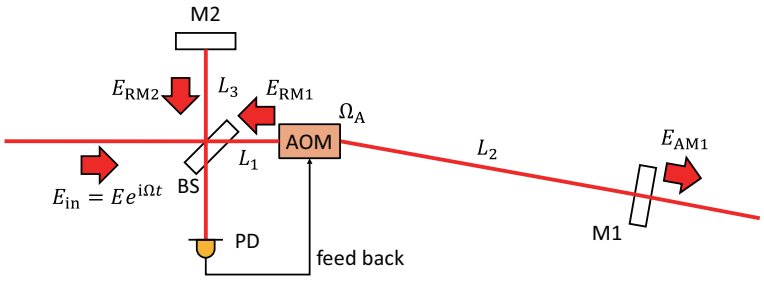

Figure 3.12: Conceptual image of the Doppler noise cancellation. Using this scheme, we can transfer laser light with a very small phase modulation.

angular frequency as large as Ω_A, we can obtain the error signal ϵ_{DNC} as

$$\frac{\epsilon_{DNC}}{t_{BS}^2 r_{BS}^2 P_{in}} = \frac{1}{2}\cos 2\left[(\Omega_A - \omega_A)\,t - \frac{\Omega(L_1+L_2-L_3)+\Omega_A(L_1+L_2)}{c}\right]. \tag{3.28}$$

Then, by feeding back the signal to the shift frequency of the AOM to keep $\epsilon_{DNC} = 0$, the equation

$$(\Omega_A - \omega_A)\,t - \frac{\Omega(L_1+L_2-L_3)+\Omega_A(L_1+L_2)}{c} = \frac{\pi}{4}(2n+1) \tag{3.29}$$

is obtained. Therefore, Eq. (3.24) can be rewritten as

$$E_{AM1} = t_{BS}t_{M1}E\mathrm{e}^{\mathrm{i}\left((\Omega+\omega_A)t - \frac{-\Omega L_3+\Omega_A L_1}{c}+\frac{\pi}{4}(2n+1)\right)}. \tag{3.30}$$

Then, the frequency fluctuation in the frequency domain can be written as

$$\delta\tilde{\Omega} = \frac{\mathrm{i}\omega}{c}\left(\Omega\tilde{L_3} - \Omega_A\tilde{L_1} - L_1\tilde{\Omega_A}\right). \tag{3.31}$$

Here, considering the situation $L_1 \ll L_3$ and $\Omega \gg \Omega_A$, Eq. (3.31) can be approximated as

$$\delta\tilde{\Omega} = \frac{\mathrm{i}\omega\Omega}{c}\tilde{L_3}. \tag{3.32}$$

Then, the frequency fluctuation of the Doppler noise depends only on the length fluctuation of the short arm of the DAMI.

There are many kinds of noise sources of the Doppler noise, such as seismic

vibration, temperature fluctuation, and wind. Therefore, the noise level of the Doppler noise cannot be estimated easily in general. However, using the DAMI, which has a reliable wind shield and sound isolation, 10^{-17} level, the frequency transfer is reported using a 30 km long optical fiber [42]. The fibers used in our experiment are much shorter than 30 km: about 5 m. The Doppler noise therefore is not problematic for reaching the 10^{-17} level of stability if we use the Doppler noise canceling system in our setup.

3.2.8 Design performance

The total noise budget of this experiment is shown in Fig. 3.13. The designed noise budget of our experiment is limited by the coating thermal noise, acceleration noise, and RAM noise of around 1 Hz.

The laser frequency stability is often evaluated by the Allan deviation (see Appendix B). This deviation and the power spectrum are connected by the following equation:

$$\sigma_y(\tau) = \sqrt{2\int_0^\infty G_y(f)\frac{\sin^4(\pi\tau f)}{(\pi\tau f)^2}\,df}, \tag{3.33}$$

where τ is an averaging time. $G_y(f)$ is a PSD of the physical quantity y. This equation means that the Allan deviation at τ is dominantly determined by the power spectrum near $f = 1/2\tau$. Using this equation, the Allan deviation of our experiment at around 1 second which is an important time scale for applying a frequency-stabilized laser to an optical lattice clock can be estimated as in Fig. 3.14. So, we can achieve a 10^{-17} level of stability by using this design.

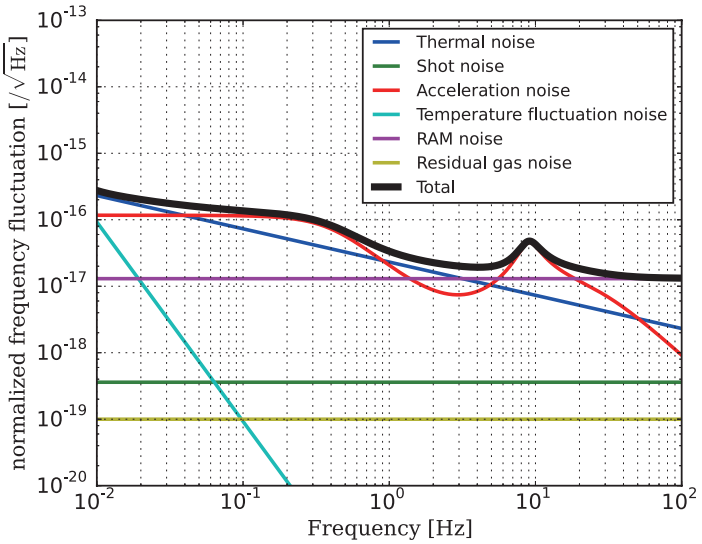

Figure 3.13: Total noise budget of our experiment. The noise sources limiting the frequency stability in our experimental design are the coating thermal noise, acceleration noise, and RAM noise.

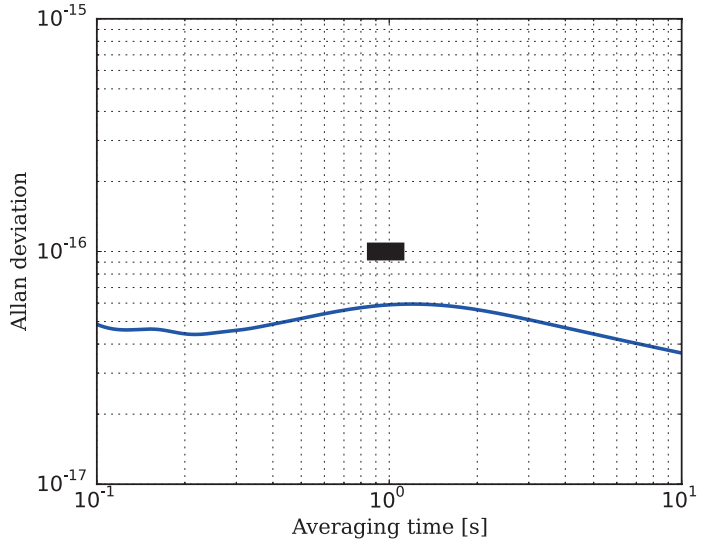

Figure 3.14: Designed stability of our experiment (blue curve). The stability of our design can reach the 10^{-17} level of stability at 1 second (below the black rectangle).

3.3 Summary of this chapter

- We use a monocrystalline silicon optical cavity, and cool it down at 18 K for reducing the thermal noise.
- In our experiment, both passive and active vibration isolation systems are used. PVIS reduces the acceleration noise at high frequency and AVIS decreases at low frequency.
- The thermal insulation stacks and radiation shields are very important structures for cooling a reference cavity at 18 K.
- The Doppler noise cancellation is a strong method for reducing the phase fluctuation, which the laser beam obtains during traveling the optical path.
- The designed noise budget of our experiment is limited by the coating thermal noise, acceleration noise, and RAM noise at around 1 Hz.
- We have designed a laser frequency stabilization system that can reach the 10^{-17} level.

Chapter 4
Performance Evaluation

In this chapter, we show the performance of our experimental setup.

4.1 Silicon optical cavity

In this section, we consider the optical property of the FPC in our experiment.

According to the inspection sheet of our mirrors, the power transmittance is

$$T = t_{\mathrm{F}}^2 = t_{\mathrm{E}}^2 = 1.05 \times 10^{-5}. \tag{4.1}$$

Then, the amplitude transmittance of the front and end mirrors can be calculated as

$$t_{\mathrm{F}} = t_{\mathrm{E}} = \sqrt{T} = 3.24 \times 10^{-3}. \tag{4.2}$$

The reflectance of a mirror is related to the finesse of a FPC. So, it can be estimated by measuring the finesse of an optical cavity. Using Eq. (2.11) and Eq. (2.21), the finesse of a cavity can be estimated as

$$\mathcal{F} = 2\pi\tau_{\mathrm{FPC}}\nu_{\mathrm{FSR}}. \tag{4.3}$$

Here, ν_{FSR} in our experiment is

$$\nu_{\mathrm{FSR}} = \frac{c}{2L} = (7.49 \pm 0.01) \times 10^8 \text{ Hz}. \tag{4.4}$$

The error is the systematic error of the length of our cavity. Thus, the finesse can be calculated by measuring the time constant, τ_{FPC}, of a FPC.

A schematic of the experimental setup for measuring the time constant of our optical cavity is shown in Fig. 4.1. The time constant of the FPC is

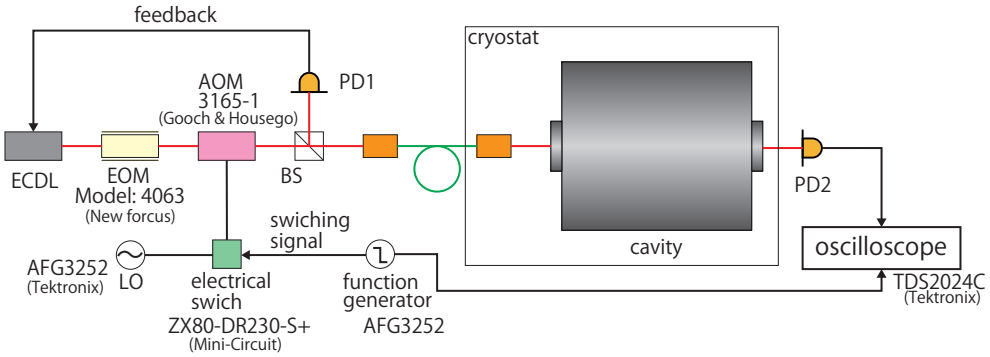

Figure 4.1: Schematic of the setup for measuring the time constant of our optical cavity. The PD2 used in this measurement is not the InGaAs photo diode G12181-020A but the InGaAs photo diode G12180-003A because the response of the PD should be fast enough to measure the decay time of the transmitted light. We use the trans-impedance circuit for changing the photo-current to the voltage. Details of the circuit is shown in Appendix C. Several model numbers of the equipments used for this measurement are shown in the figure.

determined by measuring the time dependence of the transmitted light power when the input light is stopped. At first, we stabilize the laser frequency to the resonant frequency of the FPC. Then, a certain amount of transmitted light enters the PD2. When the RF power is switched off, the laser light entering the FPC stops, and the power of the transmitted light gradually decreases. The switching signal from the function generator and the output signal of the PD2 are saved using the data-storing function of the digital oscilloscope.

The wavelength of the laser is about 1397 nm, and the temperature of the cavity is about 10 K during the measurement. The transmitted power at the time $t = 0$ is about 15 μW. The sampling frequency and the resolution of the oscilloscope are 10 MHz and 2 mV, respectively. The switching speed of the electrical switch in this experiment is below 1 μs. Therefore, the decay time of the transmitted power is determined by the time constant of the cavity when the time constant of our cavity is much longer than 1 μs.

Figure 4.2 shows an example of the time dependence of the transmitted

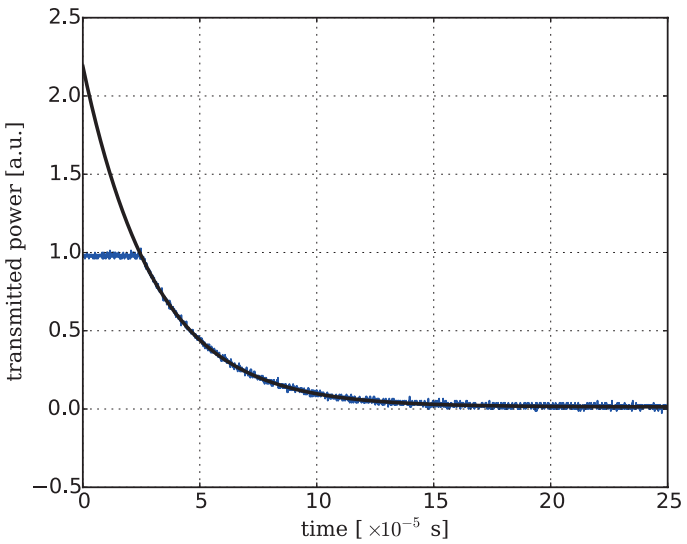

Figure 4.2: Example of the time dependence of the transmitted light reduction. The blue line is the measured transmitted power and the black line is a fitting curve with Eq. (4.5) using the transmitted power at over $t = 25$ μs.

power. By fitting this reduction curve with the following equation

$$P = A\mathrm{e}^{-t/\tau_{\mathrm{FPC}}} + C, \tag{4.5}$$

the time constant of our FPC can be estimated. In our experiment, the time constant is measured as

$$\tau_{\mathrm{FPC}} = (3.07 \pm 0.01) \times 10^{-5} \text{ s}. \tag{4.6}$$

The error is dominantly determined by the fitting error of the measurement. Then, the finesse of our optical cavity is determined to be

$$\mathcal{F} = (1.445 \pm 0.006) \times 10^{5}. \tag{4.7}$$

Moreover, by using Eq. (2.21), FWHM can be calculated as

$$\nu_{\mathrm{FWHM}} = (5.19 \pm 0.02) \times 10^{3} \text{ Hz}. \tag{4.8}$$

Assuming that the amplitude reflectance of the front mirror and the end mirror are the same, the amplitude reflectance of the mirrors of our FPC can be estimated as

$$r_{\mathrm{F}} = r_{\mathrm{E}} = 0.99998913 \pm 0.00000004. \tag{4.9}$$

The power transmittance, T, power reflectance, R, and power loss, L, of a mirror are related by an equation, as follows:

$$T + R + L = 1, \tag{4.10}$$

where $R = r_{\mathrm{F}}^2 = r_{\mathrm{E}}^2$ is the power reflectance of a mirror. Then, the amplitude loss of a mirror can be estimated to be

$$l_{\mathrm{F}} = l_{\mathrm{E}} = \sqrt{L} = (3.35 \pm 0.02) \times 10^{-3}. \tag{4.11}$$

4.2 Vibration and its isolation systems

In this section, we discuss the seismic vibration in our laboratory and the performances of the vibration isolation systems.

4.2.1 Seismic vibration level

The ground vibration is a main source of the acceleration noise, which depends on the environment, such as the stiffness of the ground, structure of the building, etc. We should thus check the spectrum of the seismic motion in the experimental environment.

The seismic acceleration can be measured with a vibration sensor. The setup for the acceleration spectrum measurement is shown in Fig. 4.3. We define the X axis as the direction along the optical axis of our cavity. We also define the Y and Z axes as the direction orthogonal to the X axis in the horizontal plane and the vertical direction, respectively. The signal of the vibration sensor is converted into the voltage spectrum by the FFT analyzer. Since the typical transfer function of our vibration sensor (L-22E, 510 Ω, IRIS

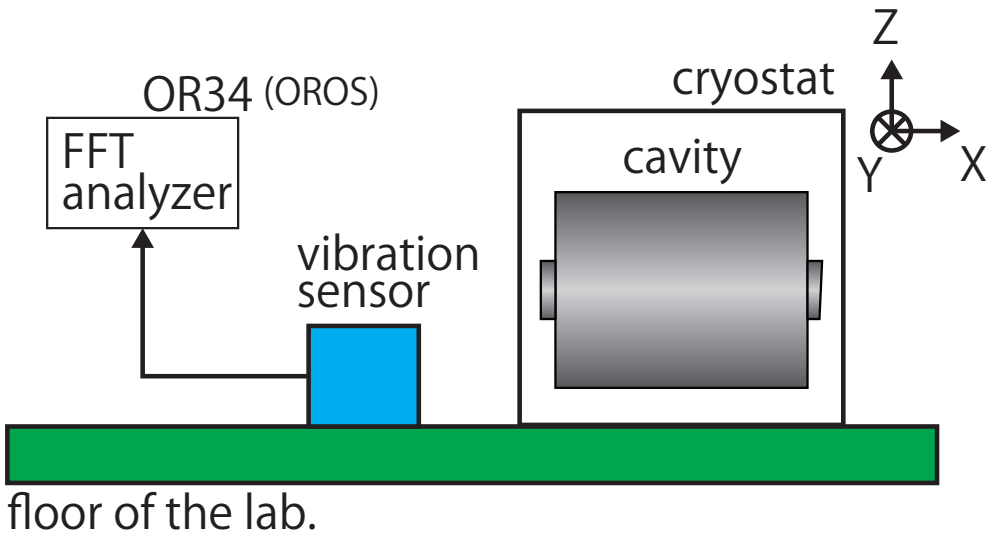

Figure 4.3: Setup for measuring the seismic acceleration spectra.The vibration sensors signal is amplified by an electric amplifier. The details of the circuit are shown in Appendix C. The model number of our FFT analyzer is shown in the figure.

PASSCAL) is given by [43]

$$H(f) \simeq \frac{2\pi f}{47.1}\sqrt{1+\frac{1}{(f/2.0\ \mathrm{Hz})^2}}\ [(\mathrm{m/s^2})/\mathrm{V}], \tag{4.12}$$

we can calculate the acceleration spectrum from the signal of the vibration sensor.

Figure 4.4 shows the seismic acceleration spectra of the translational axes in our laboratory. The distance between the vibration sensor and the cryostat is about 1 m, and the cryogenic refrigerator is moving during this measurement. We use a hamming window function for measuring the voltage spectrum.

In this result, the seismic vibration level of our experimental environment is much larger than that we expected. We should therefore further reduce the vibration levels using passive and active vibration isolation systems, and employ a low-vibration sensitivity support for a reference cavity.

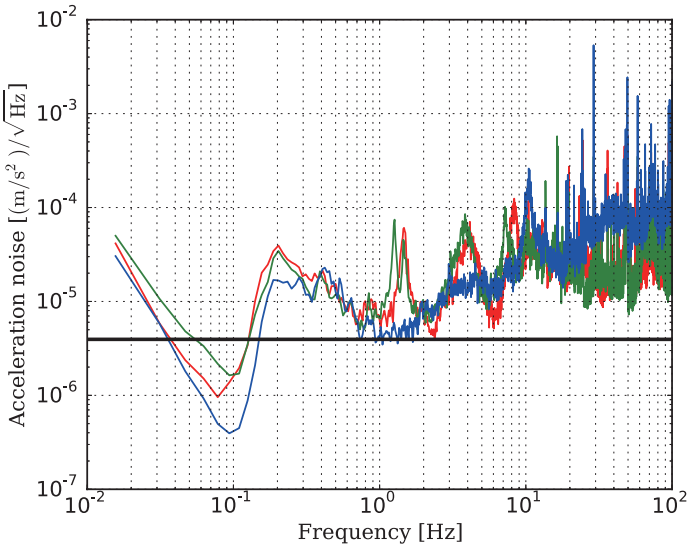

Figure 4.4: Vibration level at our experimental room. The blue, green, red lines correspond to the acceleration along the X, Y, and Z axes. The black line is the acceleration spectrum that we expect from Eq. (3.7). The spectra below ∼0.1 Hz are circuit noise of the amplifier of the vibration sensor. The peak at around 0.2 Hz is the micro seismic noise and that at around 1.4 Hz is from a vibration-reduction structure of the building for earthquakes.

4.2.2 Passive vibration isolation system

The transfer function of the passive vibration isolation can be written as Eq. (3.10). The performance of the system is therefore determined only by a resonant frequency and Q factor.

The setup for checking the performance of the PVIS is shown in Fig. 4.5. If there is no resonance except for the resonance of rubber legs, the signal ratio between the sensors on the AVIT and on the ground is the same as the transfer function of the PVIS. We can use the same method described in Section 4.2.1 for measuring the acceleration spectra at the top plate of the AVIT and the floor. This measurement is also done under the condition that the cryogenic refrigerator is moving.

Figure 4.6 is the result of this measurement. By reading the peak values and the half widths of the peaks, we can estimate the horizontal resonant

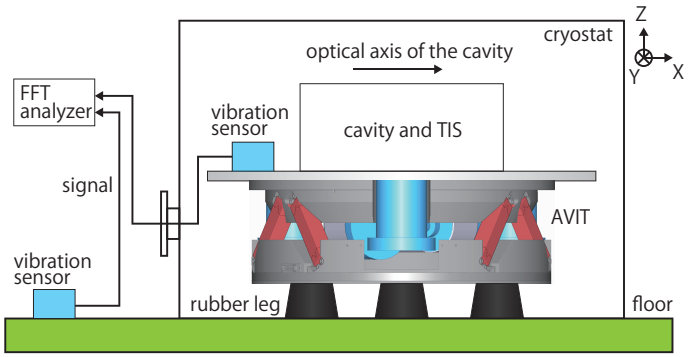

Figure 4.5: Setup for measuring the resonant frequencies of the rubber legs. The vibration sensors are put on the top plate of the AVIT and on the ground. The resonant frequencies depend on the mass on the rubber legs. So, the mass on the AVIT is the real cavity and the thermal insulation stacks (TISs) during this measurement. The vibration spectra are measured using the FFT analyzer.

frequencies and Q values of the PVIS as:

$$f_{\mathrm{P}X} = 8.5 \pm 0.2 \text{ Hz}, \tag{4.13}$$

$$f_{\mathrm{P}Y} = 8.8 \pm 0.2 \text{ Hz}, \tag{4.14}$$

$$Q_X = 2.9 \pm 0.1, \tag{4.15}$$

$$Q_Y = 3.4 \pm 0.1. \tag{4.16}$$

The error is dominantly determined by the frequency resolution of the measurement.

However, the resonant frequency and Q factor along the Z axis cannot be determined by this measurement because there are many resonances of structures inside the cryostat at over 10 Hz. Thus, the performance along the Z axis is estimated by measuring the transfer function from the voltage applied to the AVIT to the vibration of the top plate. Figure 4.7 shows a gain curve of the transfer function. By reading the peak value and half width of the peak, we can get the resonant frequency and Q factor as

$$f_{\mathrm{P}Z} = 21 \pm 2 \text{ Hz}, \tag{4.17}$$

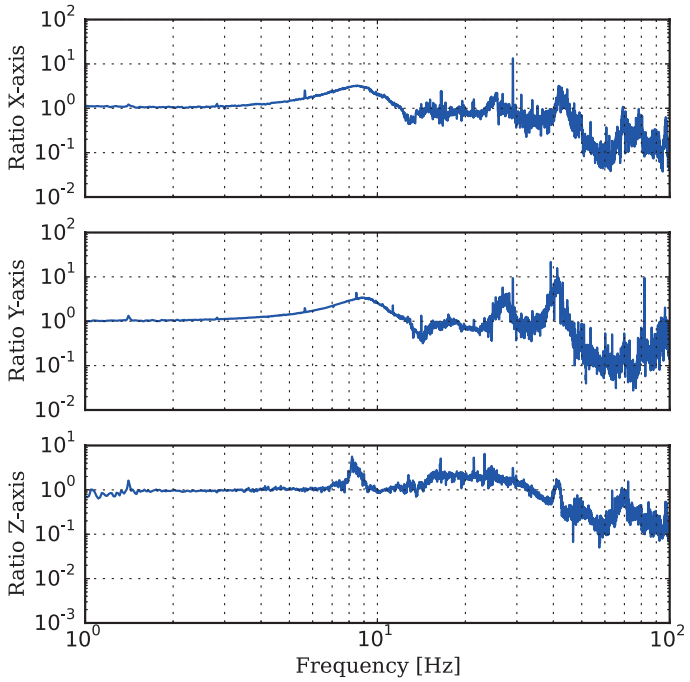

Figure 4.6: Ratio between the seismic motion and the vibration on the AVIT. These ratios represent the vibration isolation ratios of the PVIS along each axis.

$$Q_Z = 1.2 \pm 0.1. \tag{4.18}$$

The error of this result is also determined by the frequency resolution.

In this result, the passive isolation system of the translational axes are almost the same as the design, but that of a vertical axis has a higher resonant frequency, as expected, which means that the vibration isolation performance along the Z axis is worse. The main reason of this result is that the rubber legs are compressed by the mass on them, and thus the hardness of the vertical axis becomes higher than the other translational axes. It will therefore be solved by using a structure whose hardness does not depend on the mass on it, for example a mechanical spring.

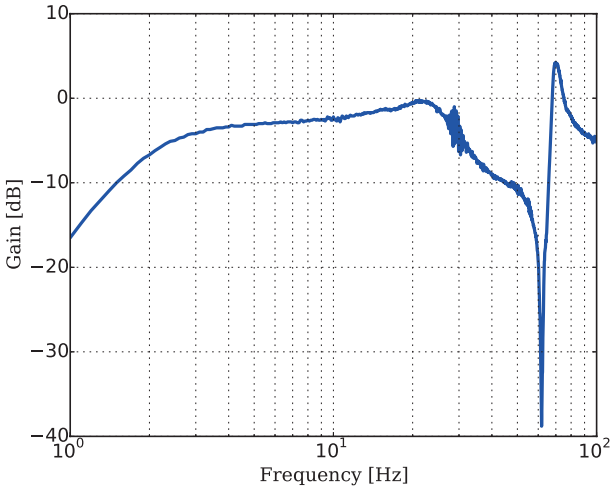

Figure 4.7: Gain curve of the transfer function of the AVIT along the Z axis. The gain curve below at 2 Hz has a slope because of the frequency response of the vibration sensor on the AVIT. The dip and the peak of the gain curve at around 60 Hz and 70 Hz are the anti-resonance and resonance of the AVIT, respectively.

4.2.3 Active vibration isolation

The active vibration isolation using the AVIT is achieved by feeding back the vibration signal at the top plate of the AVIT to the voltage applied to the PZT actuators. Figure 4.8 shows a block diagram of the AVIS.

The vibration signals at the top plate of the AVIT are diagonalized to six degrees of freedom: three translational axes and three rotational axes. In the real feedback system of our experiment, we do not use the signals of rotational axes because the signal of the rotational vibration is too small to be measured by the vibration sensors.

The open-loop transfer functions of the AVIS in our experiment are shown in Fig. 4.9 to Fig. 4.11. In these results, the behaviors of the AVIS are better than the design performance.

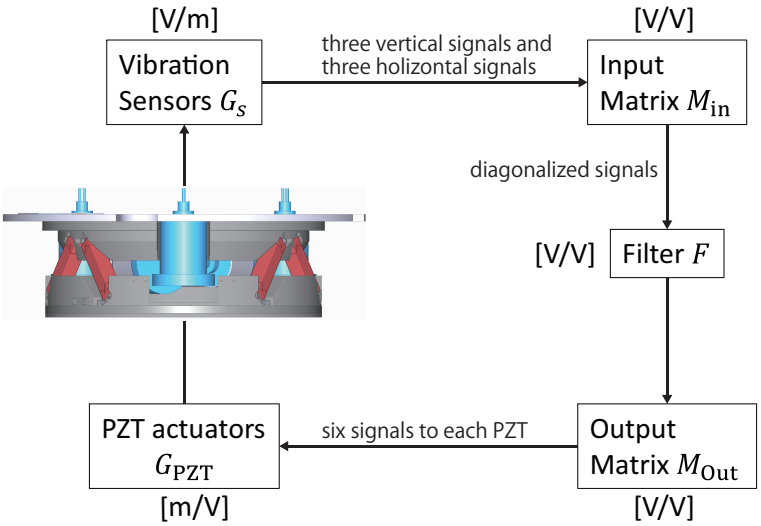

Figure 4.8: Feedback diagram of the AVIS. The signals from vibration sensors are diagonalized by the input matrix of a digital feedback system. These diagonalized signals are independently filtered and changed to the voltage applied to each PZT by the output matrix.

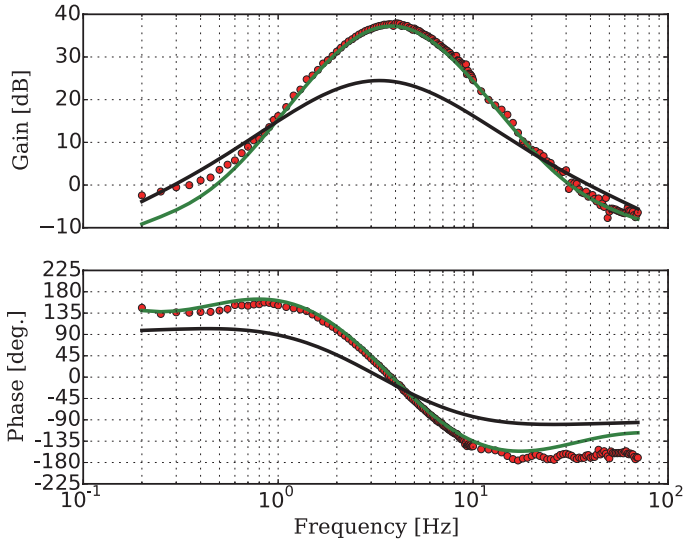

Figure 4.9: Open-loop transfer function of the X axis. The red dots are the measured values and the green line is a theoretical curve of the feedback system. The black line is the designed open-loop transfer function of the AVIS.

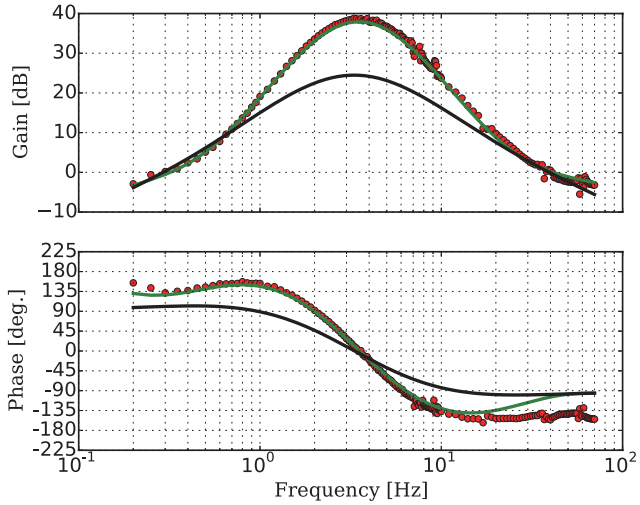

Figure 4.10: Open-loop transfer function of the Y axis. The red dots are the measured values and the green line is a theoretical curve of the feedback system. The black line is the designed open-loop transfer function of the AVIS.

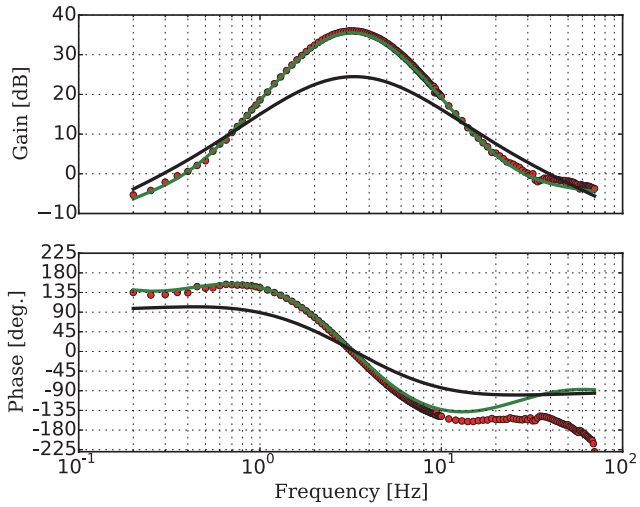

Figure 4.11: Open-loop transfer function of the Z axis. The red dots are the measured values and the green line is a theoretical curve of the feedback system. The black line is the designed open-loop transfer function of the AVIS.

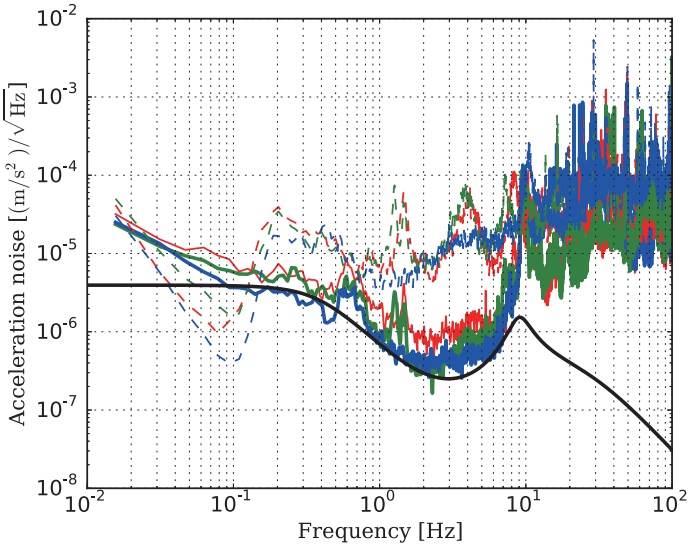

Figure 4.12: Acceleration spectra on the AVIT after controlling it. The blue, green, red lines show vibrations along X, Y, and Z axes, respectively. The solid lines represent the inloop spectra after controlling the AVIT. The dashed lines express free seismic acceleration spectra. The black line shows our designed acceleration spectrum noise level.

Figure 4.12 shows the vibration levels after controlling the AVIT. Then, the acceleration noise at a cavity point does not reach the designed noise level, especially at high frequencies, because the seismic acceleration level is much larger than the acceleration that we expect from Eq. (3.7). We should therefore use a lower resonant-frequency structure for the passive vibration isolation.

4.2.4 Vibration sensitivity

The vibration sensitivity depends on many factors, such as the cavity and support materials, the shape of a reference cavity, support points, etc. So by choosing these elements adequately, the vibration sensitivities along the X, Y, and Z axes can be small at the same time. In this subsection, we discuss the vibration sensitivity of our reference cavity.

Our cavity is supported by four rectangular parallelepiped rubber legs which are placed symmetrically around the center of the cavity. The size

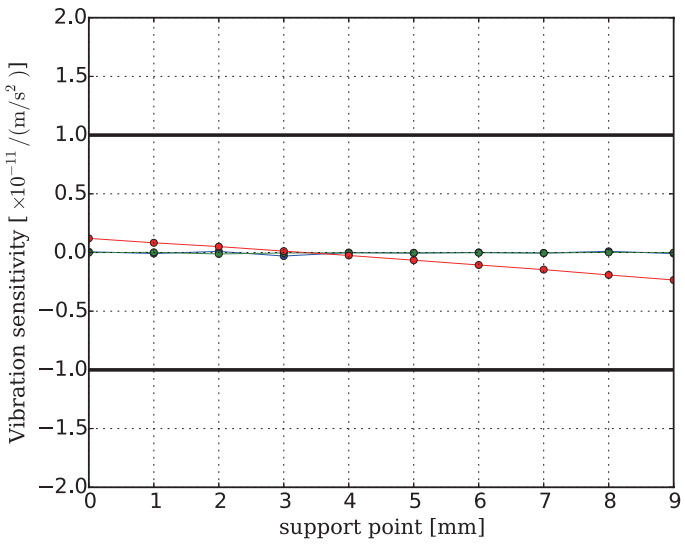

Figure 4.13: Calculation results of the FEM. The blue, green, and red lines show the vibration sensitivity along the X, Y and Z axes, respectively.

of the rubber legs is 5 mm in height and 8 mm on each side.

The vibration sensitivity can be roughly calculated by the finite element method (FEM) [20]. Since the shape of the cavity spacer has already been designed, we calculate the vibration sensitivity for deciding on the best support points of the cavity. Figure 4.13 shows the calculation result of the FEM as a function of the distance between the support point and the plane of mirror surface. In this result, the dependence of the vibration sensitivity on the support points is very small, especially for the horizontal axes. We thus choose support points near to the zero-cross point of the vibration sensitivity along the Z axis: about 4 mm.

We then check that the vibration sensitivities are as small as we calculated. A schematic diagram of the setup for measuring the vibration sensitivity is shown in Fig. 4.14. The vibration sensitivity is measured by the frequency fluctuation during swinging the cavity. The acceleration applied to the optical cavity is measured by the vibration sensor at the top plate of the AVIT. The frequency fluctuation is measured by the beat signal fluctuation between our laser and another stable laser. The frequency fluctuation signal and the

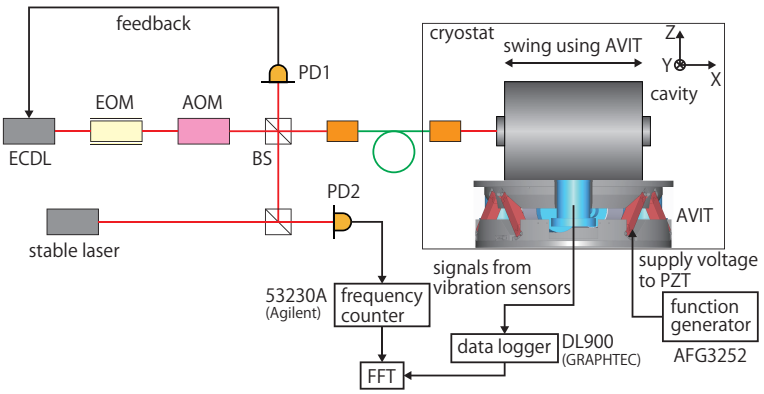

Figure 4.14: Schematic of the setup for measuring the vibration sensitivity. X axis is a direction along the optical axis, and Y axis is an perpendicular to X axis in the horizontal plane. Z axis is the vertical direction. The stable laser is the same one in Fig. 3.8.

acceleration signal are stored by the frequency counter and the data logger, respectively. We calculate the spectra of each signal and take their ratio of them at the swinging frequency. The swinging frequency is 5 Hz, and the acceleration applied to the cavity is about 10^{-3} $(\mathrm{m/s^2})/\sqrt{\mathrm{Hz}}$ at 5 Hz..

In the case that the support point is about 4 mm, the vibration sensitivities of the X, Y, and Z axes are as follows:

$$A_X = (2.5 \pm 0.3) \times 10^{-10} \ /(\mathrm{m/s^2}), \tag{4.19}$$

$$A_Y = (4.6 \pm 0.5) \times 10^{-11} \ /(\mathrm{m/s^2}), \tag{4.20}$$

$$A_Z = (7 \pm 1) \times 10^{-12} \ /(\mathrm{m/s^2}). \tag{4.21}$$

The errors are dominantly determined by the systematic errors of the vibration sensors.

The vibration sensitivity along the Z axis achieves our requirement, below 10^{-11} $/(\mathrm{m/s^2})$, but those of the X and Y axes do not satisfy this requirement. The reason why the horizontal vibration sensitivities are not small may be that there are some asymmetries of the configuration of a reference cavity, such as manufacturing errors of the cavity spacer, the mounting accuracy of the mirrors, etc. However, the vibration sensitivities of our reference cavity is

insensitive to the support point of the optical cavity in the FEM calculation result. Therefore, we should change the shape of our cavity poor to reduce the vibration sensitivity.

4.3 Temperature fluctuation

The temperature fluctuation is small at high frequencies in general because the time constant of heat transfer at room temperature is very long. However, since the pulse tube refrigerator cools the 1st and 2nd stages by compressing and expanding heat exchange gas, the temperature fluctuation spectrum of the refrigerator has some peaks at the cycle frequency. Moreover, the time constant of the heat transfer becomes short at low temperature because the heat capacity of the materials becomes small. Furthermore, since an optical cavity gets heat from an input laser, the laser power fluctuation causes a temperature fluctuation.

4.3.1 2nd stage of the refrigerator

One of the temperature-fluctuation sources of this experiment is the 2nd stage of the refrigerator. The temperature of the 2nd stage of our refrigerator becomes more stable at low temperature than at high temperature because the liquid helium plays the role of a heat bath. We therefore check the temperature fluctuation of the 2nd stage when it operates at below 4 K, which is a temperature well below the value to change helium gas to liquid helium. Figure 4.15 shows the temperature-fluctuation spectrum of the 2nd cold head.

The floor level of this result is dominantly determined by the circuit noise for measuring the temperature. The actual temperature fluctuation of the 2nd stage is therefore below this floor line. The peak structure does not exist in the circuit noise spectrum. So, the sharp peak values of this measurement reflect the actual temperature fluctuation of the 2nd stage caused by the action of the compressor; it is much higher than that which we assumed in Eq. (3.20).

However, the thermal-isolation design of our experiment has a large margin, for example 10^5 at 1 Hz. So, these peaks are not problematic for reaching the 10^{-17} level stability.

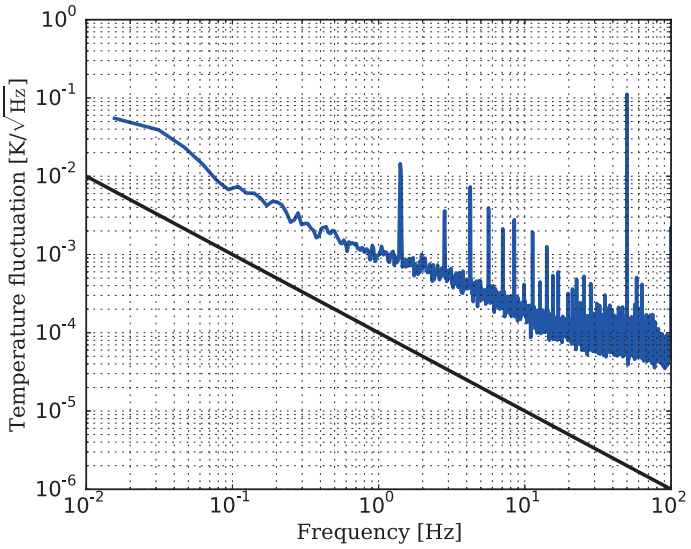

Figure 4.15: Temperature-fluctuation spectrum of the 2nd stage of the refrigerator. The blue lines are the measured values and the black line is a temperature-fluctuation spectrum that we assumed in our design. The temperature during the measurement is about 3.6 K.

4.3.2 Outer shield

Other temperature fluctuation sources of this experiment are the temperature fluctuations of the 1st stage of the refrigerator and the room temperature. However, these temperature fluctuations do not transfer to a reference cavity directly, because there is an outer shield next to the middle shield. Then, it is sufficient to check the temperature fluctuation of the outer shield. The temperature-fluctuation spectrum of the outer shield is shown in Fig. 4.16.

The floor level of this measurement is limited by the circuit noise for measuring the temperature. This result is also larger than the temperature spectrum that we assumed in the experimental design. However, since the margin of the temperature-fluctuation noise is much larger than the difference between the measured temperature fluctuation and that which we expected, it is not a problem.

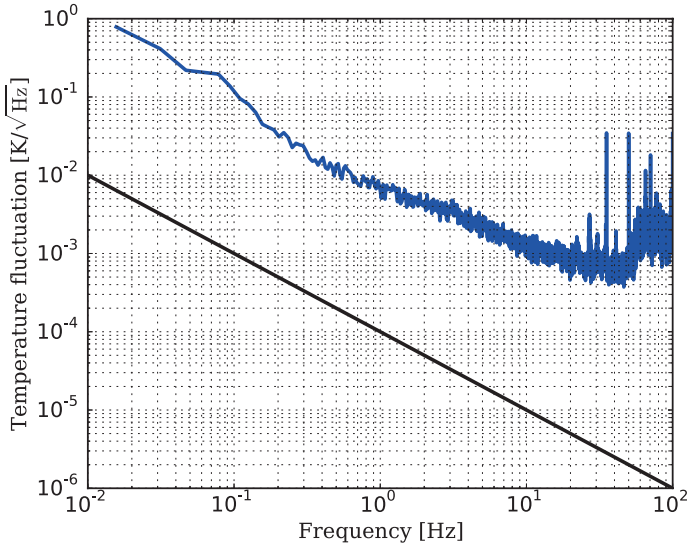

Figure 4.16: Temperature-fluctuation spectrum of the outer radiation shield. The blue lines are the measured values, and the black line is the temperature-fluctuation spectrum that we assumed in our design. The temperature during the measurement is about 100 K.

4.3.3 Laser power effect

The input laser power fluctuation causes a temperature fluctuation locally, which leads to a cavity length fluctuation through thermal expansion. In this subsection, we discuss this effect.

The normalized frequency fluctuation of the laser power change can be described as

$$\frac{\delta\nu}{\nu} = \beta\sqrt{G_P(f)}\ [/\sqrt{\mathrm{Hz}}], \tag{4.22}$$

where β is a coupling index and $G_P(f)$ is the PSD of the transmitted laser power fluctuation.

The coupling index, β, is determined by measuring the frequency fluctuation when the transmitted power is modulated. Figure 4.17 shows the setup for measuring the coupling index, β. We stabilize the laser to the cavity and supply the amplitude modulated RF signal to the AOM. Then, the transmitted light power and the laser frequency are modulated. The power of the trans-

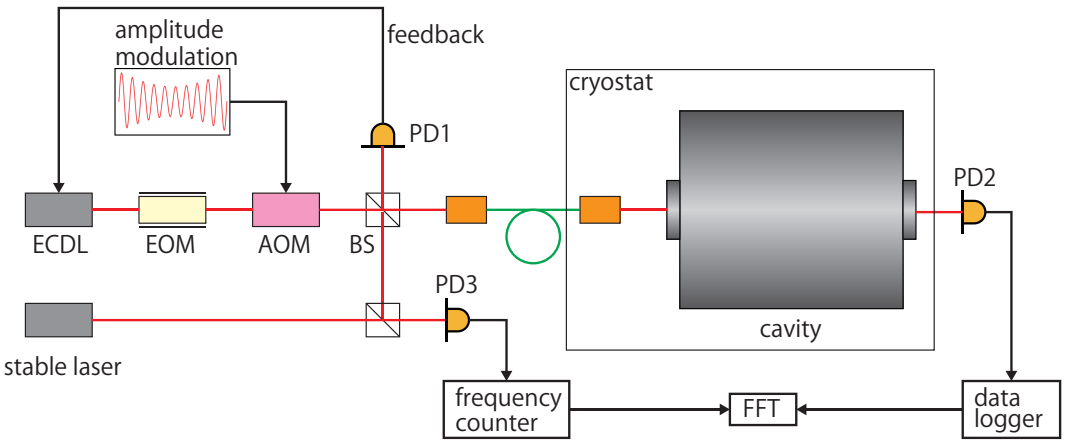

Figure 4.17: Setup for measuring the laser power-fluctuation effect. The PD1 is the InGaAs photo diode G12180-003A, and the PD2 is the InGaAs photo diode G12180-250A. The stable laser is the same one as in Fig. 3.8

mitted light is measured using PD2 and the data logger. The laser frequency is determined by measuring the beat frequency signal between our laser and the stable laser in Fig. 4.17 using the frequency counter. The data of the transmitted power and the laser frequency is converted to the spectra, and we take the ratio between them to determine the coupling index, β.

The wavelength of the ECDL is about 1397 nm, and the temperature of our cavity is about 10 K during the measurement. The amplitude of the RF signal is about 36 dBm, and the modulation depth is 10% of it. The modulation frequency is varied between 0.1 Hz to 10 Hz.

The result of this measurement is shown in Fig. 4.18. In this result, we can regard β as being a constant. The value is estimated as

$$\beta = (1.6 \pm 0.2) \times 10^{-7} \ /\mathrm{W}. \tag{4.23}$$

The error is the standard deviation of this measurement.

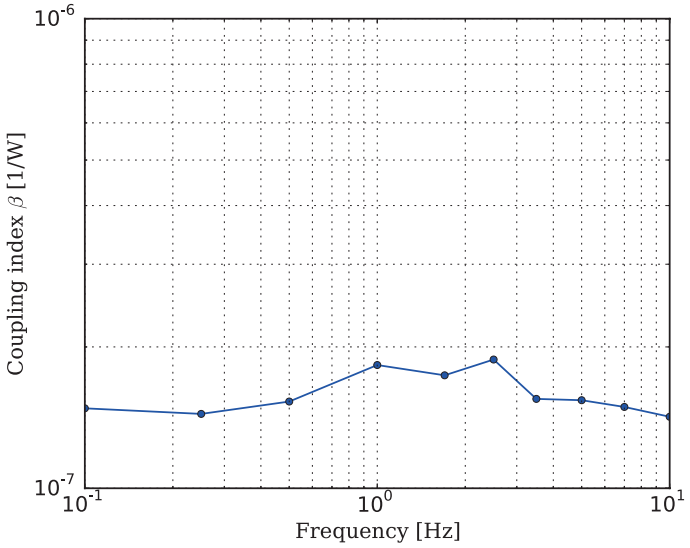

Figure 4.18: Coupling index, β, of our reference cavity. The blue dots are the measured values, which are connected by the blue line.

4.4 Feedback system

We describe the frequency-stabilization feedback system in this section.

The laser source of our experiment is an ECDL. The frequency of an ECDL can be stabilized by controlling the angle of a diffraction grating, and the amperage of a laser diode (LD) current. Thus, the frequency fluctuation at low frequencies is fed back to an angle of the grating, and high-frequency fluctuation is used to control the laser diode current. Figure 4.19 shows a block diagram of our feedback system. A detailed circuit is shown in Appendix C.

The open-loop transfer function of this feedback system can be described as

$$G = -G_{\mathrm{PDH}} G_{\mathrm{PA}} G_1 \left(F_{\mathrm{PZT}} A_{\mathrm{PZT}} + F_{\mathrm{C}} A_{\mathrm{C}} \right). \tag{4.24}$$

Since the transfer functions (G_1, G_2, G_{PA}, F_{PZT}, and F_{C}) can be calculated by the components of the feedback circuit, it is sufficient to measure only G_{PDH}, A_{PZT}, and A_{C}.

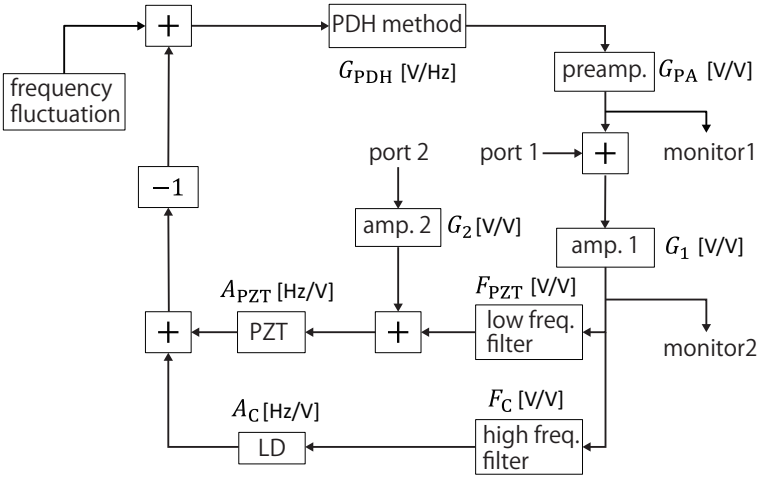

Figure 4.19: Block diagram of our feedback loop for the frequency stabilization. G_{PDH} is the gain of the PDH method; G_{PA} is the transfer function of the preamplifier. F_{PZT} and F_{C} are the transfer functions of the low frequency and high frequency filters, respectively. A_{PZT} and A_{C} are actuator gains of PZT and LD, respectively. G_1 and G_2 are the gains of amplifier1 and amplifier2, respectively.

The actuator gain of the PZT has some resonance, so it is difficult to measure A_{PZT} over the resonant frequency. However, below the resonant frequency, A_{PZT} is a flat response function, which is easy to measure. By applying the voltage from port2 and measuring the frequency shift of the ECDL, we can obtain the actuator gain A_{PZT} as

$$A_{\mathrm{PZT}} = (3.0 \pm 0.1) \times 10^9 \text{ Hz/V (below 100 Hz)}. \tag{4.25}$$

The PDH gain, G_{PDH}, and the actuator gain, A_{C}, can be evaluated by measuring the transfer function between some signal ports during frequency stabilization. The transfer function is measured by the frequency response analyzer FRA5087 (NF's product).

When we supply a modulated voltage to port2, the transfer function from the input voltage at port2 to the output voltage from monitor1 can be written

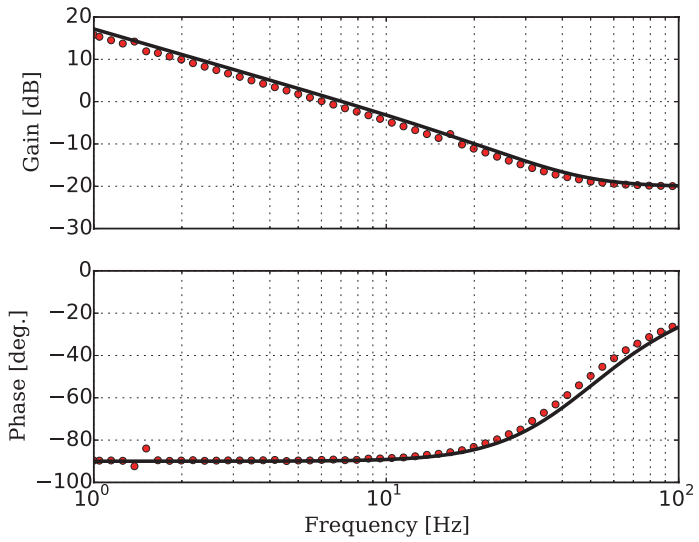

Figure 4.20: Gain and phase of $H_{\mathrm{p2}}^{\mathrm{G1}}$. The red dots are the measured values and the black curve is a theoretical line, assuming $A_{\mathrm{C}} = 10^9$ Hz/V.

as

$$H_{\mathrm{p2}}^{\mathrm{G1}} \simeq \frac{F_{\mathrm{PZT}}}{G_2}\left(1 + \frac{F_{\mathrm{C}}A_{\mathrm{C}}}{F_{\mathrm{PZT}}A_{\mathrm{PZT}}}\right). \tag{4.26}$$

Here, we assume the open-loop gain to be $G \gg 1$. Figure 4.20 shows the measured transfer function and a theoretical curve calculated by Eq. (4.26). In this result, we can estimate the transfer function from the voltage to the frequency through the LD current as

$$A_{\mathrm{C}} = (1.0 \pm 0.1) \times 10^9 \text{ Hz/V}. \tag{4.27}$$

When we supply a modulated voltage from port1, the transfer function from the output voltage from the monitor1 to that from the monitor2 can be written as

$$H_{\mathrm{G_1}}^{\mathrm{G_{PA}}} = \frac{G}{G_1} = G_{\mathrm{PDH}}G_{\mathrm{PA}}\left(F_{\mathrm{PZT}}A_{\mathrm{PZT}} + F_{\mathrm{C}}A_{\mathrm{C}}\right). \tag{4.28}$$

Figure 4.21 shows the measured transfer function and theoretical curve calculated by Eq. (4.28). In this result, we can estimate the gain of the PDH

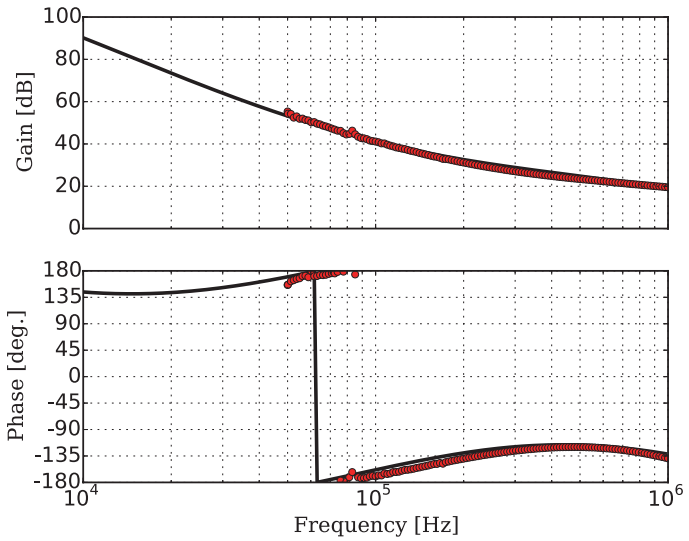

Figure 4.21: Gain and phase of $H_{G_1}^{G_{PA}}$. The red dots are the measured values and the black curve is a theoretical line assuming $A_C = 10^9$ Hz/V and $G_{PDH} = 4.4 \times 10^{-6}$ V/Hz.

method as

$$G_{PDH} = (4.4 \pm 0.4) \times 10^{-6} \text{ V/Hz}. \tag{4.29}$$

4.5 Input and output optics

The laser power stabilization and Doppler noise cancellation are performed in the input laser system. In this section, we check their performance.

4.5.1 Laser power stabilization

The laser-power fluctuation noise is caused by the fluctuation of an intra-cavity power, and the transmitted light power is proportional to the intra-cavity laser power. Therefore, we stabilize the laser power in order to make transmitted light stable for reducing the laser-power fluctuation noise.

The setup for the laser power stabilization is shown in Fig. 4.22. Laser

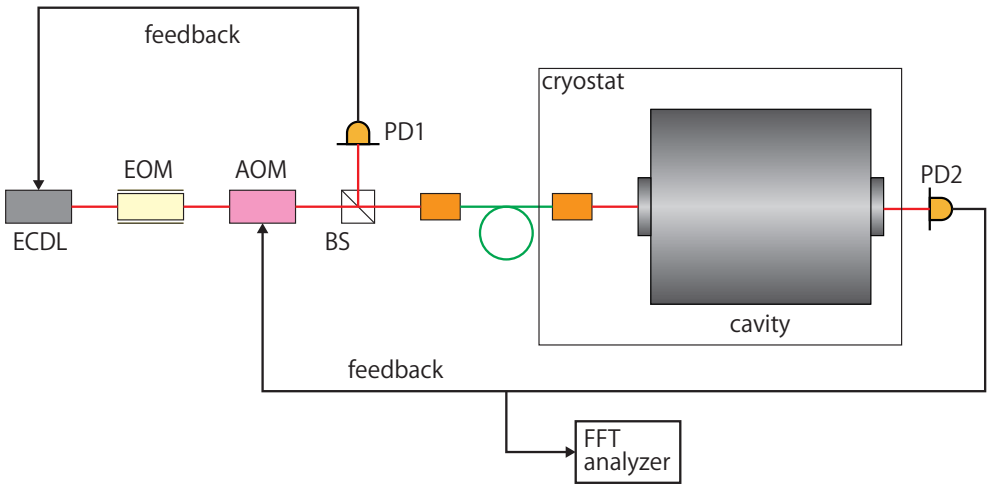

Figure 4.22: Setup for the laser power stabilization. The laser power is stabilizaed so as to make the transmitted laser power 90 μW. The laser power stability is estimated by using the signal of the PD2.

stabilization is achieved by feeding back the signal of the PD2 to AOM using the feedback circuit (see detail in Appendix C). The output from the monitor port of the feedback circuit is converted to the spectrum by the FFT analyzer, and used for evaluating the laser power fluctuation.

The transmitted laser power is about 90 μW. The amplitude and the frequency supplied to the AOM is about 160 MHz and 36 dBm, respectively. The PD2 is the InGaAs PD G12181-020K and the trans-impedance gain of the circuit is 10^4. The window function for calculating the spectrum is the hamming window function.

Figure 4.23 shows the power fluctuation spectra of the free-running and stabilized laser.

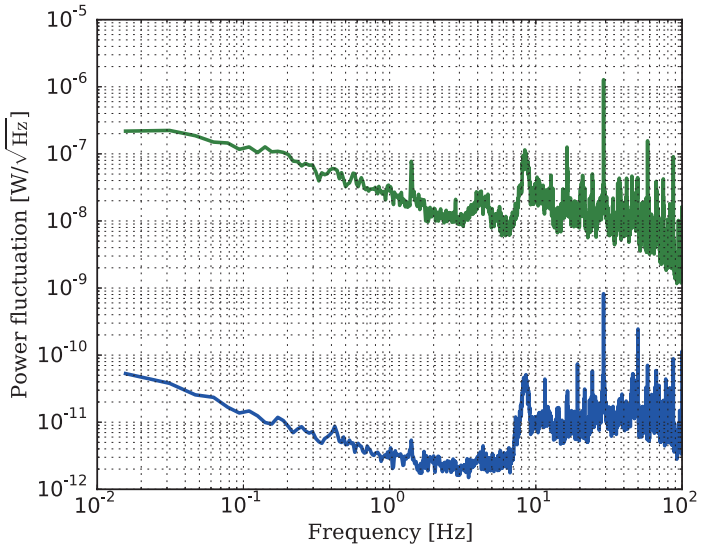

Figure 4.23: Spectra of the transmitted laser power fluctuation. The blue line is the inloop spectrum with the laser power fluctuation being stabilized. The green line is the free-run spectrum of the laser power.

4.5.2 Doppler noise cancellation

When Doppler noise cancellation is applied, the effect from the fluctuation of the traveling path is negligible, and the effect from the length fluctuation of a short arm of a DAMI will be significant. Moreover, there are some optical paths to which the Doppler noise cancellation technique cannot be applied. We therefore evaluate the phase modulation of these optical paths in this subsection.

All the optical paths without Doppler noise cancellation, which can affect the stability of our laser, is inside the windshield. Then, we make a Mach-Zehnder interferometer and measure the differential phase fluctuation of the two arms.

Figure 4.24 shows the setup for measuring the phase fluctuation inside the windshield. The phase difference between two arms of the interferometer is measured by the PD inside the figure, and this PD's signal is converted to the voltage spectrum by the FFT analyzer. The window function for calculating

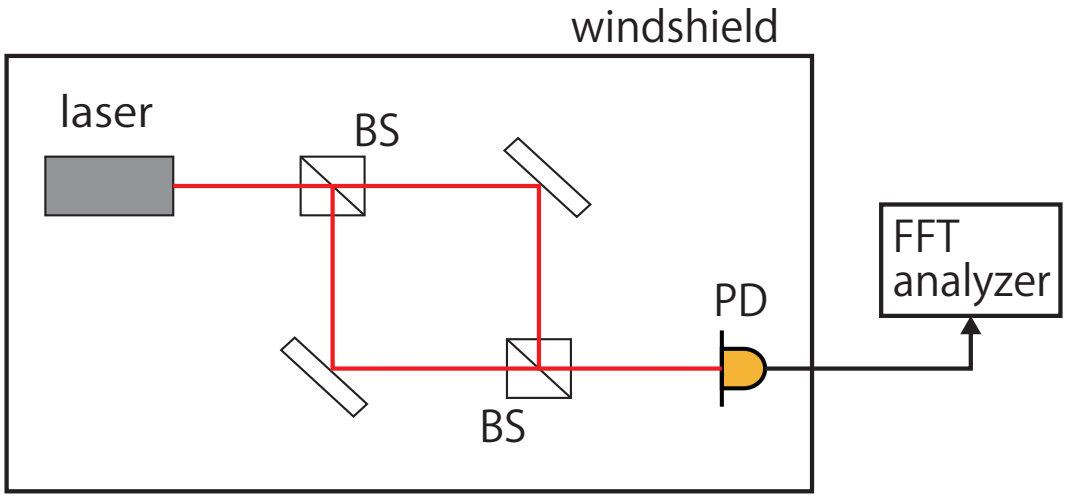

Figure 4.24: Setup for measuring the phase-fluctuation level in traveling the optical paths inside the windshield. The PD in this figure is the InGaAs photo detector G12180-003A with the trans-impedance circuit (details in Appendix C). The stable laser is the same one in Fig. 3.8.

the voltage spectrum is the hamming window function. Each arm length of the interferometer is about 50 cm in this experiment, which is as long as the optical path without the Doppler noise cancellation system in our input and output optics. The windshield is a plastic box which is the same as that used in our laser system.

In this setup, the PD voltage difference between the bright and the dark state is measured as

$$\Delta V = 3.84 \text{ V}. \tag{4.30}$$

The phase-fluctuation spectrum can be calculated as

$$\sqrt{G_\phi(f)} = \frac{2\pi}{\Delta V}\sqrt{G_V(f)} = 1.94\sqrt{G_V(f)} \text{ [rad}/\sqrt{\text{Hz}}\text{]}, \tag{4.31}$$

where $G_V(f)$ is a voltage spectrum of a PD. Then, we can estimate the phase modulation inside the windshield as in Fig. 4.25.

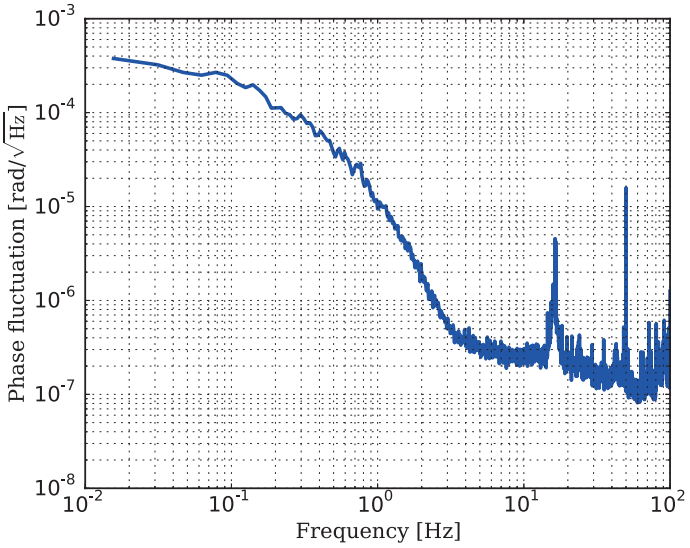

Figure 4.25: Phase-fluctuation spectrum of a Mach-Zehnder interferometer inside the windshield.

4.6 Summary of this chapter

- We checked the performance of our experimental setup and measured the behaviors of environmental noise sources.
- The results of the measurements and estimations are summarized in Table 4.1

amplitude transmittance	$t_{\mathrm{F}} = t_{\mathrm{E}} = 3.24 \times 10^{-3}$
FSR	$\nu_{\mathrm{FSR}} = 7.49(1) \times 10^{8}$ Hz
amplitude reflectance	$r_{\mathrm{F}} = r_{\mathrm{E}} = 0.99998913(4)$
amplitude loss	$l_{\mathrm{F}} = l_{\mathrm{E}} = 3.35(2) \times 10^{-3}$
cavity finesse	$\mathcal{F} = 1.445(6) \times 10^{5}$
FWHM	$\nu_{\mathrm{FWHM}} = 5.19(2) \times 10^{3}$ Hz
FPC time constant	$\tau_{\mathrm{FPC}} = 3.07(1) \times 10^{-5}$ s
PVIS cutoff frequency	$f_{\mathrm{P}X} = 8.5(2)$ Hz
	$f_{\mathrm{P}Y} = 8.8(2)$ Hz
	$f_{\mathrm{P}Z} = 21(2)$ Hz
PVIS quality factor	$Q_{\mathrm{P}X} = 2.9(1)$
	$Q_{\mathrm{P}Y} = 3.4(1)$
	$Q_{\mathrm{P}Z} = 1.2(1)$
vibration sensitivity	$A_X = 2.5(3) \times 10^{-10}$ /(m/s^2)
	$A_Y = 4.6(5) \times 10^{-11}$ /(m/s^2)
	$A_Z = 7(1) \times 10^{-12}$ /(m/s^2)
PDH gain	$G_{\mathrm{PDH}} = 4.4(4) \times 10^{-6}$ V/Hz
laser power coupling index	$\beta = 1.6(2) \times 10^{-7}$
seismic acceleration spectrum	shown in Fig. 4.4
AVIT open loop transfer function	shown in Fig. 4.9 to Fig. 4.11
2nd head temperature fluctuation	shown in Fig. 4.15
outer shield temperature fluctuation	shown in Fig. 4.16
laser power fluctuation	shown in Fig. 4.23
Doppler phase fluctuation	shown in Fig. 4.25

Table 4.1: Table of various parameters of our setup

Chapter 5
Stability Estimation

In this chapter we show the final stability of our frequency stabilization.

5.1 Noise estimation

In the previous chapter, we discussed the performance and environmental noise sources of our experiment. In this section, we estimate the noise levels of several noise sources using the results of the previous chapter.

5.1.1 Thermal noise

According to a theoretical calculation, we can estimate the noise level of the thermal noise as

$$\frac{\delta\nu}{\nu} = \frac{2.0 \times 10^{-17}}{\sqrt{f}} \ /\sqrt{\mathrm{Hz}}. \tag{5.1}$$

5.1.2 Residual gas noise

The residual gas noise is determined by the vacuum level of the cryostat. The vacuum level of our experiment is measured to be

$$p = 2.5 \times 10^{-5} \text{ Pa}. \tag{5.2}$$

Using this pressure and the result of Eq. (3.23), we can estimate the residual gas noise as

$$\frac{\delta\nu}{\nu} = 5.0 \times 10^{-20} \ /\sqrt{\mathrm{Hz}}. \tag{5.3}$$

5.1.3 Acceleration noise

The acceleration applied to a reference cavity is shown in Fig. 4.12, and the vibration sensitivity of our reference cavity is measured as Eq. (4.19) to Eq. (4.21). Then, using Eq. (2.73), we can estimate the noise level of the acceleration noise, as shown in Fig. 5.1.

In this result, the noise level is dominantly determined by the acceleration along the X axis, which is parallel to the optical axis of the reference cavity. This noise level is much larger than that we planned for in our designed. The main reason for this result is that the vibration sensitivities are much higher than we had assumed, especially the vibration sensitivity along the X axis. If the vibration sensitivities satisfy the requirement, 10^{-11} /(m/s^2) in all translational axes, the acceleration noise could be about 20-times smaller than that expressed in Fig. 5.1. Since the vibration sensitivity of our cavity is insensitive to the support point of the cavity, we should modify the shape of our FPC so as to reduce the vibration sensitivity.

Another reason is that the seismic acceleration level in our laboratory is larger than that which we had anticipated from Eq. (3.7), especially at over 10 Hz. Since the AVIS cannot produce good vibration isolation at high frequencies, we should use another passive vibration isolation structure whose resonant frequency is much smaller than that of our PVIS.

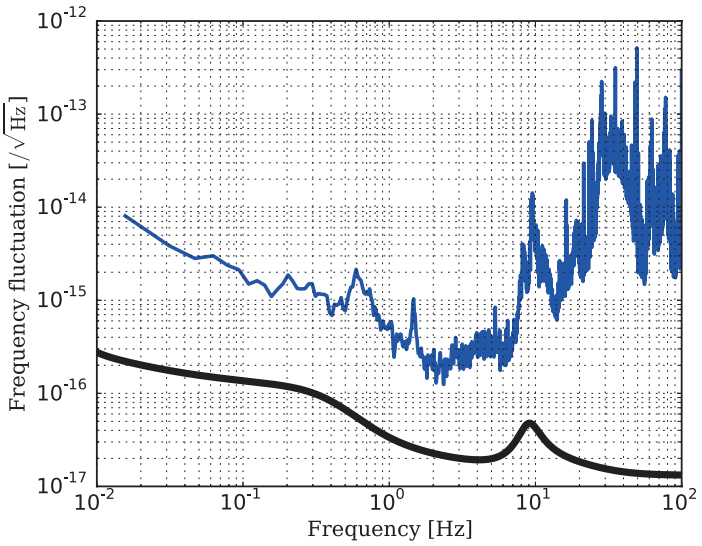

Figure 5.1: Frequency-fluctuation spectrum of the acceleration noise. The black line is the designed noise spectrum of our experiment.

5.1.4 Temperature-fluctuation noise

The temperature fluctuations of the 2nd stage and the outer shield are measured as shown in Fig. 4.15 and Fig. 4.16. The CTE of silicon is below 10^{-9} /K when the temperature of an optical cavity is below 18 K [23]. Both the heat capacity and the thermal conductivity have the same temperature dependence, proportional to T^3, at very low temperature. Then, the transfer function of the heat transfer hardly changes the operation temperature of a reference cavity. Thus, using the calculation result of the transfer function, we can estimate the temperature-fluctuation noise, as shown in Fig. 5.2.

In this result, the frequency fluctuation of the temperature-fluctuation noise is limited by the temperature fluctuation from an outer shield. Since this noise level is much smaller than the noise spectrum that we designed, the temperature-fluctuation noise does not disturb us from reaching the 10^{-17} level stability.

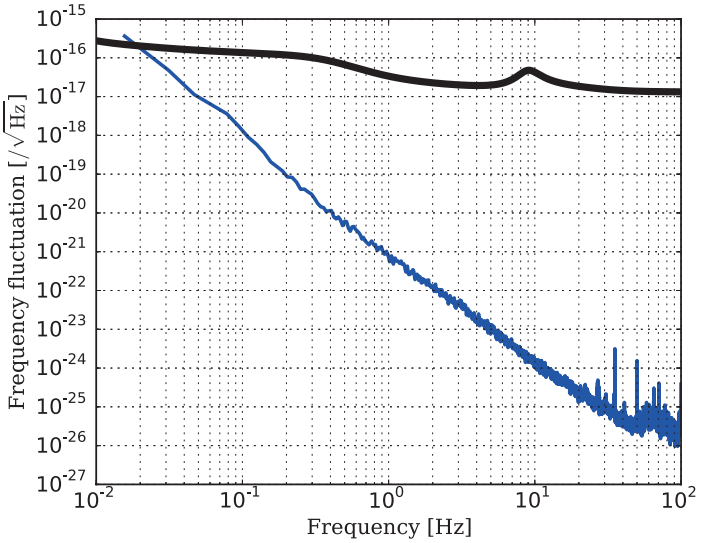

Figure 5.2: Frequency-fluctuation spectrum of the temperature-fluctuation noise. The black line is the designed noise spectrum of our experiment.

5.1.5 Laser power fluctuation noise

The laser-power fluctuation noise can be estimated using Eq. (4.22). The coupling index, β., is determined as in Eq. (4.23), and the laser-power fluctuation is measured as shown in Fig. 4.23. The normalized frequency spectrum of the laser-power fluctuation noise can thus be estimated as shown in Fig. 5.3.

In this result, the frequency fluctuation of this noise is small enough to achieve the 10^{-17} level stability.

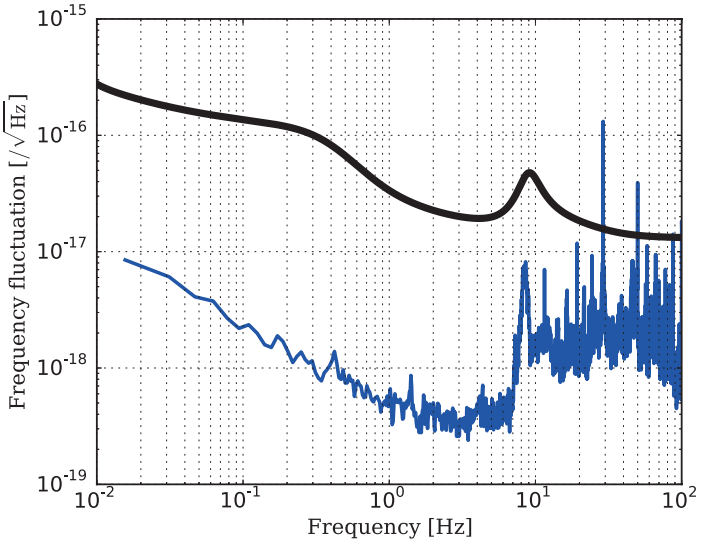

Figure 5.3: Frequency-fluctuation spectrum from the laser power-fluctuation noise. The black line is the design noise spectrum of our experiment.

5.1.6 Circuit noise

The circuit noise can be estimated by using a feedback circuit. Using the spectrum of the output voltage of amplifier1 in the feedback circuit (Fig. 4.19), we can estimate the frequency-fluctuation spectrum as

$$\frac{\delta\nu}{\nu} = \frac{\sqrt{G_{\mathrm{AG}_1}(f)}}{G_1 G_{\mathrm{PA}} G_{\mathrm{PDH}}}, \tag{5.4}$$

where $G_{\mathrm{AG}_1}(f)$ is the PSD of the output voltage of amplifier1.

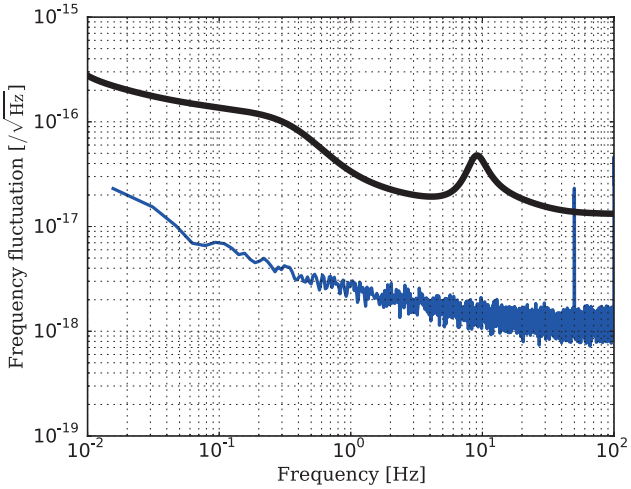

Figure 5.4: Frequency-fluctuation spectrum from the circuit noise. The black line is the design noise spectrum of our experiment.

When we turn off the laser and measure $G_{\mathrm{AG}_1}(f)$, only the circuit noise appears. Figure 5.4 shows the circuit noise level estimated by Eq. (5.4).

In this result, since the frequency fluctuation of the circuit noise is sufficiently small, the circuit noise does not disturb us from reaching the 10^{-17} level stability.

5.1.7 Shot noise

When we use a laser without any phase modulation, the shot noise and the circuit noise appear in the voltage spectrum, $G_{\mathrm{AG}_1}(f)$. Since the shot-noise level depends on the laser power entering a PD, the laser power is adjusted to be the same as the reflected light power at the time when the laser light is resonate with a FPC.

The result of this measurement is the same as that of the circuit-noise estimation. Then, the shot noise level of our experiment can be estimated as

$$\frac{\delta\nu}{\nu} < 1.7 \times 10^{-18} \ /\sqrt{\mathrm{Hz}}. \tag{5.5}$$

This result is also small enough to reach the 10^{-17} level stability.

5.1.8 RAM noise

When we use the AR reflection signal of a PD4 instead of that of a PD1 (Fig. 3.8), the RAM noise, the shot noise, and the circuit noise appear in the voltage spectrum, $G_{\mathrm{AG_1}}(f)$ [44]. The laser power is adjusted to be the same value as the reflected light power resonating with a FPC, because the RAM noise depends on the laser power entering a PD.

Using the spectrum $G_{\mathrm{AG_1}}(f)$ and Eq. (5.4), we can estimate the RAM noise, as shown in Fig. 5.5. This result is dominantly determined by the RAM noise, because the noise level of the shot noise and the circuit noise is smaller than that in Fig. 5.5. The frequency fluctuation of the RAM noise is the same as that which we designed. Thus, the RAM noise also does not disturb us from achieving the 10^{-17} level stability.

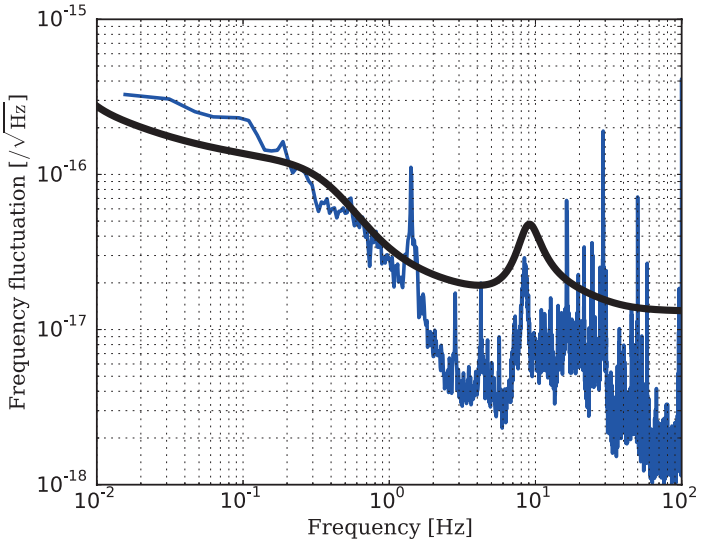

Figure 5.5: Frequency-fluctuation spectrum of the RAM noise. The black line is the design noise spectrum of our experiment.

5.1.9 Doppler noise

We use a Doppler noise cancellation system in our experiment. Thus, all of the traveling paths that lead to a laser phase fluctuation is in the windshield. We can therefore estimate the Doppler noise level by measuring the phase fluctuation traveling inside the windshield. Figure 4.24 shows the experimental setup for estimating the noise level of the Doppler noise.

The frequency-fluctuation spectrum caused by the phase fluctuation can be expressed as

$$\sqrt{G_\nu(f)} = f\sqrt{G_\phi(f)}. \tag{5.6}$$

Then, the spectrum of the normalized frequency fluctuation can be written as

$$\frac{\delta\nu}{\nu} = \frac{f\sqrt{G_\phi(f)}}{\nu}. \tag{5.7}$$

Using Eq. (5.7) and the phase-fluctuation spectrum, as shown in Fig. 4.25, we can estimate the Doppler noise while laser light travels in the windshield, as shown in Fig. 5.6. In this result, the noise level of the Doppler noise is much lower than the designed noise budget. Therefore, the Doppler noise is not a problem for reaching 10^{-17} level stability.

5.1.10 Total noise

Assuming that all of the noises we discussed in this section are uncorrelated, we can estimate the total noise spectrum by calculating the square root of the sum of squares of all noises. The total noise is shown in Fig. 5.8. Using this result and Eq. (3.33), we can estimate the frequency stability of our experiment, as shown in Fig. 5.8.

The frequency-fluctuation spectrum is dominantly determined by the acceleration noise. We can therefore improve the stability of our laser by reducing the acceleration noise.

The estimated frequency stability of our laser is $\sigma_y \simeq 2\times10^{-15}$ at 1 second. This stability is 20-times more unstable than our goal: the 10^{-17} level.

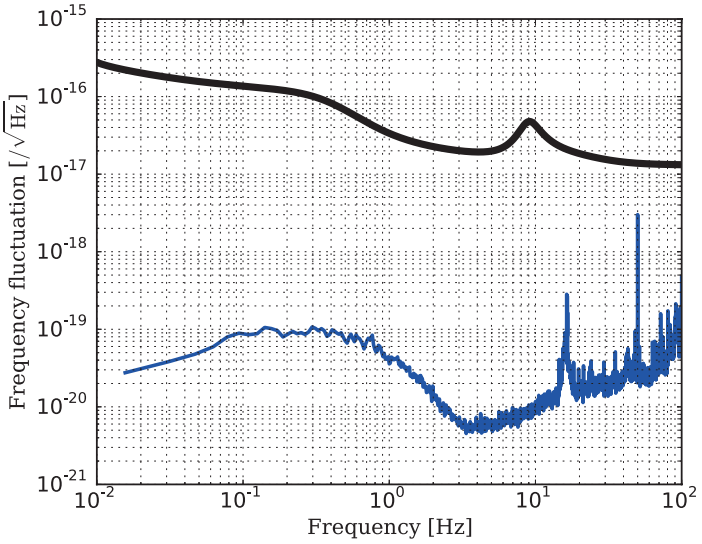

Figure 5.6: Frequency-fluctuation spectrum of the Doppler noise. The black line is the design noise spectrum of our experiment.

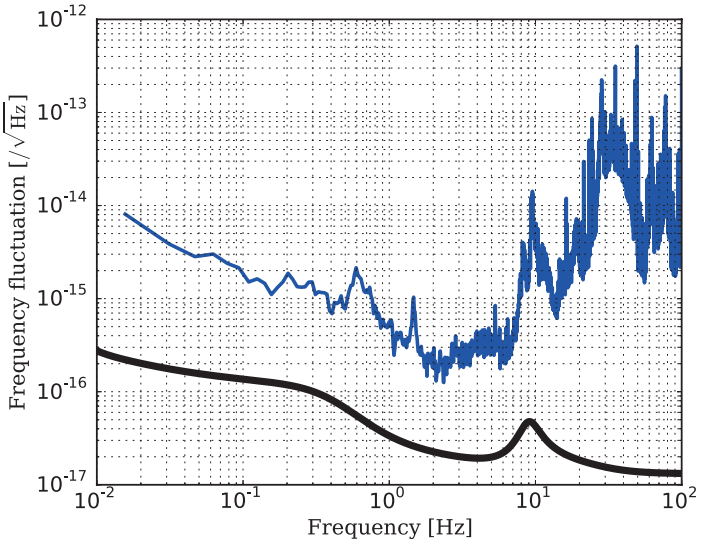

Figure 5.7: Frequency fluctuation spectrum of the total noise of our experiment. The black line is the designed noise spectrum of our experiment.

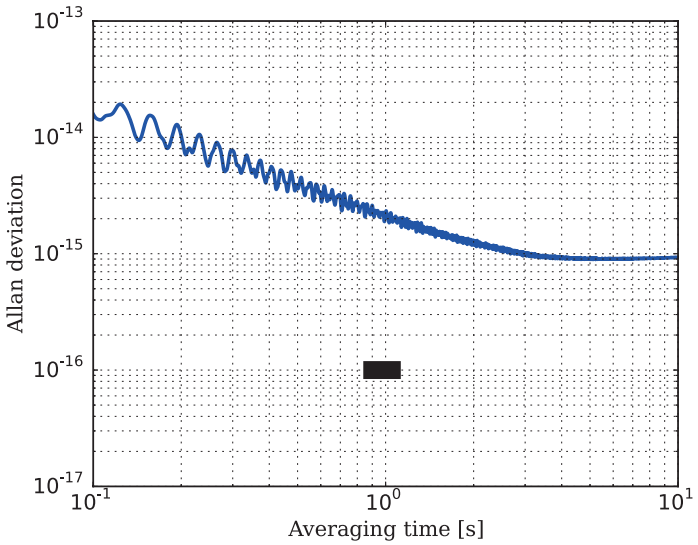

Figure 5.8: Result of our estimation for the frequency stability of our experiment. Our goal is below the black rectangle.

5.2 Frequency instability measurement

We discussed the total noise of our experiment in Section 5.1. The frequency stabilization of the laser is limited by the acceleration noise. In this section, we consider how to measure the frequency instability directly, and check that the acceleration noise actually limits the stability of our laser without any doubt.

5.2.1 Experimental setup

We show a schematic diagram of the experimental setup for the frequency-instability measurement in Fig. 5.9. The frequency instability is determined by measuring the beat frequency between two lasers. Since the beat-frequency fluctuation is dominantly determined by a laser whose instability is the larger of the two, we should prepare a more stable laser than ours in order to measure the instability of our laser. The stable laser in Fig. 5.9 has a 10^{-16} level stability from the averaging time, $\tau = 0.1$ s, to $\tau = 10$ s. Since the estimated instability of our laser is at the 10^{-15} level, this laser is enough stable to measure the instability of our laser. The beat frequency is measured using the PD5 and

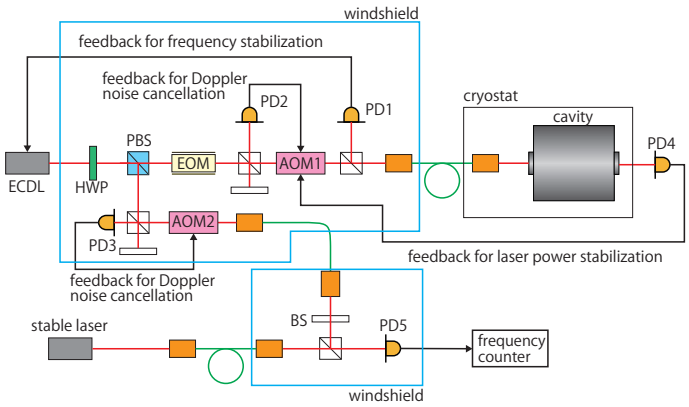

Figure 5.9: Setup for measuring the instability of our laser. PD1 is used for obtaining the PDH signal for frequency stabilization. PD1 , PD2, PD3, and PD5 are InGaAs photo detectors G12180-003As, and PD4 is an InGaAs photo detector, G12181-020K. Each PD has a trans-impedance circuit, and each feedback system is achieved by an analog electric circuit. Details of these circuits are given in Appendix C. The stable laser is the same one as in Fig. 3.8. The frequency counter is an Agilent 53230A.

the frequency counter.

During this instability measurement, the Doppler noise cancellations and the laser-power stabilization are operated. Doppler noise cancellations are achieved by feeding back the signals of the PD2 and the PD3 to the frequency of the RF signal to the AOM1 and the AOM2, respectively. Laser power stabilization is achieved by feeding back the signal of the PD4 to the amplitude of the RF signal to the AOM1.

Moreover, we use the simplified thermal isolation setup during the measurement for reducing the initial cooling time. Figure 5.10 shows a schematic of the simplified setup inside the cryostat. The main change is done in three parts. The first is to remove the stainless thermal resistance between the 2nd base of the refrigerator and the middle shield. The second is to take off the inner radiation shield. The third is to reduce the number of floors of the thermal-isolation stacks. Owing to these changes, the cavity is thermally well connected to the 2nd base of the refrigerator. It takes therefore about two days to cool a reference cavity, while it takes over two months for the designed setup to cool.

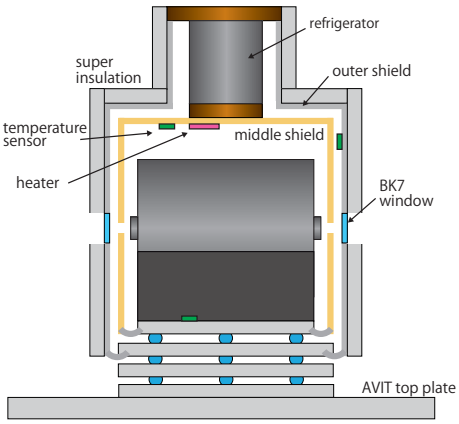

Figure 5.10: Simplified setup for reducing the cooling time. The temperature sensors are mounted at the forth floor of the thermal-isolation stacks, the middle radiation shield, and the outer radiation shield (the green parts in the figure). There are also heaters at the middle radiation shield and the outer radiation shield for changing the temperatures (the pink part in the figure).

5.2.2 Instability measurement

We measure the beat frequency between the two laser frequencies. The gate time of the frequency counter is 10 ms. The absolute value of the beat frequency is about 220 MHz. The transmitted light power is about 90 μW. The modulation frequencies of the EOM and the AOM are about 15 MHz and 160 MHz, respectively. The modulation voltages of the EOM and the AOM are about 12 dBm and 36 dBm, respectively. The temperature around the cavity is about 10 K during the measurement, and the wavelength of our laser is about 1397 nm.

Figure 5.11 shows the beat frequency between our laser and the stable laser without operating the AVIT. From this result, we can directly calculate the Allan deviation of the frequency fluctuation, as shown in Fig. 5.12. The stability seems to be dominantly limited by the stability of our silicon optical cavity, because the stability of this result is much higher than that of the stable laser used for the beat measurement. The stability at most stable time scales is measured at an Allan deviation of

$$\sigma_y = (7.03^{+0.38}_{-0.34}) \times 10^{-15} \ (\tau = 0.8 \text{ s}). \tag{5.8}$$

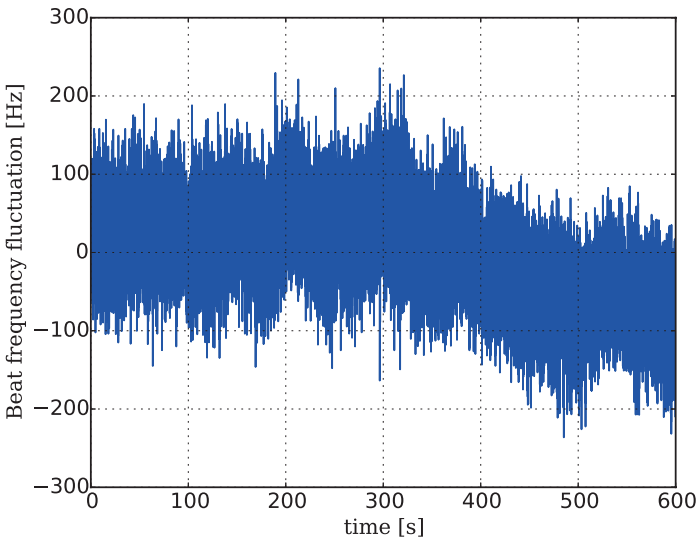

Figure 5.11: Beat-frequency fluctuation between our laser and another narrow-linewidth laser. The gate time of the frequency counter is $\tau = 10$ ms.

The error of this result is the 95% confidence interval of the χ^2 distribution of the measurement. In at previous work with the cryogenic optical cavity at very low temperature, the stability of the laser was $\sigma_y \simeq 2 \times 10^{-14}$ at around 1000 seconds and $\sigma_y \simeq 2 \times 10^{-13}$ at around 1 second [23]. Therefore, our laser is the most stable one with a very low temperature optical cavity at around 1 second, which is an important time scale for applying a laser to an optical lattice clock. Note that the stability at around 1 second in the previous work is read from a graph of the Allan deviation in Ref. [23].

Figure 5.13 shows the spectra of the beat frequency and estimated noise spectrum using the vibration sensitivity and acceleration spectrum without operating the AVIT. Since the spectrum estimated by the acceleration noise coincides with that of the beat measurement at over 1 Hz, the stability of our laser is definitely limited by the acceleration noise.

On the other hand, the spectrum below 1 Hz cannot be explained by the acceleration noise. This noise level can be considered to be the temperature-fluctuation noise from the 2nd stage of the refrigerator. Since we use the simplified thermal isolation system during this stability measurement, the

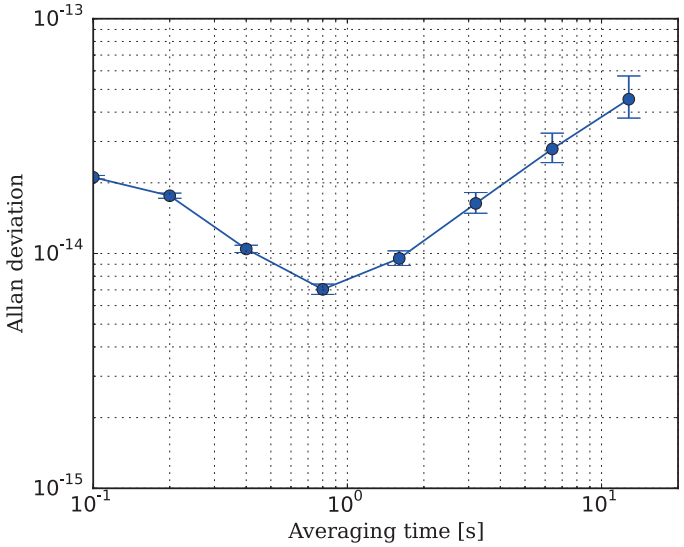

Figure 5.12: Allan deviation of the beat frequency. The error bars represent the 95% confidence intervals of the measurement. Our goal stability is below the black rectangle.

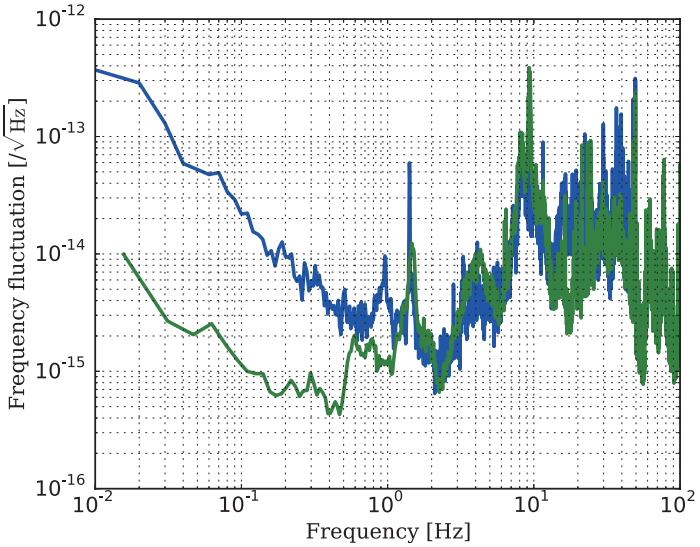

Figure 5.13: Frequency-fluctuation spectrum. The blue line is the measured value and the green line shows the estimated frequency-fluctuation spectrum with the vibration sensitivity and the acceleration spectrum.

temperature-fluctuation noise is much larger than that which we estimated in Fig. 5.2. In simplified setup, the 2nd base of the refrigerator is directly connected to the middle radiation shield, and the silicon optical cavity is put directly on the fourth floor of the thermal-isolation stacks. Therefore, the temperature fluctuation from the 2nd stage of the refrigerator travels well to the optical cavity. Thus, the transfer function of the temperature fluctuation from the 2nd stage to the cavity is dominantly determined by the connection part of the middle shield and the stack: thin OFC wires and aluminum foils.

We can directly measure the transfer function of the temperature fluctuation using the temperature sensors and heaters in the cryostat. Figure 5.14 shows a schematic of the setup for measuring the transfer function from the middle shield to the thermal-isolation stack. Temperature sensors (DT-670, Lake Shore Cryogenics) are mounted at the middle radiation shield and the forth floor of the thermal-isolation stacks. A heater is also mounted at the middle radiation shield. When we apply a periodic voltage to the heater, the temperature sensor outputs the periodic temperature signals. We can therefore measure the transfer function by calculating the ratio of the amplitude of the sensors. The heater is about 50 Ω, and the amplitude of the supplied voltage to the heater is between 1 V and 10 V.

Figure 5.15 shows the measured gain of the transfer function from the middle shield to the thermal-isolation stack. In theory, the transfer function of the temperature fluctuation can be written as in Eq. (3.13). Thus, by fitting these measured values with the function

$$|H| = \frac{1}{\sqrt{1 + (\omega RC)^2}}, \tag{5.9}$$

we obtain

$$RC = \frac{(2.2 \pm 0.2) \times 10^{-2}}{2\pi} \text{ Hz}. \tag{5.10}$$

This error is the fitting error of the measurement. Note that we only use data below 0.1 Hz for the fitting, because any measurement over 1 Hz is limited by the noise of the temperature sensor. Using this transfer function and the temperature spectrum in Fig. 4.15, we can roughly estimate the temperature fluctuation at the optical cavity. Now, assuming the CTE of silicon to be

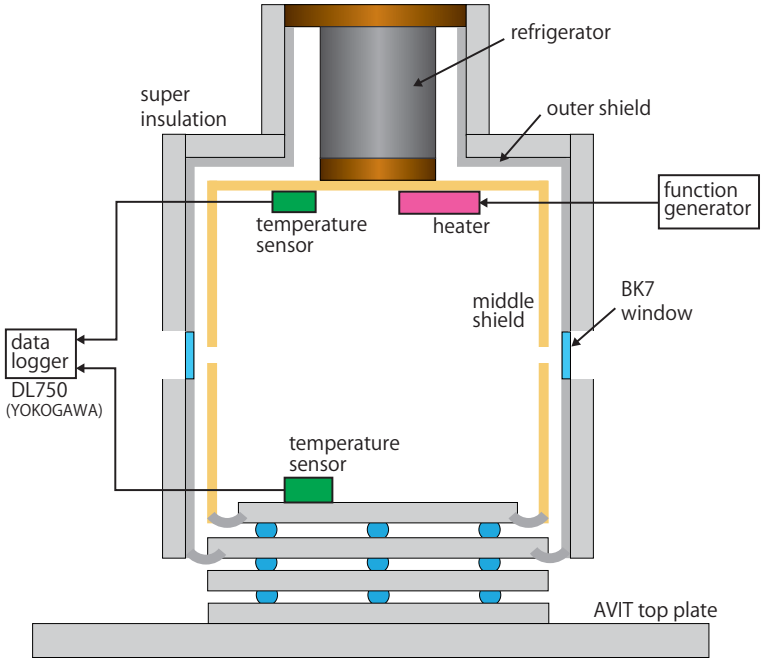

Figure 5.14: Schematic of the setup for measuring the transfer function of the temperature fluctuation.

$\alpha = 2.5 \times 10^{-10}$ /K so that the hight of the characteristic peak around 1.5 Hz is the same as the peak around 1.5 Hz in Fig. 5.13, the temperature-fluctuation noise is calculated as shown in Fig. 5.16.

In this result, the frequency of the peak of the temperature-fluctuation noise exactly coincides with the frequency of the peak in Fig. 5.13. Moreover, the CTE of silicon at 10 K is at the 10^{-10} /K level [23]. Thus, the assumed value of the CTE is not very different from the measured value. Note that the CTE of the silicon at 10 K is read from the graph of the CTE in Ref. [23]. Since the floor level of the temperature fluctuation spectrum in Fig. 4.15 is limited by the circuit noise, the actual temperature-fluctuation noise below 1 Hz should be smaller than that in Fig. 5.16. Therefore, this result is consistent with the measurement. Thus, the noise source limiting the stability of our laser below 1 Hz is likely to be the temperature-fluctuation noise. If we use the designed temperature isolation setup, the temperature-fluctuation noise can be reduced. Therefore, the full setup operation is a subject of future work.

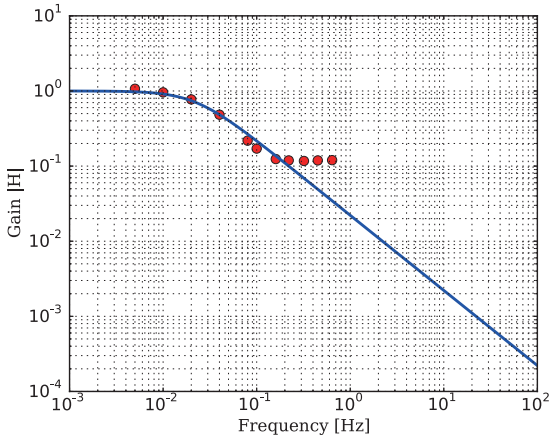

Figure 5.15: Gain of the transfer function of the temperature fluctuation from the middle radiation shield to the forth floor of the thermal-isolation stacks. The red dots are the measured values and the green curve is a fitting curve.

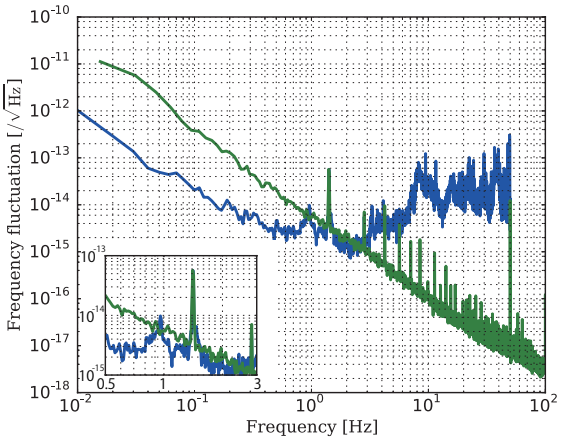

Figure 5.16: Frequency fluctuation of our laser and the estimated temperature-fluctuation noise. The blue line is the frequency-fluctuation spectrum of the beat measurement. The green line is the frequency-fluctuation spectrum of the estimated temperature-fluctuation noise. The floor level of the green line shows the upper limit of the frequency fluctuation due to the temperature fluctuation. The inset is the enlarged view of the graph from 0.5 Hz to 3 Hz.

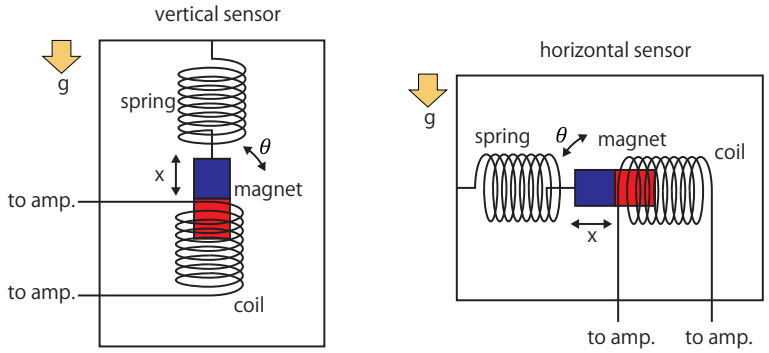

Figure 5.17: Schematic diagram of our vibration sensor's structure. Left is a vertical sensor and right is a horizontal sensor. The components are a magnet, a spring, and a coil. When the magnet moves, the coil gets induced voltage proportional to the velocity difference between the magnet and the coil.

Next, we tried to operate the AVIT for reducing the acceleration noise. However, when we operated the AVIT, the laser stability became worse than the result in Eq. (5.8). The reason for this result may be considered to be the tilt vibration of a reference cavity.

Figure 5.17 shows the structure of the vibration sensor in our experiment. When the vibration sensor moves, it outputs a signal proportional to the vibration sensor's velocity. Then, the output of the vibration sensor for the translational movement can be written as

$$V_{\mathrm{Out}} = H_{\mathrm{VS}}\dot{x}, \tag{5.11}$$

where H_{VS} is a response function of the vibration sensors (L-22E, 510 Ω), which can be roughly approximated in the frequency domain as [43].

$$H_{\mathrm{VS}}(f) \simeq 47.1\sqrt{\frac{(f/2.0\ \mathrm{Hz})^2}{1+(f/2.0\ \mathrm{Hz})^2}}\ [\mathrm{V/(m/s)}]. \tag{5.12}$$

On the other hand, if the vibration sensor is tilted, the velocity of the

vibration sensor can be described as

$$\dot{x}^{\mathrm{V}} = g \int_0^t (1 - \cos\theta)\ dt \simeq 0 \text{ (vertical)}, \tag{5.13}$$

$$\dot{x}^{\mathrm{H}} = g \int_0^t \sin\theta\ dt \simeq g \int_0^t \theta\ dt \text{ (horizontal)}. \tag{5.14}$$

Therefore, the output signals are different between a vertical axis sensor and a horizontal axis sensor, and these can be described as

$$V_{\mathrm{out}}^{\mathrm{V}} = 0, \tag{5.15}$$

$$V_{\mathrm{out}}^{\mathrm{H}} = H_{\mathrm{VS}} g \int_0^t \theta\ dt. \tag{5.16}$$

Therefore, only the horizontal vibration sensor responds to its tilt.

Now, considering the output signal ratio between the translational displacement and the tilt movement in the frequency domain, it can be expresses as

$$R_{\mathrm{TR}} = \frac{V_{\mathrm{Out}}}{V_{\mathrm{Out}}^{\mathrm{H}}} = -\omega^2 \frac{\tilde{x}(\omega)}{g\tilde{\theta}(\omega)}. \tag{5.17}$$

Then, the signal of a horizontal vibration sensor is dominantly determined by the tilt movement at low frequency. Since the rotational vibration of the ground is very in general small, this effect does not appear at around 1 Hz.

However, in the AVIS, we use a feedback system for operating the AVIT. Then, when the input matrix and output matrix, which play a role of diagonalizing six degrees of freedom, are not correct, the tilt-movement effect appears in the output signal of the vibration sensor. Figure 5.18 shows the transfer function of the AVIT. In this result, the X axis and the Y axis curves are larger than the theoretical line, while Z-axis transfer function is comparable to theory. This is evidence of coupling between the translational displacement and the rotational movement below 1 Hz.

The rotational vibration of a reference cavity can be a large acceleration through a gravitational acceleration of Earth. Therefore, the reason why the AVIS does not work well is considered to be in the rotational vibration of a reference cavity.

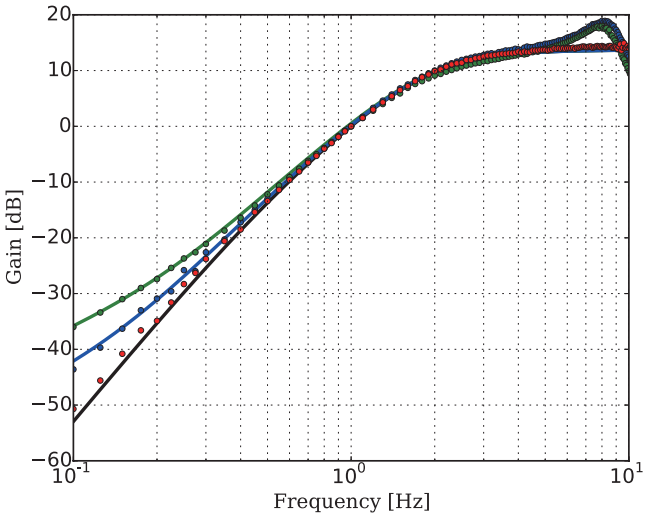

Figure 5.18: Transfer functions of the AVIT. The blue, green, and red dots show the measured values of the X, Y, and Z axes. The black solid line is a theoretical line without a tilt. The blue curve shows a theoretical curve with a 10% tilt coupling. The green line shows a theoretical curve with 25 % tilt coupling. All of the curves and dots are normalized so that the gain at 1 Hz is equal to 0 dB.

5.3 Estimation without the acceleration noise

In the last section, we described that the noise sources limiting our laser-frequency stability are the acceleration noise and the temperature-fluctuation noise. We therefore discuss the effect of other noises in this section.

The estimated frequency-fluctuation spectrum of our experimental noises without the acceleration noise is shown in Fig. 5.19. In this result, the noise level is dominantly limited by the RAM noise and the thermal noise.

By calculating the Allan deviation with the spectrum in Fig. 5.19, we obtain the Allan deviation, as shown in Fig. 5.20. This result suggests that if we make the acceleration noise is small enough, and use the designed thermal isolation setup, the instability of the laser of our experiment can reach the 10^{-17} level.

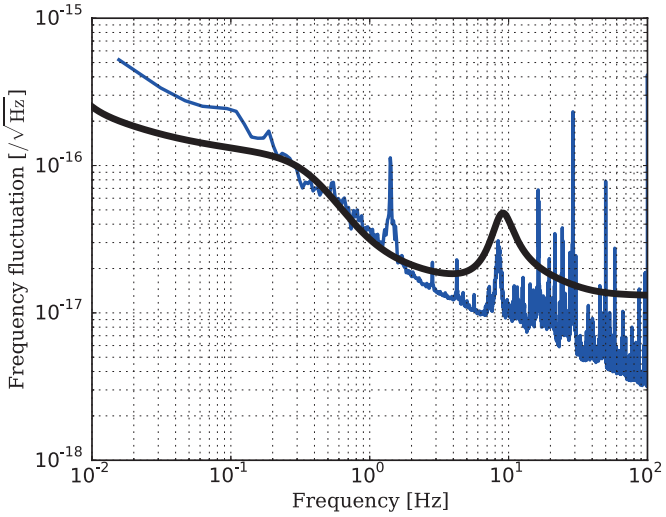

Figure 5.19: Normalized frequency spectrum of the noises in our experiment without the acceleration noise. The black line is the designed spectrum of our experiment.

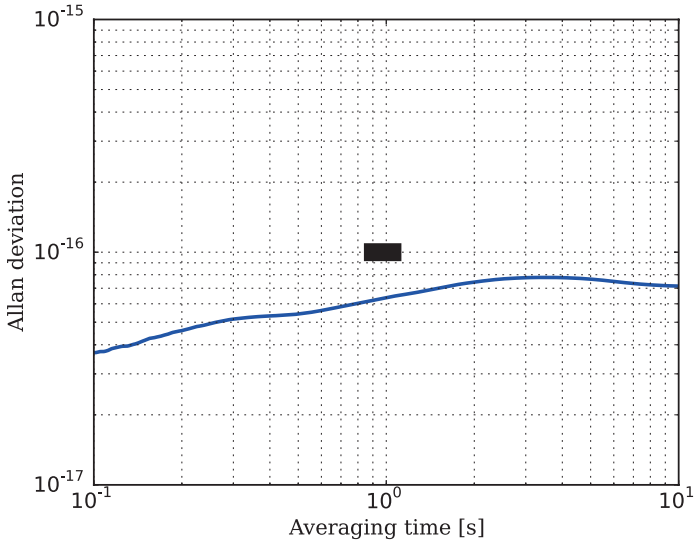

Figure 5.20: Allan deviation calculated using the spectrum in Fig. 5.19.

5.4 Summary of this chapter

- We estimated the effects of many noise sources, and showed that the acceleration noise is the most problematic one in our experiment.
- We directly evaluated the frequency fluctuation of our laser by measuring a beat frequency between our laser and another stable laser, which had a 10^{-16} level stability. The result of the direct measurement is consistent with the acceleration noise level at over 1 Hz.
- Our laser stability is $\sigma_{\mathrm{y}} = 7.0^{+0.38}_{-0.34} \times 10^{-15}$ at 0.8 second.
- Our laser is the most stable one stabilized with a cryogenic optical cavity at a very low temperature at around 1 second.
- The frequency fluctuation of our laser is probably limited by the temperature-fluctuation noise at below 1 Hz.
- In the experiment, the AVIS did not work well, probably because of the tilt coupling.
- The noise level of our laser can reach the 10^{-17} level if we make the acceleration noise small enough.

Chapter 6
Conclusion

In this chapter, we summarize our experiment and discuss the result. We also show future plans for increasing the laser stability.

6.1 Summary

In this work, we constructed a frequency stabilizing system, and stabilized a laser frequency with a very low-temperature optical cavity. Moreover, we estimated the noise contributions due to various effects, such as the vibration and temperature fluctuation, quantitatively. We then showed that the acceleration noise is the most problematic noise source for our system. We also measured the instability of our laser directly, and discussed the result. Then, we found that the problematic noise sources of our stabilization system with a cryogenic optical cavity are the acceleration noise and the temperature fluctuation noise. In addition, we also showed that other noise sources are small enough for reaching the 10^{-17} level stability.

We stabilized a laser frequency using a cryogenic monocrystalline silicon optical cavity. Since monocrystalline silicon has a very high mechanical Q factor, especially at cryogenic temperature, we can efficiently reduce the thermal noise of the cavity spacer and mirrors. Moreover, the CTE of this material has a zero-cross point temperature at around 18 K. We can therefore also reduce the frequency fluctuation from the temperature fluctuation by controlling the cavity temperature at around 18 K.

The vibration isolation system is a very important component of our experiment, because the acceleration noise is one of the most problematic technical

noise sources for frequency stabilization with a reference cavity. A hexapod-type AVIT can easily decrease the low-frequency vibration compared with the PVIS. Moreover, AVIS can isolate the acceleration transferred through the heat link from the refrigerator, while the PVIS cannot isolate it. The PVIS is a strong structure for reducing the high-frequency vibration, while it is difficult for the AVIS to reduce the high-frequency acceleration due to the resonances of its structure.

Thermal-isolation stacks and radiation shields are other important components of our experiment for cooling an optical cavity and reducing the temperature-fluctuation noise. Thermal-isolation stacks are structures that consist of aluminum plates, stainless-steel inserts and glass balls. It can make a very steep gradient of the temperature from room temperature to very low temperature. The radiation shield plays a role for reducing the heat transfer from this radiation. There are glass windows at the input laser path that transmits the laser beam, which do not transmit the radiation heat to an optical cavity.

For concerning the input laser system, the laser-power stabilization and the Doppler noise cancellation techniques are used. The laser-power stabilization system with the transmitted light decreases the laser-power fluctuation noise. The Doppler noise cancellation system reduces the phase fluctuation, while a laser beam travels some optical paths. Each system is an essential component for reaching the 10^{-17} level frequency stability.

Using these components, we have designed a reference cavity for reaching 10^{-17} level stability. The designed performance is dominantly limited by three noises: thermal noise, acceleration noise and RAM noise.

Using the designed setup, we have obtained a frequency stability of $\sigma_y = 7.03^{+0.38}_{-0.34} \times 10^{-15}$ at 0.8 second. This laser is the most stable at around 1 second by using a cryogenic optical cavity at very low temperature. Note that we turned off the AVIS, and used the simplified thermal isolation setup when we must obtain the above frequency stability.

This stability is dominantly limited by the acceleration noise and the temperature-fluctuation noise. Thus, we can improve the stability by reducing the acceleration noise and vibration sensitivity of a reference cavity and constructing the designed setup for temperature-fluctuation noise reduction.

6.2 Future prospects

The laser-frequency stability is limited by the acceleration noise in our experiment as well as the temperature-fluctuation noise. Therefore, by decreasing the acceleration noise and the temperature-fluctuation noise, the laser stability should be improved. Since the temperature-fluctuation noise will be small when we use the designed setup for thermal isolation, we only consider the reduction method of the acceleration noise in this subsection. There are several methods to reduce this acceleration noise.

First, we should make the diagonalization of vibration signals on the AVIT more exactly. In the recent configuration, the AVIS didn't help us to improve the stability of our laser. This is because the diagonalization matrix is not exactly correct, and the top plate of the AVIT is tilted when we operate the AVIT. Thus, by decreasing the coupling between the translational vibration signals and the rotational ones, the AVIS should work better, and we can reduce the low-frequency acceleration of a reference cavity.

The second method is to use a stronger PVIS, such as an air spring vibration isolator, an inverted pendulum, a geometrical anti-spring filter, etc. These passive vibration isolators have very low resonant frequencies, from around 0.1 Hz to 0.5 Hz, and small Q factor. Then, the vibration-isolation ratio improves by more than 100-times larger at high frequency.

The third method is to decrease the vibration sensitivity of a reference cavity. Our cavity has a much larger vibration sensitivity than that which we designed; it is insensitive to the support point of an optical cavity because the aspect ratio of our cavity is close to one. However, if we remake the cavity, which has the relevant aspect ratio, for example at around four, which is the aspect ratio used in a cavity whose vibration sensitivity is below 10^{-11} /(m/s^2) in all translational axis [12], the vibration sensitivity should be more sensitive to changing the support points, and we can adjust the support point for making the vibration sensitivity smaller.

Fourthly, we could move our experimental setup to a place that has a smaller seismic vibration, like Kamioka in Japan. The vibration levels from 1 Hz to 100 Hz at Kamioka are about 100-times smaller than those at our laboratory at RIKEN in Saitama Prefecture [46]. The stability of the laser

frequency could be improved even if we do not change any configuration of our experiment.

6.3 Conclusion

The laser-frequency stability has been gradually improving during the last decade, and a state-of-the-art cavity-stabilized laser has been approaching the thermal noise limit of the reference cavity. Therefore, it is inevitable for further improvements of the laser stability to utilize a cryogenic cavity operated at a very low temperature.

In this work, we stabilized the laser frequency with a cryogenic optical cavity, and the stability of our laser is measured at an Allan deviation of $\sigma_{\mathrm{y}} = 7.03^{+0.38}_{-0.34} \times 10^{-15}$. This stability is worse than that of the very stable lasers in the world. However, our laser is the most stable laser stabilized with a cryogenic optical cavity operated at very low temperature at around 1 second.

Moreover, we have studied various noise sources that may disturb the laser stabilization, and found that our laser stability is limited by the acceleration noise and the temperature-fluctuation noise. In addition, the other noise sources, such as the laser-power fluctuation noise, the RAM noise, etc, are small enough for achieving the 10^{-17} level of stability. In this way, our work reveals the prospects for reaching the 10^{-17} level of stability.

Since cooling the cavity at a very low temperature is an indispensable technique for further improving the laser stability, for example 1×10^{-17}, our work is an important step for making an ultrastable laser in the future.

Appendix A
Gaussian Beam and Cavity Mode

In the main part of this thesis, we treated a laser beam using geometrical optics. However, in reality, the electromagnetic field of a laser beam practically has an intensity distribution, and we should consider this distribution in order to calculate some parameters of a laser, like a beam size. In Appendix A, we describe Gaussian beam optics.

A.1 Gaussian beam

The amplitude of a laser beam traveling in the direction along the Z axis can be expressed as

$$E(t,x,y,z) = \Psi(x,y,z)\mathrm{e}^{\mathrm{i}\Omega t - \mathrm{i}kz}, \tag{A.1}$$

where Ω is the angular frequency of a laser beam and $k = \Omega/c$ is the wave number. $\Psi(x,y,z)$ is the distribution of an electromagnetic field, which satisfies the following equation:

$$\left(\frac{\partial^2}{\partial x^2} + \frac{\partial^2}{\partial y^2} - 2\mathrm{i}k\frac{\partial}{\partial z}\right)\Psi(x,y,z) = 0. \tag{A.2}$$

One solution of this equation can be described as

$$\Psi(x,y,z) = \sqrt{\frac{k}{\pi z_\mathrm{R}}}\frac{\mathrm{i}z_\mathrm{R}}{q(z)}\mathrm{e}^{\left(-\frac{\mathrm{i}k}{q(z)}\frac{x^2+y^2}{2}\right)}, \tag{A.3}$$

where $q(z)$ is the wavefront coefficient, which can be written as

$$q(z) = z + \mathrm{i}z_{\mathrm{R}}, \tag{A.4}$$

where z_{R} is the Rayleigh range, which is expressed as

$$z_{\mathrm{R}} = \frac{kw_0^2}{2}. \tag{A.5}$$

Here, we consider the physical meaning of w_0. Using Eq. (A.3), the electromagnetic field distribution at $z = 0$ can be written as

$$\Psi(x, y, 0) = \sqrt{\frac{k}{\pi z_{\mathrm{R}}}} \mathrm{e}^{\left(-\frac{x^2+y^2}{w_0^2}\right)}. \tag{A.6}$$

From this equation, it is found that the amplitude of the electromagnetic field at a distance w_0 is 1/e of the amplitude at the center.

We now consider the functions $R(z)$ and $S(z)$ defined as follows:

$$\frac{1}{q(z)} = \frac{1}{R(z)} + \frac{1}{\mathrm{i}S(z)} \tag{A.7}$$

and define the function $w(z)$ as

$$w^2(z) = \frac{2S(z)}{k}. \tag{A.8}$$

Using Eq. (A.7) and Eq. (A.8), Eq. (A.3) can be written as

$$\Psi(x, y, z) = \sqrt{\frac{2}{\pi}} \frac{1}{w(z)} \mathrm{e}^{\left[-\left(\frac{1}{w^2(z)} + \frac{ik}{2R(z)}\right)(x^2+y^2) + \mathrm{i}\arctan(z/z_{\mathrm{R}})\right]}. \tag{A.9}$$

From the above calculation, $R(z)$ and $w(z)$ can be written as

$$R(z) = z\left[1 + \left(\frac{z_{\mathrm{R}}}{z}\right)^2\right], \tag{A.10}$$

$$\text{and } w(z) = w_0\sqrt{1 + \left(\frac{z}{z_{\mathrm{R}}}\right)^2}. \tag{A.11}$$

From Eq. (A.9), it is found that $R(z)$ is the radius of curvature of the equiphase plane of a laser beam, and $w(z)$ is the beam size at a distance of z.

A.2 Cavity eigen mode of a FPC

In order to resonate the laser beam to a FPC, $R(z)$ on the front and the end mirrors should be matched with the radii of curvatures (ROC) of the mirrors. So, $R(z)$ satisfies the equations as follows:

$$R(z_0) = z_0 \left[1 + \left(\frac{z_\mathrm{R}}{z_0}\right)^2\right] = -R_\mathrm{F}, \tag{A.12}$$

$$\text{and } R(z_0 + L) = (z_0 + L) \left[1 + \left(\frac{z_\mathrm{R}}{z_0 + L}\right)^2\right] = R_\mathrm{E}. \tag{A.13}$$

Here, z_0 is the coordinate of the front mirror and L is the cavity length; R_F and R_E are the radii of curvatures of the front and end mirrors, respectively. The sign of ROC is positive when the mirror surface inside a FPC is concave. From these equations, we can calculate z_0, z_R, and w_0 using the following equations:

$$z_0 = \frac{L - R_\mathrm{E}}{R_\mathrm{F} + R_\mathrm{E} - 2L} L, \tag{A.14}$$

$$z_\mathrm{R}^2 = \frac{k^2 w_0^4}{4} = \frac{L(R_\mathrm{F} - L)(R_\mathrm{E} - L)(R_\mathrm{F} + R_\mathrm{E} - L)}{(R_\mathrm{F} + R_\mathrm{E} - 2L)^2}. \tag{A.15}$$

We can thus calculate the beam size on the front and end mirrors using Eq. (A.11), Eq. (A.14), and Eq. (A.15).

We give some examples of the beam size on the mirrors in Table A.1

R_{F}	R_{E}	$w(z_0)$	$w(z_0 + L)$
0.5 m	0.5 m	3.33×10^{-4} m	3.33×10^{-4} m
0.5 m	1.0 m	3.77×10^{-4} m	3.27×10^{-4} m
0.5 m	∞	4.26×10^{-4} m	3.30×10^{-4} m
1.0 m	1.0 m	3.85×10^{-4} m	3.85×10^{-4} m
1.0 m	∞	4.71×10^{-4} m	4.22×10^{-4} m

Table A.1: Several examples of the beam size on the mirrors of a FPC. The parameters for the calculation are $L = 0.2$ m and $k = 4.50 \times 10^6$ rad/m.

Appendix B
Allan Deviation

When evaluating the frequency instability of a laser, the standard deviation cannot be used for the criterion of the frequency stability because it can be changed by the measurement time if the laser frequency has some drift. Therefore, the Allan deviation is often used for estimating the frequency stability, which is not varied by the measurement time, even if the frequency has a drift.

B.1 Definition

The Allan deviation is defined as

$$\sigma_y(\tau) = \sqrt{\frac{\langle (y_{i+1} - y_i)^2 \rangle}{2}}, \tag{B.1}$$

where $< X_i >$ means an ensemble average of X_i, and τ is a sampling interval; y_i is the i-th measured mean value of a physical quantity of $y(t)$, which is defined as

$$y_i = \frac{1}{\tau} \int_{t_i}^{t_i+\tau} y(t)\ dt. \tag{B.2}$$

An ensemble average can be defined as

$$< X_i >= \frac{1}{N} \sum_{n=1}^{N} X_i. \tag{B.3}$$

Then, Eq. (B.1) can be rewritten as

$$\sigma_y(\tau) = \sqrt{\frac{1}{2(N-1)} \sum_{n=1}^{N-1} (y_{i+1} - y_i)^2}. \tag{B.4}$$

In this thesis, we calculated the Allan deviation from the sampling data with Eq. (B.4).

B.2 Allan deviation and power spectrum

The PSD of the physical quantity y and its Allan deviation are connected as follows [47]:

$$\sigma_y(\tau) = \sqrt{\int_0^\infty G_y(f) H(f)\ df}, \tag{B.5}$$

where $H(f)$ is a dimensionless function, defined as

$$H(f) = 2\frac{\sin^4(\pi\tau f)}{(\pi\tau f)^2}. \tag{B.6}$$

We show the behavior of $H(f)$ as a function of Fourier frequency in Fig. B.1. Equation (B.6) means that the Allan deviation at an averaging time of τ is dominantly determined by the power spectrum at around $f = 1/2\tau$. Thus, in this thesis we calculated the Allan deviation using the frequency spectrum from about 0.01 Hz to 100 Hz with Eq. (B.5), because we care about the Allan deviation at around 1 second.

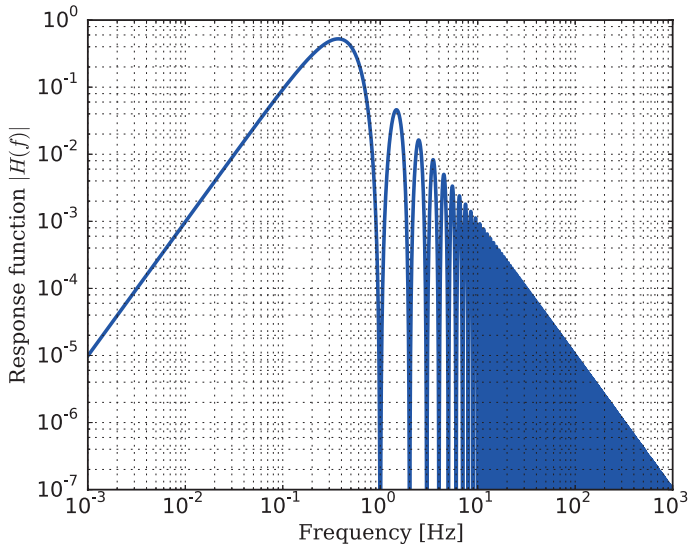

Figure B.1: Value of the response function $H(f)$ ($\tau = 1$ s).

Appendix C
Electrical Circuit in our Experiment

In Appendix C, we give details about the electrical circuits in our experiment.

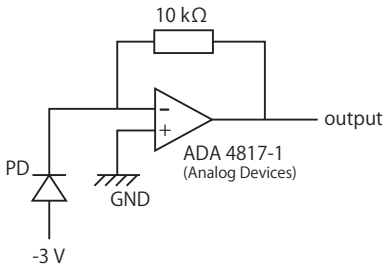

Figure C.1: Electric circuit for the InGaAs PD G12180-003A and G12180-250A (Hamamatsu Photonics's products).

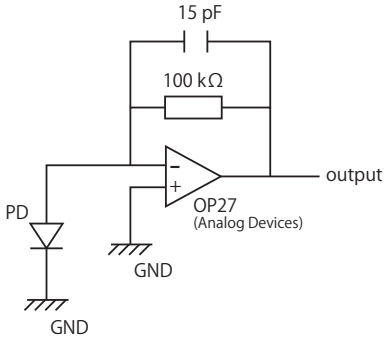

Figure C.2: Electric circuit for the InGaAs PD G12181-020K (Hamamatsu Photonics's product).

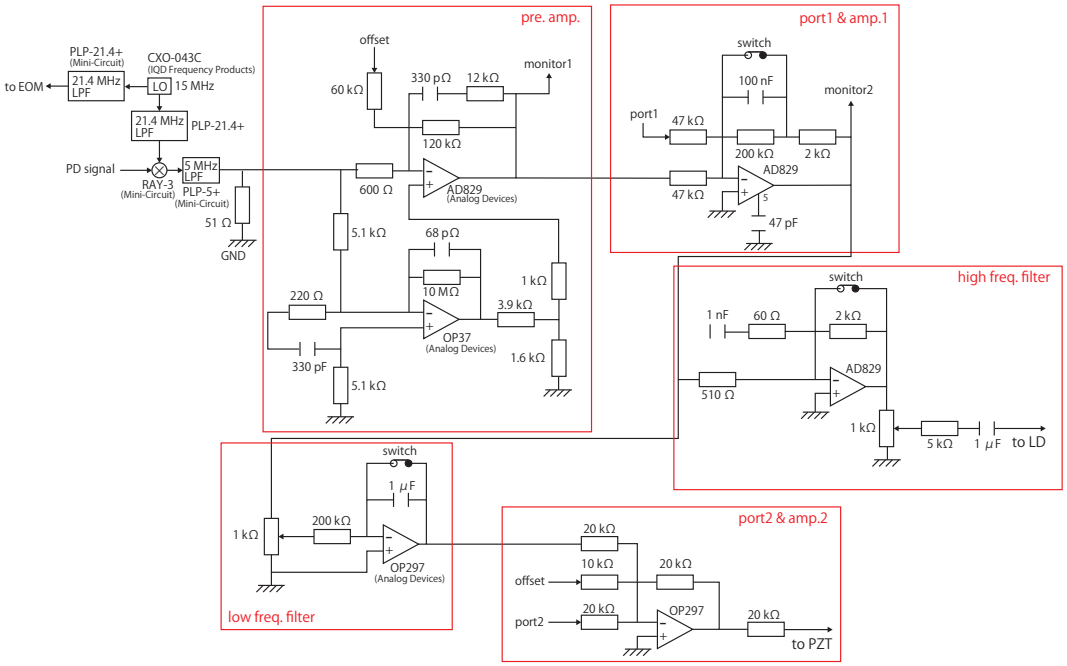

Figure C.3: Electric circuit for frequency stabilization. Several model numbers used in the circuit are given in this figure. Each block surrounded by red lines represents the components of the block diagram in Fig. 4.19

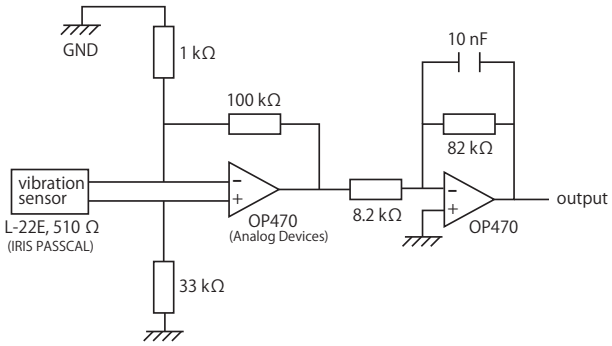

Figure C.4: Electric amplifier for the vibration sensor. Several model numbers used in the circuit are given in this figure. The gain of this circuit is about 1000.

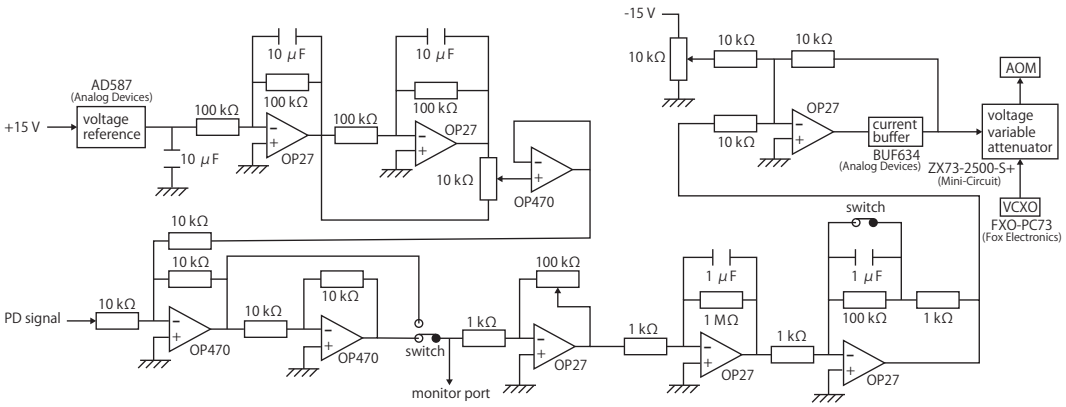

Figure C.5: Electric circuit for laser power stabilization. Several model numbers used in the circuit are shown in this figure.

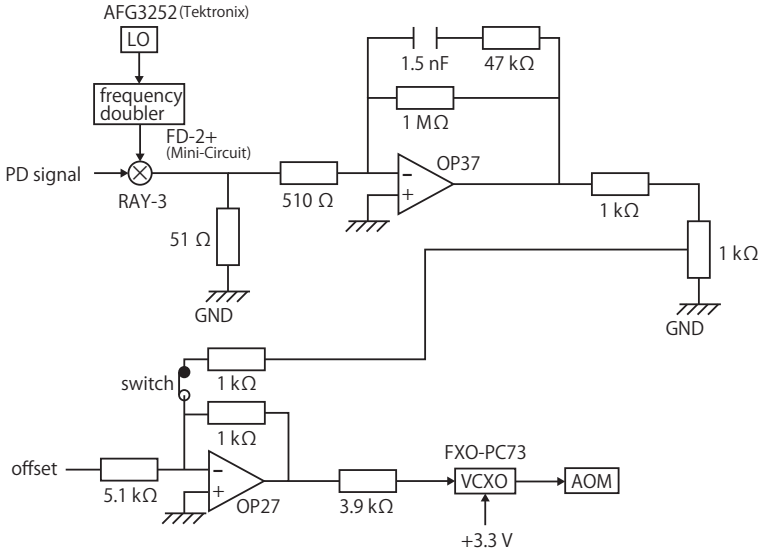

Figure C.6: Electric circuit for Doppler noise cancellation. The model numbers used in the circuit are given in this figure.

Appendix D
Photos of Experimental Setup

In Appendix D, we show several photos from our experimental setup.

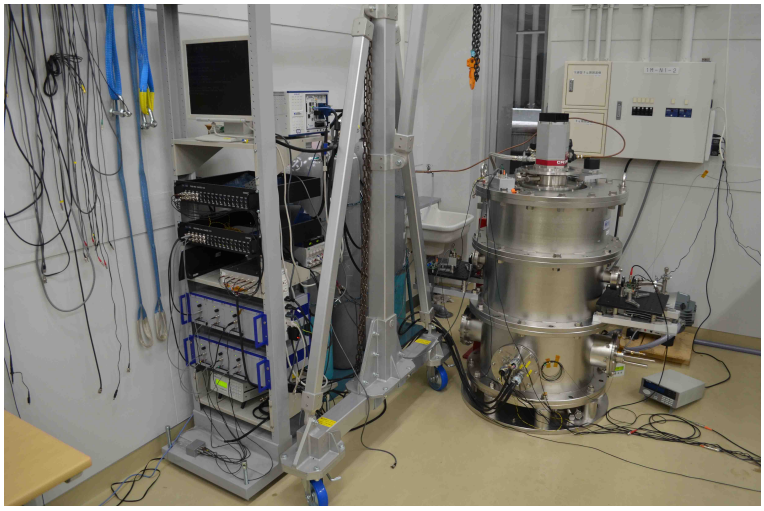

Figure D.1: Appearance of our setup. The cryostat is about 1.5 m in height and 0.8 m in width. The rack is a digital feedback system for the AVIS using a LabView real-time machine.

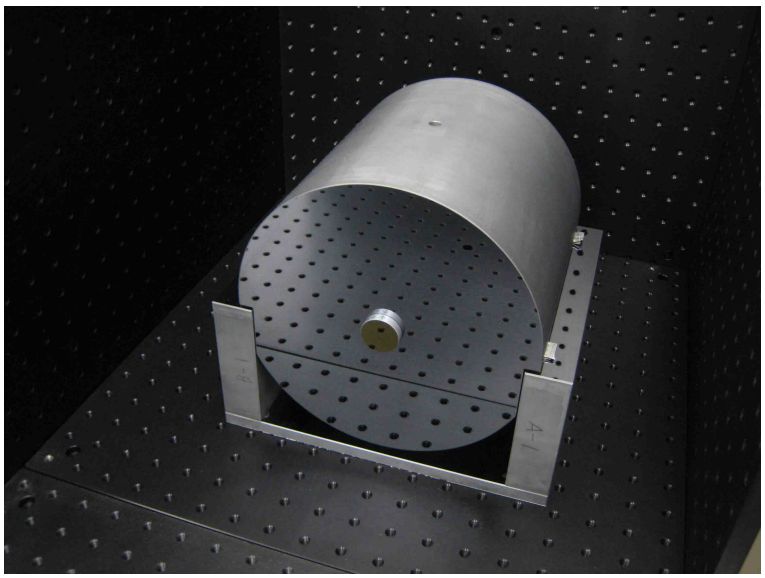

Figure D.2: Monocrystalline silicon optical cavity.

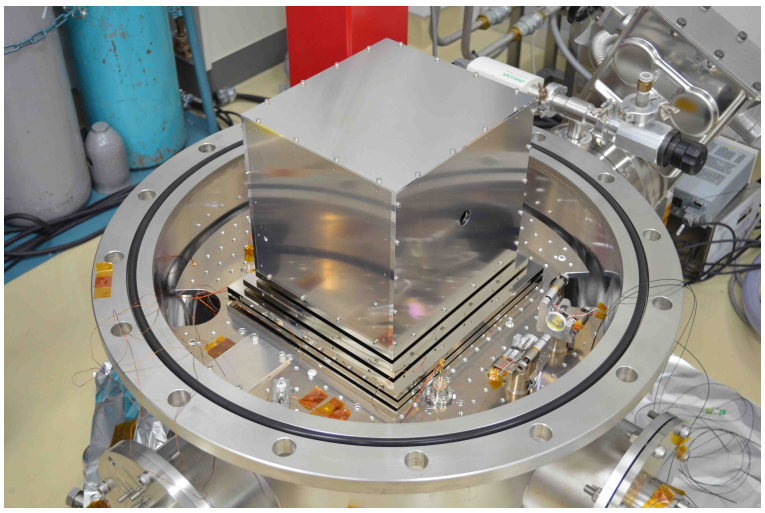

Figure D.3: Thermal-insulation stacks and an inner radiation shield. A silicon optical cavity is inside the inner shield.

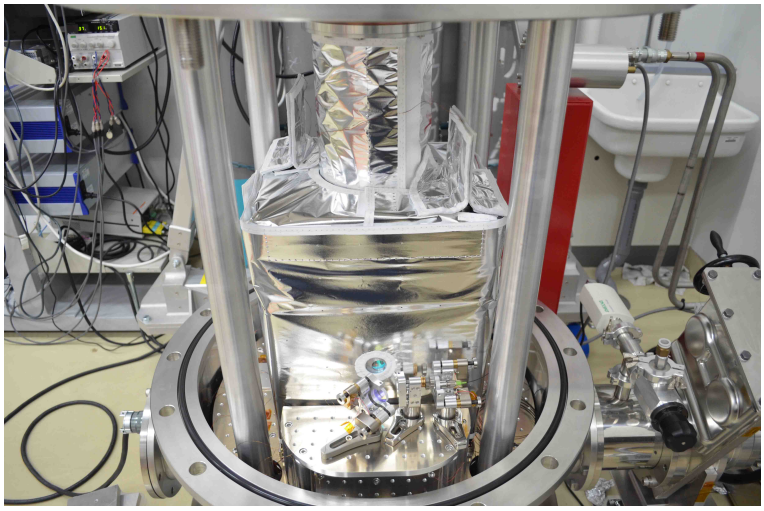

Figure D.4: Appearance inside the cryostat. The optics in front of an outer shield are ones for mode-matching. Behind an outer shield, there are some optics for monitoring the transmitted light through a FPC. The outer shield has two heaters for temperature control.

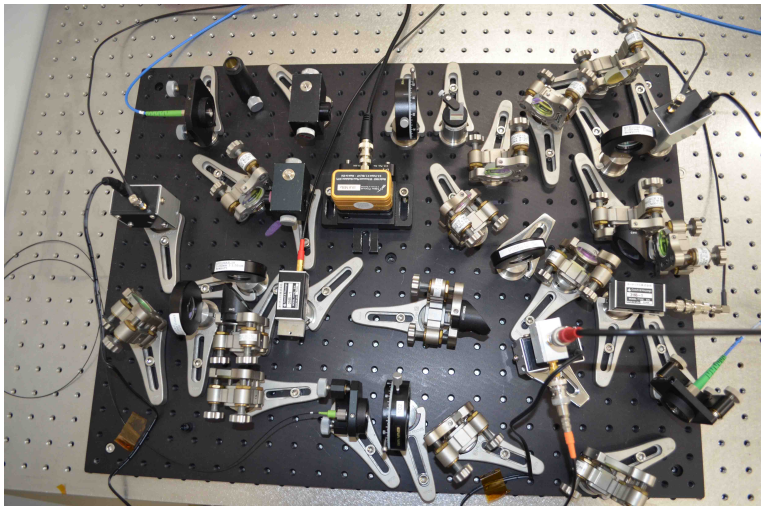

Figure D.5: Main part of an input laser system. This part is covered by a wind shield for reducing the Doppler noise.

Bibliography

1 Introduction

[1] T. H. Maiman, Nature **187**, 493-494 (1960).
Stimulated Optical Radiation in Ruby

[2] K. Kuroda, Class. Quantum Grav. **27**, 084004 (2010).
Status of LCGT

[3] G. M. Harry, Class. Quantum Grav. **27**, 084006 (2010).
Advanced LIGO: the next generation of gravitational wave detectors

[4] T. Accadia, *et al.*, J. Phys.: Conference Series. **203**, 012074 (2010).
Status and perspectives of the Virgo gravitational wave detector

[5] B. D. Tapley, *et al.*, Geophys. Res. Lett. **31**, L09607 (2004).
The gravity recovery and climate experiment: Mission overview and early results

[6] M. Takamoto, *et al.*, Nature **435**, 321-324 (2005).
An optical lattice clock

[7] M. Takamoto, *et al.*, Nat. Photon. **5**, 288-292 (2011).
Frequency comparison of optical lattice clocks beyond the Dick limit

[8] M. Yamanaka, *et al.*, Phys. Rev. Lett. **114**, 230801 (2015).
Frequency Ratio of ^{199}Hg and ^{87}Sr Optical Lattice Clocks beyond the SI Limit

[9] http://www.npl.co.uk/science-technology/time-frequency/optical-frequency-standards-and-metrology/units/secondary-representations-of-the-second

[10] S. Peil, *et al.*, Phys. Rev. A **87**, 010102 (2013)
Tests of local position invariance using continuously running atomic clocks

[11] Santarelli, G. *et al.*, IEEE Trans. Ultrason. Ferroelectr. Freq. Control **45**, 887-894 (1998).
Frequency stability degradation of an oscillator slaved to a periodically interrogated atomic resonator.

[12] T. Kessler, *et al.*, Nat. Photon. **6**, 687-692 (2012).
A sub-40-mHz-linewidth laser based on a silicon single-crystal optical cavity

[13] M. D. Swallows, *et al.*, IEEE Trans. Ultrason. Ferroelectr. Freq. Control **59**, 416-425 (2012)
Operating a 87Sr Optical Lattice Clock With High Precision and at High Density

[14] A. D. Ludlow, Doctoral Thesis, p170 (The university of Colorado, 2008)
The Strontium Optical Lattice Clock: Optical Spectroscopy with Sub-Hertz Accuracy
https://jila.colorado.edu/yelabs/sites/default/files/uploads/theses_2008_AndrewLudlow.pdf

[15] I. Ushijima. *et al.*, Nat. Photon. **9**, 185-189 (2015).
Cryogenic optical lattice clocks

[16] A.Yu. Nevsky, *et al.*, Optic. Comm. **210**, 91-100 (2002).
A Nd:YAG Laser with short-term frequency stability at the Hertz-level

[17] S. A. Webster, M. Oxborrow, and P. Gill, Optic. Lett. **29**, 1497-1499 (2004).
Subhertz-linewidth Nd:YAG laser

[18] A.Yu. Nevsky, *et al.*, Optic. Lett. **32**, 641-643 (2007).
Compact, thermal-noise-limited optical cavity for diode laser stabilization at 1×10^{-15}

[19] J. Alnis, *et al.*, Phys. Rev. A. **77**, 053809 (2008).
Subhertz linewidth diode lasers by stabilization to vibrationally and thermally compensated ultralow-expansion glass Fabry-Pérot cavities

[20] J. Millo, *et al.*, Phys. Rev. A. **79**, 053829 (2009).
Ultrastable lasers based on vibration insensitive cavities

[21] J. Millo, *et al.*, Nat. Photon. **5**, 158-161 (2011).
Making optical atomic clocks more stable with 10216-level laser stabilization

[22] G. D. Cole, *et al.*, Nat. Photon. **7**, 644-650 (2013).
Tenfold reduction of Brownian noise in high-reflectivity optical coatings

[23] E. Wiens, *et al.*, Optic. Lett. **39**, 3242-3245 (2014).
Silicon single-crystal cryogenic optical resonator

[24] F. Häfner, *et al.*, Optic. Lett. **40**, 2112-2115 (2015).
8×10^{-17} *fractional laser frequency instability with a long room-temperature cavity*

[25] Kenji Numata, Amy Kemery, and Jordan Camp, Phys. Rev. Lett. **93**, 250602 (2004)
Thermal-Noise Limit in the Frequency Stabilization of Lasers with Rigid Cavities

2 Frequency Stabilization

[26] T. Ushiba, Master Thesis, p5-p19 (The University of Tokyo, 2013).
「低温シリコン光共振器を用いた高安定化光源の開発」 (*Development of Highly Stabilized Laser using a Cryogenic Silicon Optical Cavity*; in Japanese)
http://granite.phys.s.u-tokyo.ac.jp/theses/ushiba_m.pdf

[27] M. Ando, Master Thesis, p25-p35 (The University of Tokyo, 1995).
「Fabry-Perot 型重力波検出器の制御」 (*Control of the Fabry-Perot type gravitational wave detector*; in Japanese)
http://t-munu.phys.s.u-tokyo.ac.jp/theses/ando_m.pdf

[28] A. L. Schawlow and C. H. Townes, Phys. Rev. **112**, 1940-1949 (1958).
Infrared and Optical Masers

[29] D. Shoemaker, *et al.*, Optic. Lett. **14**, 609-611 (1989).
Frequency-stabilized laser-diode-pumped Nd:YAG laser

[30] R. W. P. Drever, *et al.*, Appl. Phys. B **31**, 97-105 (1983).
Laser phase and frequency stabilization using an optical resonator

[31] E. D. Black, Gen. Am. J. Phys. **69**, 79-87 (2001).
An introduction to Pound-Drever-Hall laser frequency stabilization

[32] K. Yamamoto, Doctoral Thesis, p25-p36 (The University of Tokyo, 2000).
Study of the thermal noise caused by inhomogeneously distributed loss
http://t-munu.phys.s.u-tokyo.ac.jp/theses/yamamoto_d.pdf

[33] K. Kokeyama, *et al.*, J. Opt. Soc. Am. A **31**, 81-88 (2014).
Residual Amplitude Modulation in Interferometric Gravitational Wave Detectors

[34] S. Moriwaki, 『重力波をとらえる』 edited by T. Nakamura, N. Mio, M. Ohashi, p.224-228 (Kyoto University Press, 1998).

3 Experimental Design

[35] L. S. Ma, *et al.*, Optic. Lett. **19**, 1777-1779 (1994).
Delivering the same optical frequency at two places: accurate cancellation of phase noise introduced by an optical fiber or other time-varying path

[36] D. F. McGuigan, *et al.*, J. Low Temp. Phys. **30**, 621-629 (1978).
Measurements of the Mechanical Q of Single-Crystal Silicon at Low Temperatures

[37] K. G. Lyon, *et al.* J. Appl. Phys. **48**, 865-868 (1977).
Linear thermal expansion measurements on silicon from 6 to 340 K

[38] Hartnett, J.G., *et al.*, Ultrasonics, Ferroelectrics, and Frequency Control **57**, 1034-1038 (2010).

Cryogenic sapphire oscillator using a low-vibration design pulse-tube cryocooler: first results

[39] J. J. Wortman and R. A. Evans, J. Appl. Phys. **36**, 153-156 (1965).
Young's Modulus, Shear Modulus, and Poisson's Ratio in Silicon and Germanium

[40] P. R. Saulson *Fundamentals of Interferometric Gravitational Wave Detectors*, p.127 (World Scientific, Singapore, 1994).

[41] G. K. WHITE and P. J. MEESON,
"Experimental Thchniques in Low-Temperature Physics" (OXFORD SCIENCE PUBLICATIONS)

[42] T. Akatsuka, *et al.*, Jpn. J. Appl. Phys. **53**, 032801 (2014).
30-km-long optical fiber link at 1397 nm for frequency comparison between distant strontium optical lattice clocks

4 Performance Evaluation

[43] http://www.sercel.com/products/Lists/ProductSpecification/Geophones_specifications_Sercel_EN.pdf

5 Stability Estimation

[44] W. Zhang, *et al.*, Optic. Lett. **39**, 1980-1983 (2014).
Reduction of residual amplitude modulation to 1×10^{-6} *for frequency modulation and laser stabilization*

[45] A. Shoda, Doctoral Thesis, p50-p54 (The University of Tokyo, 2014).
Development of a High-Angular-Resolution Antenna for Low-Frequency Gravitational-Wave Observation
http://granite.phys.s.u-tokyo.ac.jp/shoda/Thesis_shoda.pdf

6 Conclusion

[46] T. Sekiguchi, JGW **1**, 1402971 (2014).
Seismic Spectrum in Kamioka Mine
http://gwdoc.icrr.u-tokyo.ac.jp/DocDB/0029/T1402971/001/141106_seismic_noise.pdf

B Allan Deviation

[47] T. J. Witt, IEEE Instrum. Meas. **50**, 445-448 (2001).
Using the Allan Variance and Power Spectral Density to Characterize DC Nanovoltmeters